Nanofluidic transport using charge-selective interfaces

by

Sourayon Chanda

A thesis submitted in partial fulfillment of the requirements for the degree of

Doctor of Philosophy

Department of Mechanical Engineering
University of Alberta

Abstract

Nanotechnology has advanced research and development in various engineering disciplines, for instance, charged nano-confinements with overlapping electrical double layers act as charge-selective pores, thereby benefiting a wide range of technologies such as desalination, membrane technology, and renewable energy. In this regard, a sound knowledge of nanofluidic transport is essential. This doctoral dissertation contributes to this research area by providing a better understanding of flow through charged nano-confinements.

As an essential forcing mechanism, a gradient of electrolyte concentration along a charged nano-confinement can cause fluid motion without the need of an external electrical field or pressure difference. This phenomenon, known as diffusioosmosis, is frequently encountered in micro/nano-fluidic devices and biological systems. In this doctoral research, we numerically investigate diffusioosmotic nanoflow in a charged nanochannel connecting two reservoirs of different salt concentrations–a typical fluidic configuration for a variety of innovative applications. Under a wide range of parameters, our simulation results show that the flow speed inside the nanochannel is linearly dependent on the concentration difference between the two reservoir solutions, Δc. On the other hand, the flow direction was influenced predominantly by three key parameters: nanochannel length, height, and surface charge density. Based on a comparative study between chemiosmotic and electroosmotic flow, we identified a non-dimensional number to delineate different diffusioosmotic flow directions, thereby providing a feasible strategy for flow control in a charged nanochannel. We also investigated diffusioosmotic flow in a tapered nanochannel, where we found a significant dependence of the nanoflow through the channel on the nanochannel taper angle and tip diameter.

An interesting application of diffusioosmotic flows can be observed in the case of renewable energy generation through reverse electrodialysis (RED). We numerically investigate such a process of renewable power generation using a two-dimensional single cell model of RED. Our numerical model consists of constant inflow of salt solutions of different concentrations through two reservoirs, which are connected by a charged nanochannel. We compute the coupled flow, ion flux, electrical potential, and resultant electric outputs in the nanofluidic RED cell. The results of nanochannel resistance and power output density reveal a power-law relationship on the concentration difference, quantitatively shedding light on the optimal RED flow designs. Our simulations at different inflow velocities show that the electrical output parameters remain nearly constant at low speed but increases at high velocity when the advection effect becomes significant. To examine renewable power generation by harvesting salinity gradient energy through RED, we designed a fluidic cell, consisting of two reservoirs separated by a nanoporous cation-selective (Nafion) membrane. Two electrolyte solutions of different salt concentrations flow through the reservoirs, creating a salt-concentration difference across the membrane. Using our single cell experimental setup, we investigate the effects of salt-concentration variation, Δc (between the two reservoirs), and flow velocity on the renewable electricity generation. The current-voltage (I-V) characteristics of the single RED unit shows a linear relationship. Similar to the predictions from our numerical simulations, the variation of internal resistance reveals a power-law dependence on Δc, while the open-circuit voltage shows a logarithmic relationship. For the range of flow rate explored, change of inflow velocity has an insignificant impact on the I-V data of the RED cell.

Preface

This thesis is an original work by Sourayon Chanda, under the supervision of Dr. Peichun Amy Tsai.

Chapter 3 of this thesis has been submitted to *Soft Matter* as Sourayon Chanda & Peichun Amy Tsai, "Diffusioosmotic flow in charged nanofluidics", and is currently under revision.

Chapter 4 of this thesis is being prepared for submission to *Langmuir* as Sourayon Chanda & Peichun Amy Tsai, "Diffusioosmosis in tapered nanochannels". This numerical work was benchmarked with other numerical investigations with guidance from Dr. Tsai.

Chapter 5 of this thesis has been published as Sourayon Chanda & Peichun Amy Tsai, "Numerical simulation of renewable power generation using reverse electrodialysis", Energy (2019), vol. 176, 531 – 543. I was responsible for numerical modeling in COMSOL, and initial drafts of the manuscript. Dr. Tsai provided rigorous feedback during the numerical modeling and manuscript writing, critically verifying the numerics.

The manuscript corresponding for Chapter 6 is under preparation, to be submitted as Sourayon Chanda & Peichun Amy Tsai, "Renewable power generation by reverse electrodialysis using a charge-selective membrane".

This doctoral thesis is dedicated to

my grandparents (the doctors, who used to save lives):

Dadu, *Dr. Prafulla Kumar Majumder*

and

Didibhai, *Dr. Maya Majumder.*

Acknowledgements

I would like to take this opportunity to heartily thank my supervisor, Dr. Peichun Amy Tsai for her support and motivation towards the present research. Her efficient guidance and assistance towards this doctoral program enabled progress in research to occur at a steady rate. Working under her supervision, I got valuable opportunities to present and attend several international conferences and workshops and visit research groups.

I am grateful to all my colleagues of our research group at the University of Alberta for their valuable comments and suggestions. The fortnightly group meetings where we get to present in turn provided insight into my research through a different set of eyes, and helped me improve considerably.

I am greatly indebted to Alberta Innovates Technology Futures for supporting me through their graduate student scholarship. This research is also supported by Natural Sciences and Engineering Research Council of Canada (NSERC) for the Discovery and Accelerator grants as well as Canada Research Chair Program in Fluids and Interfaces.

I would like to anonymously thank all the fellow researchers and friends who have helped my directly or indirectly to continue my studies at the University of Alberta.

Last but not the least, I would like to thank my entire family for their continued support and motivation throughout this PhD thesis research.

Contents

List of Figures

List of Tables

Nomenclature

Acronyms

EDL	electric double layer
ICR	ion current rectification
RED	reverse electrodialysis
SGE	salinity gradient energy

Constants

ϵ_0	permittivity of free space	8.85×10^{-12} F m^{-1}
e	elementary charge	1.602×10^{-19} C
F	Faraday's constant	96,485 C mol^{-1}
k_B	Boltzmann constant	1.38×10^{-23} J K^{-1}
R	universal gas constant	8.314 J K^{-1} mol^{-1}

Symbols

α	cone angle of tapered nanochannel
δ	anion concentration ratio
ϵ_r	relative permittivity of water ($\simeq 80$)
η	energy conversion efficiency

η_m	energy conversion efficiency at maximum power output
λ_D	Debye length
λ_B	Bjerrum length
λ_{GC}	Gouy-Chapman length
μ	coefficient of viscosity
ϕ	electric potential
ϕ_0	open-circuit voltage
ϕ_c	potential supplied by the RED cell
σ	surface charge density
$\vec{E}$	electric field
$\vec{u}$	velocity vector
ζ	zeta potential
A_c	effective nanochannel cross-sectional area for the numerical analysis; effective membrane cross-sectional area in the experimental investigation
C	non-dimensional number to predict the nanoflow direction
C^*	critical non-dimensional number to predict the nanoflow direction
c_+	cation molar concentration
c_-	anion molar concentration
c_H	concentration of concentrated solution
c_L	concentration of dilute solution
c_R	concentration ratio of concentrated to dilute solution

$c_{-,out}$ average anion concentration at c_H reservoir exit

D_+ diffusion coefficient of cation

D_- diffusion coefficient of anion

F_e electrical body force

h nanochannel height

I_c circuit current

I_{SC} short-circuit current

J_s total number of ions transported through the nanochannel per unit time

l nanochannel length

p pressure

P_c' power output

$P_{c,m}'$ maximum power output

$P_{c,m}$ maximum power output density

Pe Peclet number

q net charge

R_c nanochannel resistance

R_e external resistance

Re Reynolds number

T temperature (in Kelvin)

u_{CO} chemiosmotic velocity

u_{DO} diffusioosmotic velocity

u_{EO} electroosmotic velocity

v_f inflow velocity

z_+ valence of cation

z_- valence of anion

$\vec{J}_+$ anionic (molar) flux

$\vec{J}_-$ cationic (molar) flux

Subscripts

$+, -$ cation, and anion

Chapter 1

Introduction

The study of fluid mechanics at the laboratory-scale can be broadly classified into three categories: millifluidics, microfluidics, and nanofluidics [8]. While millifluidic and microfluidic setups have at least one of the dimensions of the flow apparatus in the scale of millimeters and micrometers, respectively, nanofluidics deals with devices where at least one dimensions are in the nanometer scale. Due to the different length scales, the surface area to volume ratio in these three classifications are significantly different. Dominant surface forces are witnessed for micro/nanofluidic setups, which are insignificant in larger scale flows, causing flows through micro/nano geometries to be distinctively different from conventional large-scale streams. The present doctoral research investigates fluidic systems in the nanoscale regime using numerical and experimental techniques.

1.1 Fundamentals of nanofluidics

Nanofluidics is a branch of fluid mechanics that investigates fluidic interactions and influences at the nanoscale regime. In general, nanofluidic transport deals with length scales ranging from 1 nm to 100 nm [8]. Since such minute geometries and fluid interactions are not visible to the naked human eye, sophisticated magnification technologies such as scanning electron microscopy and atomic force microscopy are used to visualize such systems. Fuelled by the rapidly growing interest in nanofluidics, path-breaking nanofabrication techniques have been

reported, such as electron beam lithography, optical projection lithography, X-ray lithography [9]. In addition to these conventional techniques, researchers have also fabricated nanostructures through self-assembly [10], nanoimprint lithography [11], and scanning probe lithography [12]. The boom in nanoscale research over the past few decades can be attributed to the close resemblance of nanofluidic setups to naturally-occurring biological systems, such as charge-selective membranes, cell pores, which can bring us closer to building structures in close resemblance to that found in nature.

Due to the higher surface-area-to-volume ratio in micro/nano-fluidic systems, several surface-related phenomena are found to be dominant over other volume effects. Some of the significant surface effects at the micro/nanoscale are described below:

Surface tension

The tendency of fluid surfaces to minimize their surface area to the lowest possible value is originated from surface tension. This minimization of the surface area is the result of the inherent tendency of molecules to remain in the state of lowest energy. Surface tension is proportional to the strength of the adhesive force in a solid-liquid interface and is measured in force per unit length. This surface property plays a crucial role in a number of daily-use products, for example, paints, pharmaceuticals, detergents. Fluid motion can also be initiated in specially designed apparatus utilizing differences in surface tension, which is widely known as Marangoni effect [13]. By exploiting surface tension between solid-water interfaces, superhydrophobic surfaces are synthesized for a variety of applications, for instance, drag reduction [14, 15], self-cleaning coatings [16], and anti-icing systems [17]. Due to the higher surface-area-to-volume ratio, surface tension can also play a very crucial role in nanofluidic transport.

Capillary action

Capillary action is the ability of a liquid to flow in narrow spaces without the assistance of external forces [18]. Capillary action has many benefits to current technological equipment, such as in manometers and barometers [19] and liquid chromatography [20]. Biological appli-

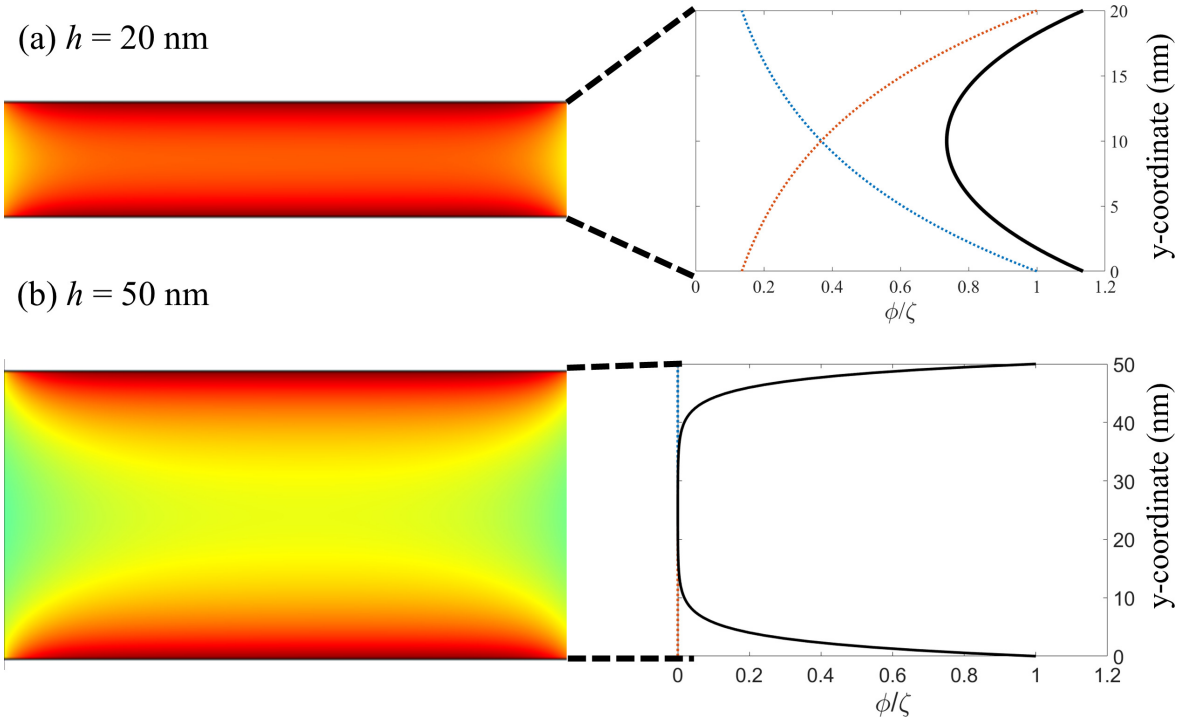

Figure 1.1: Electric potential distribution in nanochannels of different height: (a) h = 20 nm, demonstrating the overlapping of EDL and (b) h = 50 nm, showing no EDL overlap. The electric potential, ϕ has been normalized with zeta potential, ζ. The red and blue dotted line represent the 1-D electric potential profile from the top and bottom surfaces, respectively, whereas the solid black line is the resultant electric potential in the nanochannel.

cations of capillary rise can be witnessed in plants, where capillary action is utilized in the supply of fluids to leaves and branches from the roots [21]. The capillary force has been extensively utilized in nanofluidic equipment and for different nanofabrication techniques, such as to fabricate various polymeric structures using capillary force lithography [22].

Electric double layer (EDL)

Due to the presence of free electrons or holes near the surface, many substrates develop a fixed surface charge when they are in contact with certain electrolytes [23]. This makes such surfaces either positively or negatively charged when placed in contact with such solutions. The electrostatic attraction by the surface charge causes the counter-ions near the surface to form a layer of fixed charges (or the so-called Stern layer). Above the Stern layer forms the diffuse layer, which consists of loosely-held counter-ions. The ions in the diffuse layer can be

easily displaced under the effect of some stronger driving force [24], such as external pressure gradient, or electric field. These two layers are essentially termed as EDL, which plays a very significant role in the dynamics of fluid motion through these thin confinements. The Debye length, λ_D represents the thickness of the EDL, and for a monovalent symmetric electrolyte (i.e., ionic valence, $z_+ = z_- = 1$), it can be mathematically expressed as:

$$\lambda_D = \sqrt{\frac{\epsilon_0 \epsilon_r RT}{2F^2 c_0}} \tag{1.1}$$

where c_0 is the ion concentration, ϵ_r is the relative permittivity of the medium, ϵ_0 ($= 8.854 \times 10^{-12}$ Fm $^{-1}$) is the permittivity of vacuum, and F ($= 96{,}485$ Cmol^{-1}) is known as Faraday's number. Overlapping of EDL is observed in narrow nano-confinements, which causes significant variation in overall flow, and gives rise to charge-selective behavior in certain nanoporous membranes [25]. For a quick introspection, $\lambda_D \approx$10 nm when $c_0 \approx 1$ mM, and thus, in this case, nanochannels of height $\lesssim 20$ nm will experience an EDL overlap whereas wider channels ($\gtrsim 25$ nm) would not.

1.2 Electrokinetic flow in nano/micro-fluidics

The study of fluid flow of electrolytes fluids through charged nano-sized compartments is broadly referred to as electrokinetics [26]. Some types of electrokinetic flows are described below:

1.2.1 Pressure-driven transport

Pressure-driven transport, predominantly used in large-scale fluidic setups, can also be useful in micro/nano-fluidic systems. However, the pressure difference that needs to be applied to nano-confinements is higher, and thus, the compressibility of fluids needs to be considered when the channel dimension is ≤ 10 nm [27]. There are a plethora of engineering applications of nanofluidic flow driven by a pressure gradient. For example, pressure-driven nanofluidic transport was implemented to generate renewable energy [28, 29], to study the transport behavior of DNA molecules [30], and to generate high-velocity flow through carbon nanotubes

[31]. In a comparative study regarding solute separation, Xuan et al. reported that solutes with different valence are more effectively separated via pressure-driven flow, whereas electroosmotic flow is more efficient in separating charged ions with different mobility [32].

1.2.2 Electroosmosis

Fluid flow is a micro/nano-fluidic setup due to the effect of an electric field is termed as electroosmosis. Electroosmotic transport is caused by electromigration of ions due to an external electric field or induced one (caused due to interaction between surface charge and ions in the electrolyte). Under the effect of an electrical body force, F_e, the electroosmotic velocity, u_{EO}, for a charged nano-confinement of constant zeta potential, ζ, along its surface, can be described using the Stokes equation as shown below [33]:

$$\mu \frac{\partial^2 u}{\partial x^2} - \frac{\partial p}{\partial x} - F_e = 0. \tag{1.2}$$

where $F_e = qE_x$: q is the charge density and E_x is the tangential electric field in x-direction. Considering 1-D distribution of charge, the charge density q is related to the electric potential, ϕ, and can be described by the 1-D Poisson's equation, which is given by:

$$\epsilon_0 \epsilon_r \frac{\partial^2 \phi}{\partial x^2} = -q, \tag{1.3}$$

In addition, for a simplified 1D analysis, the concentration distribution can be expressed using the Boltzmann distribution of ions:

$$c\pm = c_0 \exp\left(\mp \frac{ez\phi}{k_B T}\right) \tag{1.4}$$

where k_B is the Boltzmann constant and T is the operating temperature. Using these three equations, we can obtain a simplified 1D formulation of electroosmotic velocity, u_{EO} [24, 34]:

$$u_{EO} = -\frac{\epsilon \zeta E_x}{\mu} \tag{1.5}$$

Electroosmosis plays a prominent role in plant physiology, and the resultant transportation of fluids [35]. To name a few industrial applications, electroosmotic flow finds its usage in sludge dewatering [36] and micropumps [37].

1.2.3 Electrophoresis

The motion of suspended particles in an electrolyte solution under the influence of an external electric field is known as electrophoresis [38]. A simple electrophoretic system includes an electrolyte solution with two electrodes of opposite charge which supplies the external electric field ($\vec{E}$). In such a system, the electrophoretic velocity of a colloidal particle ($\vec{v_{ep}}$) is proportional to the applied electric field, and can be expressed as $\vec{v_{ep}} = m\vec{E}$, where m is known as the electrophoretic mobility of the particle. Electrophoresis has several biological applications, including the manipulation and segregation of DNA molecules [39], protein separation [40]. Due to its ability to mobilize charged particles, it has been widely used for the segregation of biomolecules, such as DNA [41], cells [42], proteins [43]. Electrophoresis has also been frequently used for abiotic applications in the chemical separation of charged particles [44].

1.2.4 Diffusioosmosis

Another kind of electrokinetic flow is caused by the transport of electrolytes along a charged surface due to a concentration gradient across the nano-confinement. This type of fluid flow, termed as diffusioosmotic flow (DOF) [45, 46], has not been addressed in detail in the literature for unconventional geometries. This doctoral thesis, thus, investigates diffusioosmosis in various geometries for different flow configurations. A typical schematic of DOF through a positively-charged nanochannel with constant flow of solutions of different concentration is shown in Fig. 1.2.

Diffusioosmosis primarily consists of two components, which drives the fluid flow. One part due to the driving force of concentration difference is known as chemiosmosis, whereas the other component is electroosmosis, which arises due to the induced electric field inside the nanochannels. Since electroosmosis has been discussed before, we will focus on the mathematical description of chemioosmosis in this section.

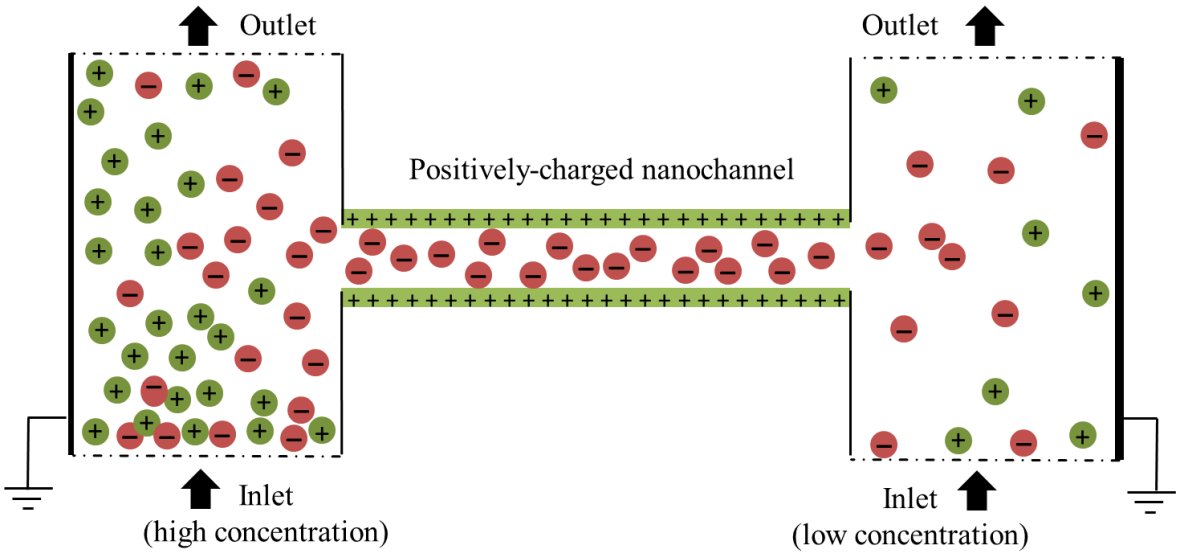

Figure 1.2: Schematic diagram of a two-dimensional model of diffusioosmotic flow through a positively-charged nanochannel.

Chemiosmosis

When a flow adjacent to a charged surface is subjected to a concentration difference, Δc, across its length, a chemical potential gradient develops in the compartment. This initiates fluid flow from one side of the compartment to another and is referred to as chemiosmotic velocity, u_{CO}. In a simple system assuming no velocity fluctuations in the transverse direction (i.e., velocity in the y-direction, $u_y = 0$), this flow configuration can be described using the Stokes equation [33, 47]:

$$\mu \frac{\partial^2 u}{\partial x^2} - \frac{\partial p}{\partial x} - (c_+ - c_-) ze \frac{\partial \phi}{\partial x} = 0. \tag{1.6}$$

$$\frac{-\partial p}{\partial y} - (c_+ - c_-) ze \frac{\partial \phi}{\partial y} = 0 \tag{1.7}$$

where u_x is the velocity in x-direction, p is the pressure, c_+ and c_- are the cation and anion concentration, respectively, ϕ is the electric potential, z is the valence, e is the unit electronic charge, and μ is the viscosity coefficient. After appropriate mathematical simplifications of the above equations, the chemiosmotic velocity can be expressed as [48, 49]:

$$u_{CO} = -\frac{k_B T}{\mu} \frac{\ln(1-\gamma^2)}{2\pi\lambda_B} \frac{\Delta c}{l c_0}. \tag{1.8}$$

where $\gamma = \tanh \frac{ze\zeta}{4k_BT}$: ζ is the zeta potental of the surface, k_B is the Boltzmann constant, and T is the operating temperature.

1.2.5 Diffusiophoresis

The migration of particles in an ionic solution under an external concentration difference is termed as diffusiophoresis. Diffusiophoresis can be useful in many day-to-day activities such as cleaning of stains in clothes [50], effective deposition of aerosols in lungs [51], and efficient interaction of digestive enzymes with bacterial cells [52]. By causing faster deposition of particles in membranes, diffusiophoresis can be harmful in specific micro/nano-fluidic systems by contributing to membrane fouling [53]. In addition, chemical reactions, crystallization, and sedimentation in abiotic and biotic systems can cause local concentration variation initiating diffusiophoretic flow, which can either be beneficial or detrimental to the system operation [54].

1.2.6 Thermo-osmosis

Transport of fluid due to a temperature difference in a fluidic system is termed as thermo-osmosis [55]. This phenomenon is receiving a lot of attention lately, due to its ability to utilize waste heat from industries to mobilize fluidic systems [56]. Researchers have even utilized a thermal gradient in a nanofluidic setup to harness heat energy [57].

1.2.7 Thermophoresis

Similar to diffusiophoresis, thermophoresis is the transport of particles in a fluid medium when a temperature gradient is applied across it. In certain fluidic systems with no scope of external electric field or concentration difference, thermophoresis offers a convenient way to mobilize charged or uncharged particles. As a result, thermophoresis is frequently used for many bio-engineering applications. For instance, investigation of droplet motion by thermophoresis in a carbon nanotube was reported [58, 59], protein interactions in abiotic systems under microscale thermophoresis was studied [60]. Researchers further reported the mobilization of

single-stranded DNA through thermophoresis by infrared heating of the solution containing DNA strands [61].

1.3 Ion-exchange membranes

Ion-exchange membranes (IEMs) are a particular type of membranes that allow ions of only one kind of charge to pass through, while blocking the other type of charge [62, 63]. This specific property arises since these membranes acquire surface charge during their interaction with electrolytes and as a result, attract counter-charges while repelling away co-charges. This spectacular property of these membranes allows them to be used for many engineering applications. Depending on this ion-selective property, IEMs can be of two kinds:

1. **Cation exchange membrane (CEM):** This kind of membranes allows cations to pass through, whereas blocking the passage of anions. Some commercially available CEMs are the Nafion membrane, alumina membrane (Sigma-Aldrich).

2. **Anion exchange membrane (AEM)** These membranes typically promote the passage of anions through them, and prevents the flow of cations. A few examples of commercially available AEMs are fluorinated membranes [64], Xion (The Fuel Cell Store).

Ion transport adjacent to IEMs includes a number of processes i.e., diffusion, electromigration, and convection. These processes cause non-uniform concentration distribution along with the pores and can be mathematically expressed using the Nernst-Planck equation [65]:

$$-\vec{\nabla}\cdot\left(D_{\pm}\vec{\nabla}c_{\pm}+\frac{D_{\pm}}{RT}z_{\pm}Fc_{\pm}\vec{\nabla}\phi\right)+\vec{u}\cdot\vec{\nabla}c_{\pm}=0, \tag{1.9}$$

Here, c_+ and c_- are the cation and anion concentration, respectively, whereas z_+ and z_- are the corresponding valence of the ions. $\vec{u}$ is the flow velocity vector. T (= 293 K) is the operating temperature, R (= 8.314 $JK^{-1}mol^{-1}$) is the universal gas constant, F (= 96,485 $Cmol^{-1}$) is the Faraday's number, and D_+ and D_- are the diffusivities of the cation and anion, respectively. The terms in the above equation describe the contribution via diffusion, electromigration, and convection of ions, respectively [24]. Due to its unique property of charge selection, these

membranes play a crucial role in several industrial processes, such as water desalination, power generation, and waste treatment.

1.4 Applications of Nanofluidics

With improved lithographic and etching techniques, nanofluidics is presently implemented for the improvement of many processes that deal with fluidic systems. For example, nanofluidic transport finds its application in various areas of engineering and biomedicine, such as water purification [66], renewable energy generation [67], biomolecule separation [41], flow detection [27]. In this section, we will discuss two applications of nanofluidic transport.

1.4.1 Water purification

Providing clean and safe drinking water to the rapidly increasing population has been a significant concern for under-developed and developing nations. Traditional water purification involves several steps, such as sedimentation, disinfection, and filtration, which is both time-consuming and cost-intensive. In this regard, various membranes with miniature pore dimensions have demonstrated great potential for desalinating water, which could play an essential role in reducing the total time and overall cost of water purification [68, 69]. With recent advances in membrane technology, composite membrane, synthesized from readily available bio-based renewable polymers, have demonstrated high water rejection properties [70]. Besides, these membranes manufactured from natural sources have a low environmental impact and purifies water faster than conventional techniques. Some examples of nanoporous membranes used to water purification purposes are polysulfone membrane, polyethersulfone membrane, polyamide membranes [66].

1.4.2 Renewable energy

Conventional energy sources, such as coal, gas, petroleum has powered the world for a very long time. However, there are major drawbacks to using these energy sources, for instance, its non-renewability, environmental pollution, and the greenhouse effect. According to estima-

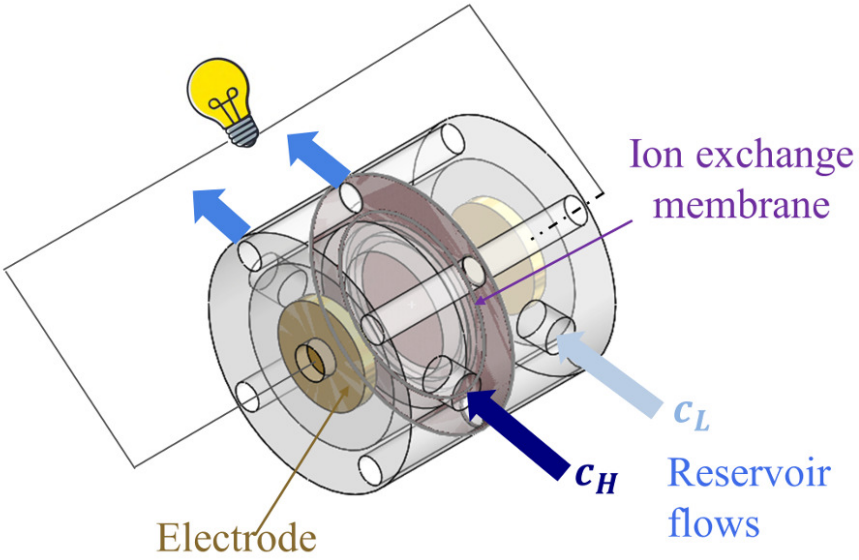

Figure 1.3: Schematic of a reverse electrodialysis cell, using a single ion-exchange membrane.

tions in 2005, with no new oil reserve discovery, the present oil reserves will run out in 32 years [71], which does cause serious questions to the sustainability of life on the planet, unless we successfully find alternative energy sources. In this regard, extensive research is going on to find alternative renewable sources of energy, such as solar energy [72, 73], wind energy [74, 75], fuel cells [76, 77], hydropower [78, 79]. Another such a source of renewable energy is salinity gradient energy (SGE), which refers to the available energy due to thermodynamic mixing of two solutions of different concentrations, and can be harnessed using charged nanoporous membranes, such as reverse electrodialysis (RED), and pressure-retarded osmosis [80].

Reverse electrodialysis

Reverse electrodialysis (RED) is an emerging technology for harvesting SGE and has been investigated in detail in the present thesis, both numerically and experimentally. A typical RED cell stack, illustrated by Fig. 1.3, consists of ion exchange membranes assembled to form alternating compartments of high salinity and low salinity solutions, with electrodes at the end to harness the Gibbs free energy of mixing [67].

The concept of RED was first introduced by Pattle [81] by flowing salty and freshwater

separated by alternate acidic and basic membranes. Through this setup, he demonstrated the possibility of energy generation using charge-selective nano-confinements by obtaining a maximum power output of 15 mW. To understand the inherent mechanism of ion transport and electrical interactions in RED, Osterle and colleagues analytically studied the behavior of charged membranes for small [82], and large concentration differences [83] between the two solutions. In their theoretical analyses with Debye-Hückel linearization, they found that the dimensionless membrane potential increases with an increase in concentration ratio and a decrease in pore size. They further reported a high efficiency of energy conversion for very narrow confinements (i.e., when $\mathcal{O}(h) \sim \mathcal{O}(\lambda_D)$, where h and λ_D are the nanochannel height and Debye length respectively). Recently, the analytical estimation of the maximum power density of RED stacks was reported by Vermaas et al. [84]. They concluded that with the present technological advances, a maximum power density of 2.7 W/m^2 could be achieved. Moreover, significantly higher power densities (~20 W/m^2) could be reached by decreasing the membrane resistance and cell length. Vermaas and co-workers further designed a RED cell with recirculation of the feed water, theoretically achieving an efficiency of more than 50% through co-, counter- and cross-flow methods [85].

Through small-scale laboratory experiments, several studies have shown the feasibility of generating power using RED. Similar to Pattle [81], Turek et al. designed a RED experimental setup using alternating cation and anion exchange membranes, and observed power generation for different solution concentrations and flow velocities [86]. They concluded that a low concentration of dilute solution (~ 0.56 g/L) and an optimum flow velocity (~ 0.54 cm/s) can generate maximum electrical output (~ 460 mW/m^2). Suda et al. designed a 59-compartment RED setup with ion-exchange membranes to investigate SGE generation [87]. They reported an exponential decay of power output with time, which may be explained with a capacitor-type equivalent electrical circuit. Post et al. [88] focused on the energy recovery of RED cells and reported that internal energy loss could be reduced by lowering inter-membrane distance. Galama et al. experimentally studied the effect of salinity gradient on the cation exchange membrane and its resistance, reporting that the membrane conductance is mainly determined by the lowest external concentrations [89]. In the quest to improve the efficiency

of RED, researchers have fabricated new membranes and implemented improved stack design of RED cell [90, 80, 91]. Designing a nanocomposite membrane with organic and inorganic components, Hong and Chen reported a power density of 1.3 W/m^2 [92]. More recently, Zhang et al. [93] reported considerable improvement in power generation through RED by use of resin beads packed compartments as nano-confinements, instead of traditional ones.

To achieve the fundamental understanding and efficient design of RED cells, several numerical investigations of RED were undertaken. To this end, most of the numerical work focused on the analysis of a single nano-confinement (nanopore or nanochannel), instead of an entire membrane for computational simplicity [4, 94, 5]. Assuming insignificant effect of electrokinetic flow on RED electrical characteristics, Kim performed a two-dimensional numerical analysis of RED and concluded that power generation can be maximized by minimizing the cross-sectional area, increasing surface charge density, and optimizing the length of the charged nanochannel [4]. This study was improved by Kang et al. by inclusion of electrokinetic flow [5]. In this investigation, Kang et al. modelled a numerical simulation of RED using anodic alumina nanopores with experimentally determined values of surface charge density. They reported an increase of the diffusion potential and a decrease of electrical conductance with an increase in nanopore length. With optimized design parameters, they achieved a power output density of 9.9 W/m^2. However, Kang et al. did not analyze the effect of external flows, which can be frequently encountered in steady-state experimental models of an RED cell. In this doctoral thesis, we numerically investigate RED through a single charged nanochannel without neglecting the effect of external flows through the reservoirs.

On the experimental front, investigations of RED power generation was performed using various charged membranes, such as microfiltration membranes [95], polymeric membranes [96, 97], silica nanochannels [98, 99, 100], porous diaphragm [101] and Al_2O_3 membrane [102]. One such membrane which demonstrates excellent charge-selective characteristics is the Nafion membrane. Previous investigations using the Nafion membrane focused on the electrokinetic energy conversion characteristics [103], and the effect of temperature [104]. Our experimental investigation reports a detailed analysis of state-state electrical measurements of a RED cell using a Nafion membrane for different concentration difference across the membrane and

different solution inflow rate.

RED pilot plant:: In order to test the feasibility of power generation from salinity gradient, a pilot plant was installed in Afsluitdijk, The Netherlands, in 2014 [105, 90, 106]. This plant has the capacity of generating 50 kW of power, with a power output density of 2.6 W/m^2. Through this pilot project, it was estimated that the total potential of electricity generation through this process for The Netherlands alone is 200 MW, which is about 5% of the total energy consumption.

1.5 Overview of the thesis

The present doctoral study deals with numerical and experimental study of flow through charged, nanochannels, with particular focus on its applications in the area of renewable energy generation. Since three out of the four studies performed in this doctoral thesis involves numerical simulations, the details of the basic numerical modeling framework, performed in COMSOL is presented separately in Chapter 2.

Chapter 3 reports diffusioosmotic flow in a straight nanochannel. In this chapter, we focus on the change in the flow direction of the solution with the change in control parameters. For the first time, a non-dimensional number based on nanochannel parameters has been proposed with can predict the flow direction in a nano/micro-junction.

Chapter 4 concerns the diffusioosmotic flow in a charged, tapered nanochannel, where we have investigated the effect of the angle of taper on the flow magnitude and direction. In addition, the impact of other vital parameters, such as nanochannel tip diameter, length concentration difference, and the flow rate has also been investigated.

In Chapter 5, we analyze one of the engineering application of ionic interactions of electrolytes through nanochannels, by studying its power generation capacity through RED. In this analysis, we investigate the key parameters affecting the power output of a RED cell and report a power-law dependence behavior of internal resistance and power output density on external concentration difference. Through our simulations we aim to develop a better understanding of variation of energy conversion efficiency and power density with solution

concentrations, concentration gradient, nanochannel dimensions, and flow rate.

Lastly, the experimental observation of power generation through a RED cell was reported in Chapter 6. In this chapter, we discuss the use of the Nafion proton-selective membrane to capture energy from solutions of different salinity.

Chapter 2

Numerical model

A significant part of the present doctoral thesis was undertaken through numerical investigation of ionic flows through nano-confinements. Hence, a detailed description of the numerical model is quintessential. The numerical models were implemented using the commercially available finite element-based numerical simulation software, COMSOL Multiphysics 5.3a [1]. A few advantages of using COMSOL Multiphysics can be listed as follows:

- No requirement for any other external applications or meshing software, since COMSOL Multiphysics is a complete package which includes built-in meshing application and solver. Only in case of complicated geometry, there may be a need to use specialized design software.
- COMSOL offers easy coupling of multi-physics problems. The user gets to choose whether he/she wants to implement a full coupled solution or partial coupling of the solutions.
- COMSOL can help with an easy tackle of solving complex problems in a complex (fluidic) geometry, which often presents numerical challenges for common direct numerical simulation methods based on a finite difference scheme.
- It is possible to easily switch between simple (with physics-defined mesh), and complicated models (with refined user-defined mesh).

- COMSOL Multiphysics a user-friendly graphical user interface, where the user decides how much details of the simulation and solver he/she will be working.

- Even though simulation time depends a lot on the system configuration, COMSOL Multiphysics, through an efficient in-built selection of best numerical approach, provides the simulation results in relatively less time.

However, like every numerical software, there exists some limitations of COMSOL. Some of them are relatively less control on meshing, and complicated process of creation of the model geometry. In this project, we are dealing with a multi-physics problem that involves coupled solution of Poisson's, Nernst-Planck and Navier-Stokes equations. Since COMSOL Multiphysics is an excellent numerical tool for analyses involving multiple physical phenomenon, this software was a reasonable good option.

The following section provides details of the simulation flowchart that was followed for our numerical investigation. Section 2.2 describes the geometrical model for diffusioosmotic flow in a straight channel, and a RED cell used for investigating renewable power generation from a salinity gradient of electrolytes of different salt concentration. The grid Independence study was also conducted for this numerical analysis and has been reported in Section 2.3. All our numerical models have been benchmarked by comparing our results with existing analytical and numerical results of simplified models related to diffusioosmotic and electroosmotic flows, which is elaborated in Section 2.4.

The geometry, boundary conditions, and benchmarking of tapered nanochannel are not reported in this chapter, but on chapter 4.

2.1 Simulation Flowchart

A graphical representation of the simulation procedure, identifying the key elements and interrelationships can be conveniently illustrated through a model flowchart. Thus, a basic flowchart for our numerical simulations is provided in Fig. 2.1. Each key computational step listed in the flowchart is elaborately described below [1]:

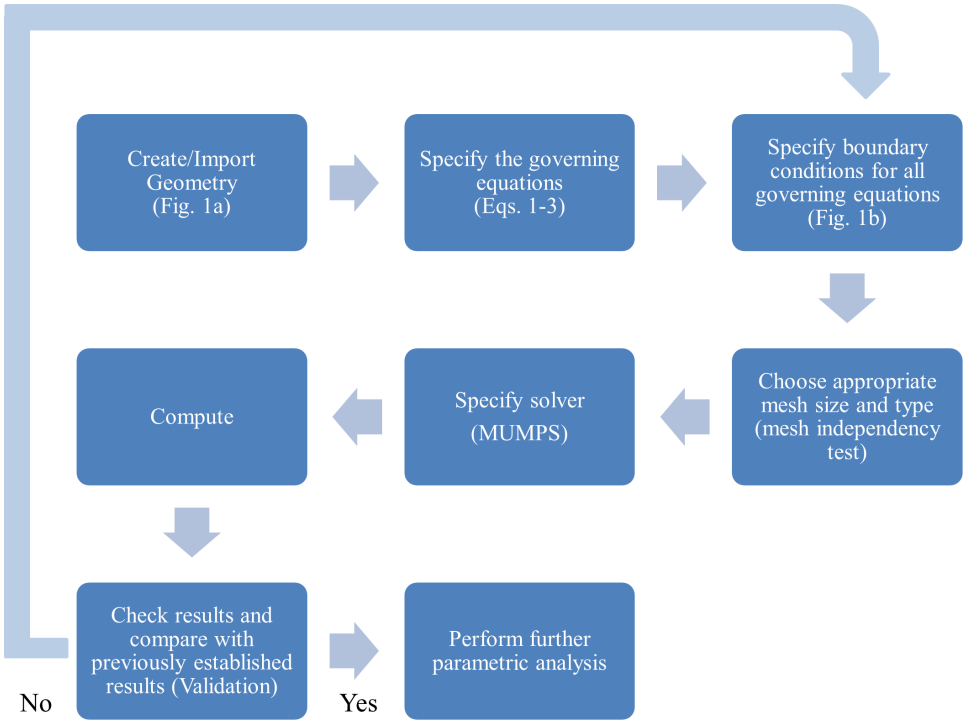

Figure 2.1: Flowchart of our numerical procedure. The simulation is implemented in COMSOL Multiphysics 5.3a.[1]

1. **Governing equations**: The very first step for any numerical modeling is the mathematically formulate the problem. In this regard, we first identify the governing equations for our problem. For the analysis of a steady-state RED problem with a single nano-confinement, Poisson's, Nernst-Planck and Stokes equations are used to solve for electrical potential, ionic concentrations, and flow fields.

2. **Geometry**: The second step for numerical modeling in COMSOL Multiphysics is to create the geometry of the problem. We investigated a 2D model of reverse electrodialysis to study ionic flow and electrical output using a positively-charged nanoslit. Our geometry consists of a single nanochannel and two reservoirs, through which solutions of different salt concentrations flow. This particular configuration can be treated as micro/nano-junction, where the reservoirs represent the microchannels.

3. **Boundary conditions (BCs)**: This step in probably the most critical undertaking for the numerical model. After careful analysis of the actual experimental system, the boundary conditions for each boundary of the computational domain has to be decided for all the governing equation such that it can provide outputs which is comparable to experimental observations. The boundary conditions for the governing equations of the present problem were decided based on the underlying physical mechanisms and reasoning as well as previous numerical models of RED without external flow [4, 5] and other experimental reports which concern the BCs for modeling surface charges of nanopores [107, 108] and flow field (with no-slip and no-penetration BCs) [109].

4. **Mesh independency study**: It is an essential step to check the mesh independence of the numerical simulation models. Starting for a course mesh (with less number of elements), we gradually increase the mesh size until we do not observe any variation in the results with further increase in mesh. We identify the mesh size after which there is no significant change in output. Henceforth, we always use a mesh with has equal to or greater number of elements than the identified mesh size. In this project, we systematically increased the total number of elements in our numerical simulation to examine the reproducibility of some important output parameters.

5. **Solver**: For the current analysis involving multiple physics, COMSOL uses a multifrontal massively parallel solver (MUMPS), which is a direct solution method, based on Gaussian factorization [110]. MUMPS is an algorithm based on a multifrontal approach to solve linearized equations of the form of $Ax = b$, where A is the (differential operator) coefficient matrix, x is the vector of desired variables to be solved for, and b is a known vector calculated based on the numerical, discretized differential equations used. The solution technique of MUMPS can be broadly divided into three parts [110]:

   (a) **Analysis**: This is the pre-processing stage, where the solver decides on the particular Gaussian factorization method to be used by analysis of the matrix, A (i.e., checking whether the matrix, A, is diagonal, symmetric, etc.) to simplify the solution method used.

   (b) **Factorization**: In this step, the matrix, A, is factorized into either $A = LU$ (where L and U are lower and upper diagonal matrices, respectively) or $A = LDL^T$, where D is a diagonal matrix, and the superscript T denotes transpose of a matrix.

   (c) **Solution**: At this stage, the factorized matrices are solved to obtain the final solution, x for the linearized set of equations, $Ax = b$.

6. **Computation**: As already discussed, we have used the commercially available software, COMSOL Multiphysics 5.3a, for our numerical computations. This software uses finite element method to solve numerical problems, using various algorithms and solvers. We have used the built-in MUMPS solver described above.

7. **Validation**: Validation forms an essential step for any numerical simulation, where we develop credibility of our model by comparing with previously established analytical, numerical, and/or experimental results from the literature, or our experiments. This step helps build trust and confidence in our model. Due to the absence of experimental results on such miniature nano-confinements, we validated our model with previous analytical results and numerical findings (see Section 2.4 for details).

8. **Parametric analysis**: After the benchmark of our numerical model, we systematically

vary the various parameters and study the resulting electrical characteristics of the RED cell, and the corresponding flow. In our problem, we analyze the effect on output characteristics for change in model parameters, such as nanochannel height, h, nanochannel length, l, and concentration difference, Δc.

2.2 Model geometry

The basic geometry of our problem is shown in Fig. 2.2. The positively-charged nanochannel connects the left-hand and right-hand reservoirs. The far end of the reservoirs are fitted with electrodes for electrical signals. Solutions of different concentration flows through the two reservoirs at the same flow velocity. Through the left-hand reservoir flow a solution of higher salinity, whereas a dilute solution flows through the right-hand reservoir. The charged nanochannel allowed preferential exchange of ions between the two reservoirs. This problem involves interactions among various ions, electrical voltage distribution, and the effect of flow of solution, which can be represented by simultaneous solution of the Poisson's, Nernst-Plank, and Stokes equations. Generally, the continuum model is still valid for liquids in nanofluidics when dimensions are not less than 5 nm [111]. In accordance with this hypothesis, we have kept the geometric parameters in our model more than 5 nm for all our cases.

2.3 Mesh independence studies

We verified the reproducibility of our numerical results by performing mesh independence checks for the current-voltage (I-V) characteristics of the RED model. We plotted the linear I-V curves for different mesh sizes and total numbers of elements, shown in Fig. 2.3, and further confirmed the mesh independence with the values of open-circuit voltage, ϕ_0 and nanochannel resistance, R_c, summarized in Table 2.1. It can be seen that the reproducibility of the results is enhanced significantly (with around 5% variation) when the total number of elements is greater than 20,000, which was used for all the computations presented. We describe the uncertainty analyses performed during our simulations to ensure systematic and

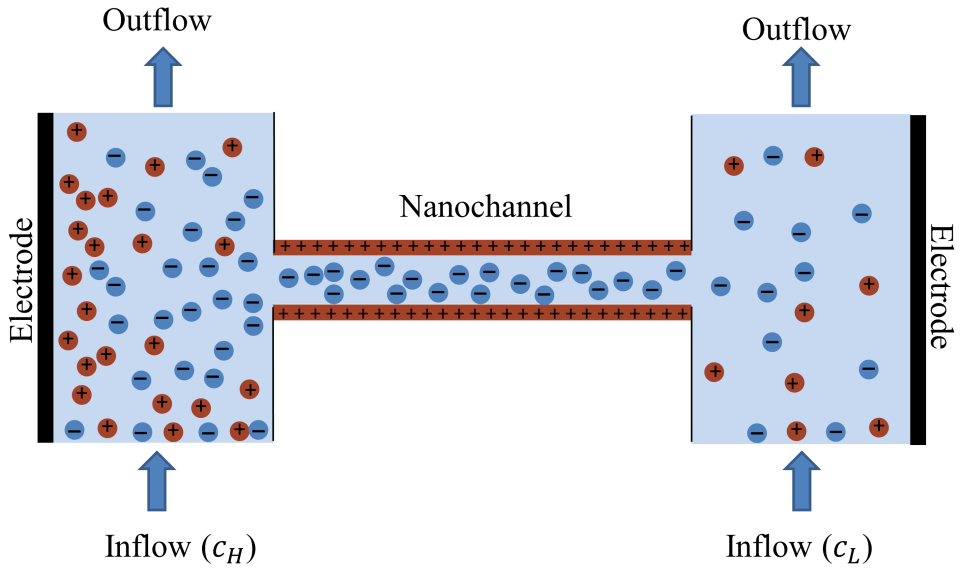

Figure 2.2: Schematic of the model geometry that was implemented in COMSOL

consistent results in 2.5.

When the total number of elements is greater than 20,000, the reproducibility of the results is enhanced significantly (with deviations within $\approx 4\%$). Therefore, the typical mesh number for all computations were greater than 20,000.

2.4 Validation

The present numerical configuration is a 2D steady-state problem using Cartesian coordinates. The numerical study has been implemented using a finite element method with COMSOL Multiphysics (version 5.3a) [1]. We validated our numerical model based on previous analytical as well as other numerical solutions of a simplified model.

2.4.1 Benchmark with analytical results

Analytical description of 1D electrokinetic flow in a narrow capillary of a surface potential under an external electrical field (without external reservoir flow and concentration difference) was previously reported [2, 112]. We computed similar situations by modifying our present

Total number of elements E_{total}	**Open-circuit voltage** ϕ_0 (mV)	**Internal resistance** R_c $(M\Omega)$
2156	89.58	113.84
5472	73.30	193.07
6738	58.96	190.74
11752	141.52	252.46
17536	115.06	249.01
21582	114.89	264.49
26918	118.12	253.61
29952	108.81	249.15

Table 2.1: Mesh independence studies based on the current-voltage data of the RED cell, revealing the changes and convergence of electrical outputs, ϕ_0 and R_c, with increasing the total number of mesh elements.

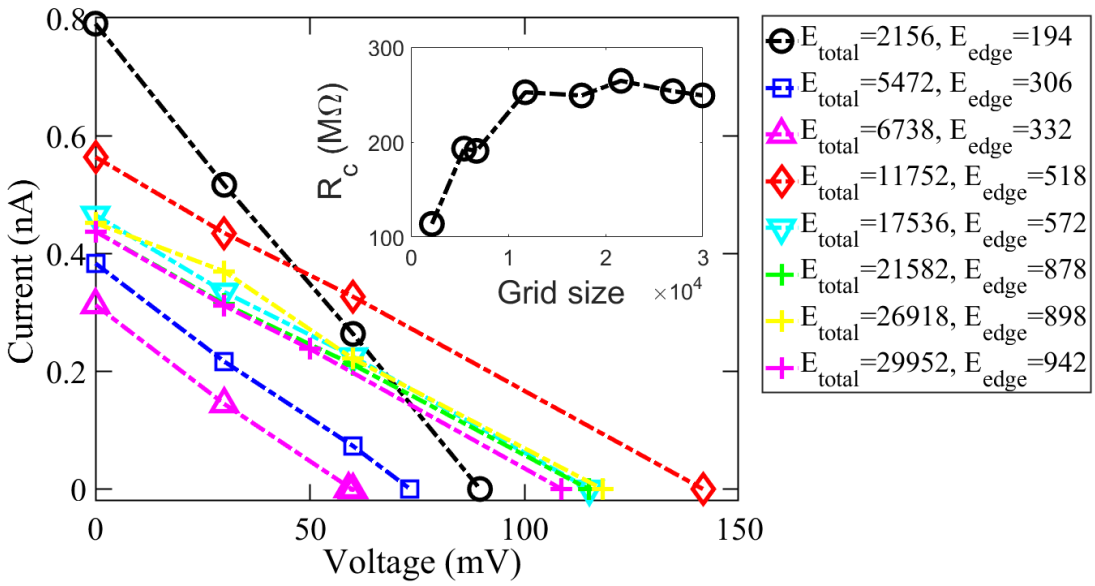

Figure 2.3: Mesh independence studies showing consistent results obtained when the total number of elements (E_{total}) is greater than 20,000 and the number of edge elements (E_{edge}) is larger than 850.

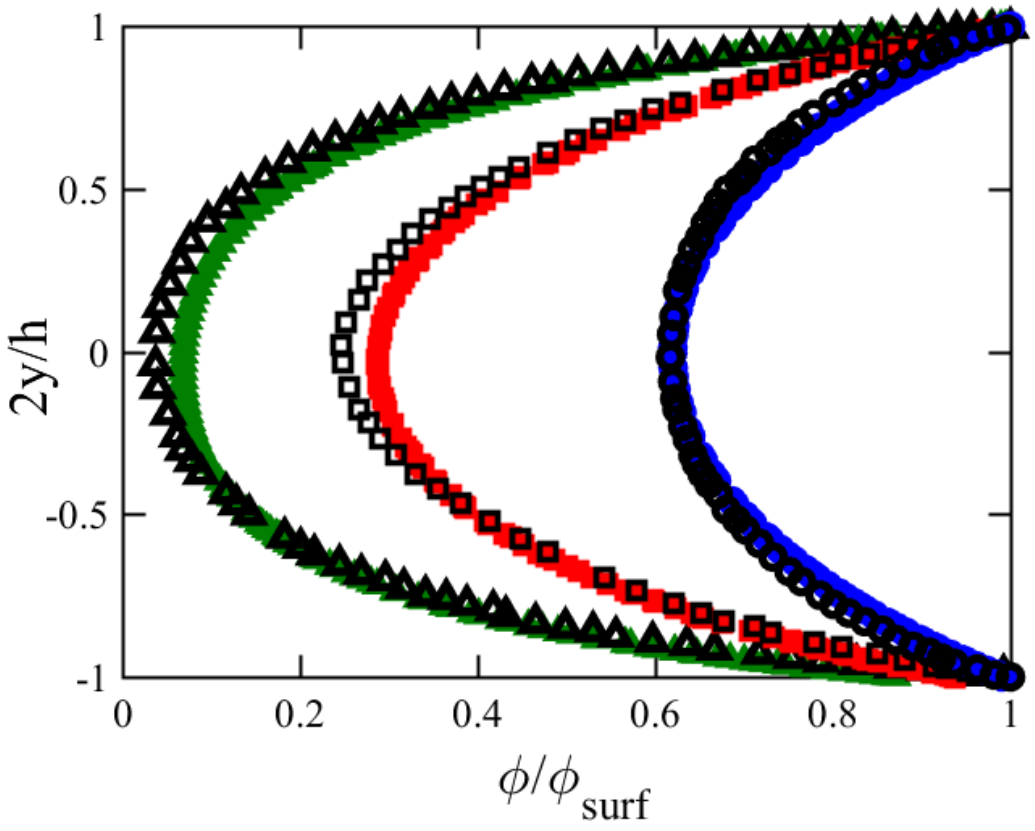

Figure 2.4: Comparison of non-dimensional electric potential along the transverse direction (y-axis) of our two-dimensional (simplified) numerical simulation with one-dimensional analytical results of electrokinetic flow under an external electric field without external flow nor external concentration difference, reported by Burgreen and Nakache [2]. The numerical results are shown for different electrokinetic radii of $h/\lambda_D = 1$ (●), 2 (■) and 4 (▲), compared with the corresponding analytical results (○, □, and △, respectively) by Burgreen and Nakache [2].

simulation model (but using the current 2D computational domain), with a surface charge $\sigma \approx 1.55 \times 10^{-4}$ C/m^2, which corresponds to a constant zeta potential [113] of 23.5 mV (used in Fig. 2 of Ref. [2]) along the charged nano-channel without external reservoir flow. Shown in Fig. 2.4 is the comparison of the analytical and our simulation results of the electric potential profile across the fine channel. Albeit different computational geometries used, the comparison between the simulation and analytical results by Burgreen et al. [2] show good agreement, with the percentage relative error of $\approx 5\%$ for the different cases of h/λ_D = 1, 2, and 4.

We first validated our numerical model with the analytical solution of electrokinetic flow

of a dilute electrolyte under an external electrical field by Burgreen and Nakache [2] In the theoretical analysis without any external flow or concentration difference, they formulated the generation of streaming potential in fine capillaries and analyzed the dependence of the resultant flow on the channel radius and Debye length. This 1D analytical simulation, based on surface potential, ζ, has been compared with our 2D numerical simulation, based on surface charge density, σ, using the well-known Grahame relation: $\sigma = \epsilon_0 \epsilon_r \zeta / \lambda_D$ [114]. Illustrated in Fig. 2.4, the transverse electric potential profile (non-dimensionalized with the surface potential, Φ_0) of our (simplified) 2D simulation agree well with the 1D analytical solutions of the electrokinetic flow by Burgreen and Nakache [2] (maximum deviation $\simeq 5\%$).

2.4.2 Benchmark with numerical results

Kim previously studied electric outputs of a RED process without considering flow field [4]. Our model, with required adjustments in the governing equations and boundary conditions, provides consistent results with theirs. Fig. 2.6a illustrates good agreement between our test results and those reported by Kim [4] concerning the average concentration profiles. As shown in Fig. 2.6b, the overall profile for average electric potential agrees well (except near the end of the nanochannel at $x > 200$ nm with a deviation of $\approx 10\%$).

In addition, we benchmarked our simulation with an investigation of electrohydrodynamic transport by Pivonka et al. [3]. They reported transport of ionic solution across a negatively-charged slit opening subjected to an electrolyte concentration gradient, but without external electrical forcing. The nano-slit was connected to two steady reservoirs with no external flow (i.e., $v_f = 0$). With appropriate modifications in our simulation, by implementing $h = 10$ nm, $l = 150$ nm, $\sigma = -0.01$ C/m^2, $c_L = 10$ mM and $c_H = 20$ mM, we compared our results with those of Pivonka et al. [3]. Shown in Fig. 2.5 are the simulation results of the average cation and anion concentrations over the cross-section (in (a)) and average electric potential (in (b)) along the nanochannel. The average cation and anion concentrations between the two numerical models agree well, whereas a 10% deviation of average electric potential is present at the junction of the left reservoir and nano-slit. We further investigated this discrepancy, and compared the membrane potential (i.e. the potential difference across the nanochannel)

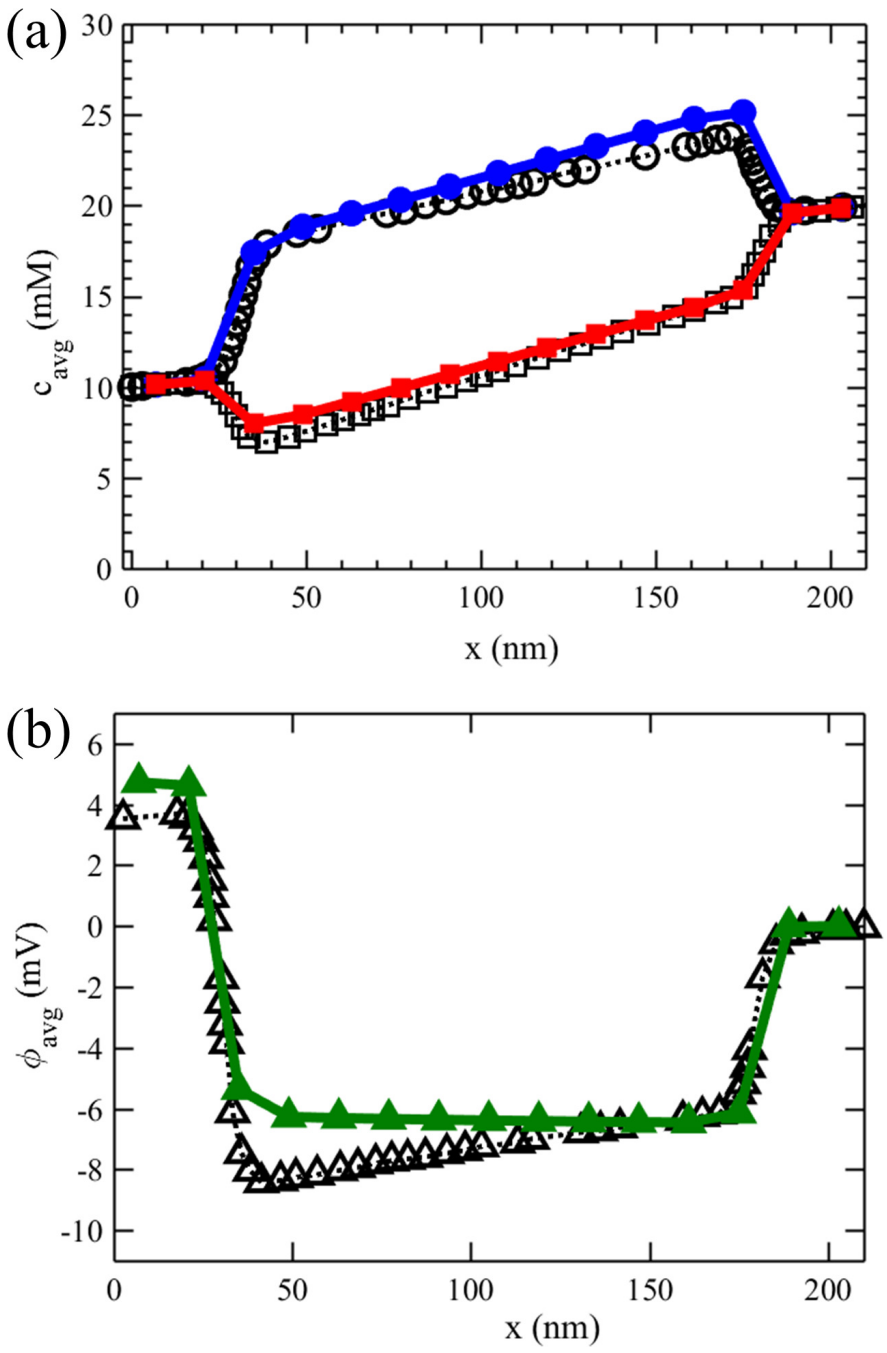

Figure 2.5: (a) Average cationic (●) and anionic (■) concentrations, and (b) average electric potential (▲) obtained by our simplified numerical model of diffusioosmotic flow without external flow (i.e., the current model for steady reservoirs, but with $v_f = 0$). The corresponding comparisons are done based on the numerical results (○, □, and △) by Pivonka et al. [3]. Here, we investigated a 2D steady diffusioosmotic flow through a negatively charged slit (of height h = 10 nm, length l = 150 nm, and surface charge density σ = -0.01 C/m^2). The nano-slit is connected to two reservoirs (of dimensions 30 nm × 30 nm) with electrolyte concentrations of c_L = 10 mM and c_H = 20 mM.

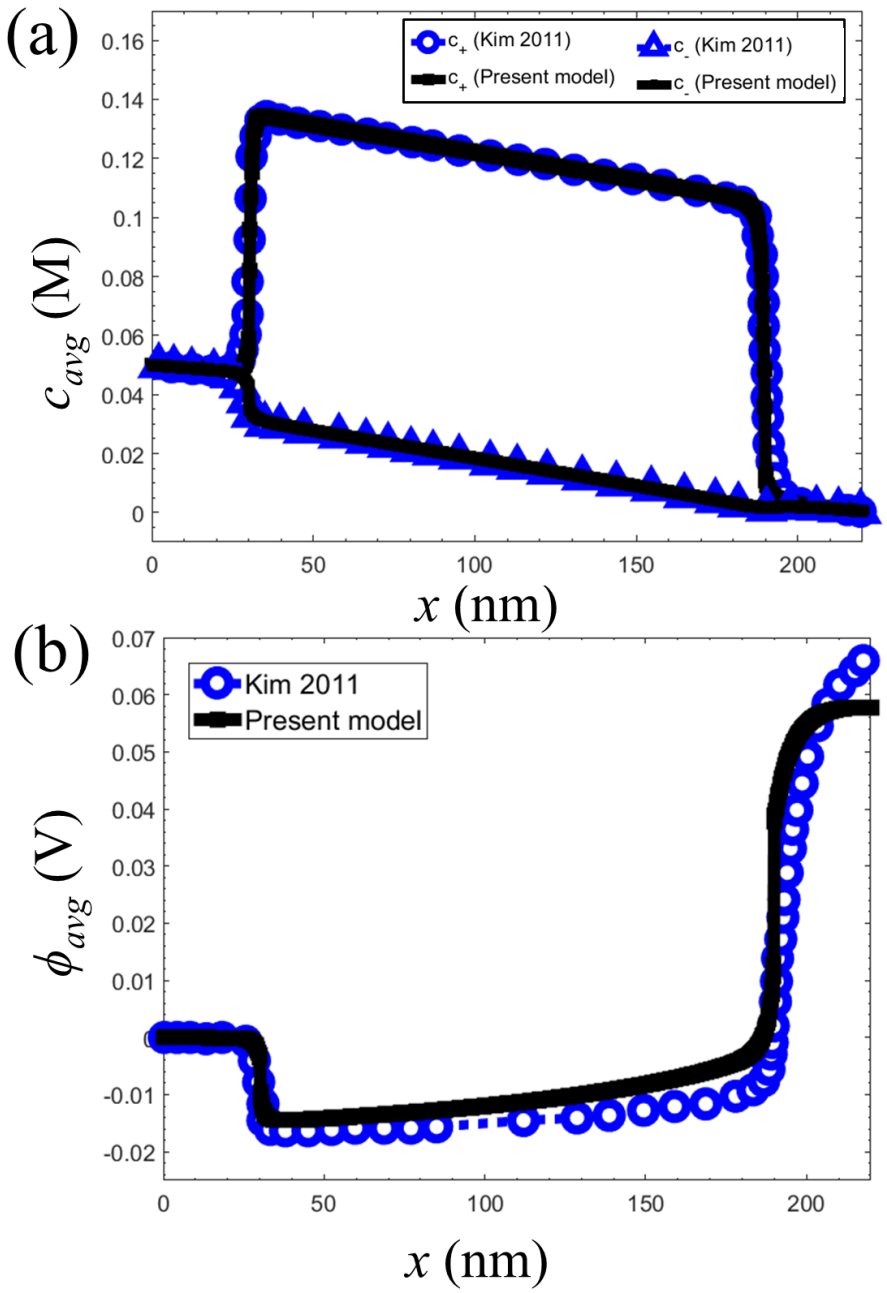

Figure 2.6: Comparison of the current numerical results with those of RED model without external flow (v_f = 0) by Kim [4], revealing good agreements of (a) average concentration of the cation, $c_{+,avg}$ (○) and anion, $c_{-,avg}$ (△) and (b) average electric potential, ϕ_{avg} (○), for h = 20 nm, l = 160 nm, c_L = 0.5 mM, c_R = c_H/c_L = 100. Here, these simulations use a negative surface charge density, σ = -0.1 C/m^2.

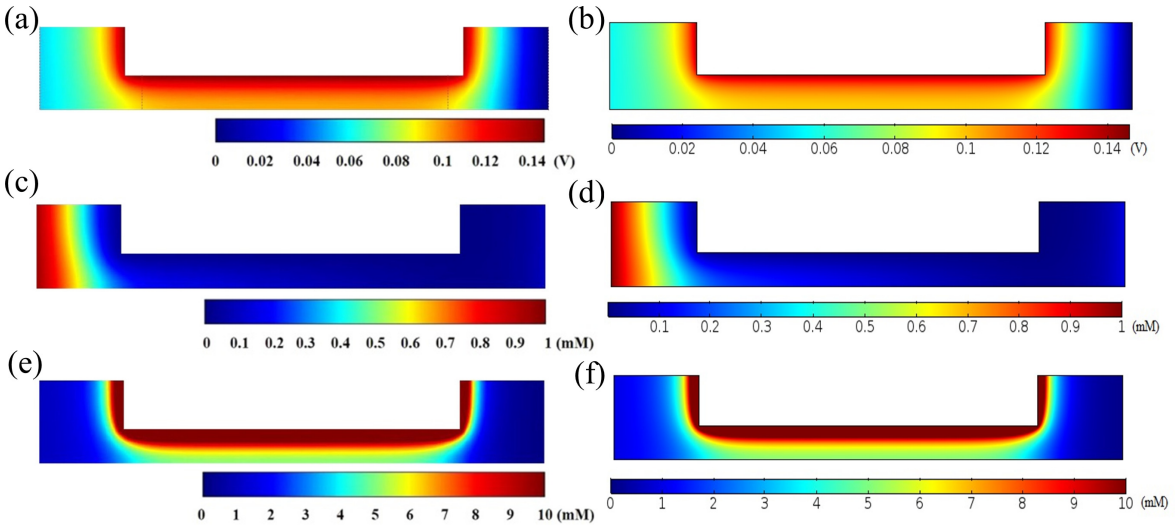

Figure 2.7: Validation of the present numerical model based on the results by Kang et al. [5] $h = 10$ nm, $l = 100$ nm, $c_L = 0.1$ mM, $c_R = c_H/c_L = 10$, $\sigma = 0.01$ C/m^2, and $I_c = 0$. (a) Electrical potential profile, (b) cation concentration, and (e) anion concentration reported by Kang et al. The corresponding results by our simulation are shown in (b), (d), and (f), respectively.

from our results ($\Delta\phi \approx 4.8$ mV) with results reported by Westermann-Clark and Christoforou [115]($\Delta\phi_2 = 5.7$ mV), which demonstrated a better agreement when compared to Pivonka et al. (≈ 3.2 mV).

We further validated our COMSOL simulation by a comparison with the results reported by Kang et al. [5]. As shown in Fig. 2.7, we found a good agreement between Kang et al. findings [5] and our results for a simplified model without external flow.

2.5 Uncertainty Analysis

In the previous section, mesh independence tests were done with respect to the I-V data of the nanochannel RED, such as open circuit voltage and internal resistance. Mesh with more than 20,000 elements demonstrated about 5% variation with simulations using highest number of elements (≈30,000). Systematic uncertainty for our simulation was minimized by fixing the relative tolerance to be 10^{-2} for all our simulations. Our simulations in COMSOL were terminated when the relative error of computed variables becomes less than the relative

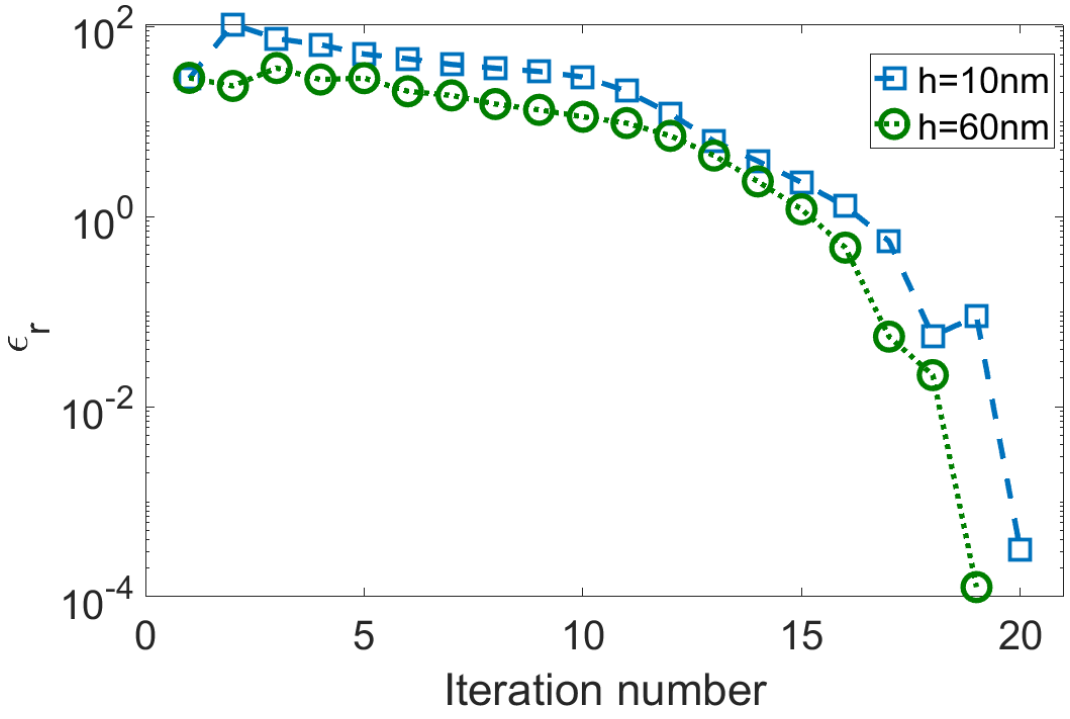

Figure 2.8: Representative curves illustrating variation of error, ε_r with iteration number for our numerical simulations for different nanochannel heights, $h = 10$ and 60 μm.

tolerance. Relative error, ε_r, is calculated using the weighted Euclidean norm [1], as follows:

$$\varepsilon_r = \sqrt{\frac{1}{M}} \sqrt{\Sigma_{j=1}^{M} \frac{1}{N_j W_j} \Sigma_{i=1}^{N_j} (E_{i,j})^2}, \tag{2.1}$$

where M is the number of fields, N_j is the degree of freedom in each field, W_j are the weights determined from the residuals, $E_{i,j}$ is the current residual. Fig. 2.8 shows representative curves of calculated relative error, ε_r, varying with each subsequent iteration for two different channel heights, $h = 10$ and 60 nm. To determine the appropriate relative tolerance value for our simulations, a number of simulations for a sample numerical result were tested with relative tolerance varying from 10^{-1} to 10^{-6}. It was observed that reducing the relative tolerance value below 10^{-2} did not have a significant impact of the numerical results. Hence, a relative tolerance of 10^{-2} was used for our simulations. For majority of our numerical simulations, the relative error was less than 10^{-3}, as shown in Fig. 2.8.

Chapter 3

Diffusioosmotic flow in nano-confinements

3.1 Introduction

Nanofluidic transport has lately attracted significant interest due to the advent of nanofabrication [116, 117, 118, 119] as well as its beneficial surface-dominant (or induced) effects [120, 55, 8, 121]. For instance, nano-slits (typically of the order of 10 – 100 nm) can become charge-selective due to overlapping electrical double layers (EDLs) in an electrolyte solution and, hence, allow electrical interaction and manipulation [117]. This underlying mechanism has recently been applied to various promising applications of nanofluidics for desalination [98, 122, 123, 124], membrane technology [23, 125], cell biology [126, 118], and sustainable energy using reverse electrodialysis [5, 101, 127, 128, 129]. Nanoflow generally can be driven or manipulated by several external forcing mechanisms, such as, via temperature difference [130, 131], capillary action [132, 133] or external electrical field [121, 47, 134]. For example, the electroosmotic flow (EOF) is commonly used, and is driven by an external electrical field and affected by the induced ion distribution within the EDLs along a charged surface [24]. Less attention, however, has been given to the flow generated across a charged nano-confinement under an electrolyte concentration gradient [135, 38, 49]. This so-called diffusioosmotic flow

(DOF) is a combination of two effects: namely, chemiosmosis and electroosmosis. chemiosmotic flow is fluid motion due to diffusive flow which induces a pressure gradient under an electrolyte concentration gradient along the charged surface [136, 137, 138], whereas the motion due to the electrical interactions between spatial charges and the electrical field induced within the double layers is termed as electroosmosis [139, 140, 141]. On the other hand, motion of a charged colloidal particle under such a concentration gradient in the solution is termed as diffusiophoresis [47, 49].

Most previous analytical studies of diffusioosmosis considered an electrolyte solution subjected to a concentration gradient along a homogeneously-charged surface, with simplified 1D Poisson-Boltzmann distribution of electrolyte concentration [142, 136, 137, 143, 45, 144, 145]. Keh et al. reported a closed form expression of diffusioosmotic velocity of the electrolyte, equating the net equilibrium force acting on the solution to zero [136]. In the limit of small zeta potential or wall surface charge density, Keh et al. found a monotonic increase of diffusioosmotic flow with increasing zeta potential [136]. Keh et al. further demonstrated the non-linear increase of diffusioosmotic velocity with decreasing porosity in a charged porous medium with a 1D formulation of diffusioosmotic velocity as a function of EDL thickness, ion diffusivities, and pore diameter [137, 45].

Another unique characteristics in nanofluidic flow is the phenomenon of ion concentration polarization (ICP) observed in specific geometries. The phenomenon of ICP is indicated via a strong concentration gradient (or polarization) of the electrolyte concentration within a nano-confinement [146, 147]. For instance, under d.c. bias, concentration of a cation-selective membrane could deplete significantly in the anodic side, resulting an ion-depletion zone. Simultaneously, the cathodic counterpart can become highly concentrated to form an ion-enrichment zone [124]. Motivated by bio-sensing and bio-medical applications exploiting ICP in nano-confinements, recent numerical investigations consider 2D configuration of micro-nano junctions to investigate DOF [138, 148, 149]. These studies of 2D DOF problem reveal a significant dependence of diffusioosmotic velocity on surface charge, concentration gradient, and dimensions of the nano-confinement. More specifically, diffusioosmotic velocity was found to increase with increasing surface charge density [148] and increasing nanochannel aspect

ratio [138] whereas demonstrating non-linear dependence on electrolyte concentration [148, 149].

Intriguingly, the reversal of diffusioosmotic flow was found with a small zeta potential of planar charged nanochannel [136, 45], at a low electrolyte concentration [148] or by tuning width-to-height ratio [138]. However, one study reported that DOF in nanopores only occurs from the high concentration reservoir to the low concentration reservoir [149]. In spite of insightful findings by these investigations considering a planar or homogeneous flow geometry, common experimental setups involving nano/micro-junctions [150, 151, 102, 152] are quasi-2D or 3D problems of nano-slits connecting micro-channels and are hardly considered theoretically or numerically due to the complexity of the flow geometry. To fill this literature gap, specifically regarding the better understanding and manipulation of diffusioosmotic nanoflow, we numerically investigate DOF in a charged nanochannel without any external electrical forcing.

Our numerical model consists of two reservoirs with inflow of solutions of different concentrations, connected via a positively-charged nanochannel. The results under various concentrations show a linear dependence of the DOF magnitude on external concentration gradient. The numerical results suggest a critical characteristic dimensionless number that conveniently delineates the parameter regions into different DOF directions for various channel dimensions and surface charge.

3.2 Mathematical modeling

We numerically compute the flow, electrical, and ion concentration fields of a 2D steady-state diffusioosmosis problem, where two steady-flow reservoirs of different electrolyte concentrations (of KCl) are connected by a nanochannel with a constant (positive) surface charge density, σ (see Fig. 3.1). A steady flux of electrolyte solution of high concentration (c_H) is injected through one reservoir (on the left), while a low concentration (c_L) through the other (on the right). Interaction between the two different solutions via the nanochannel is significantly affected by the nanochannel surface charge, resultant electric double layer, and concentration

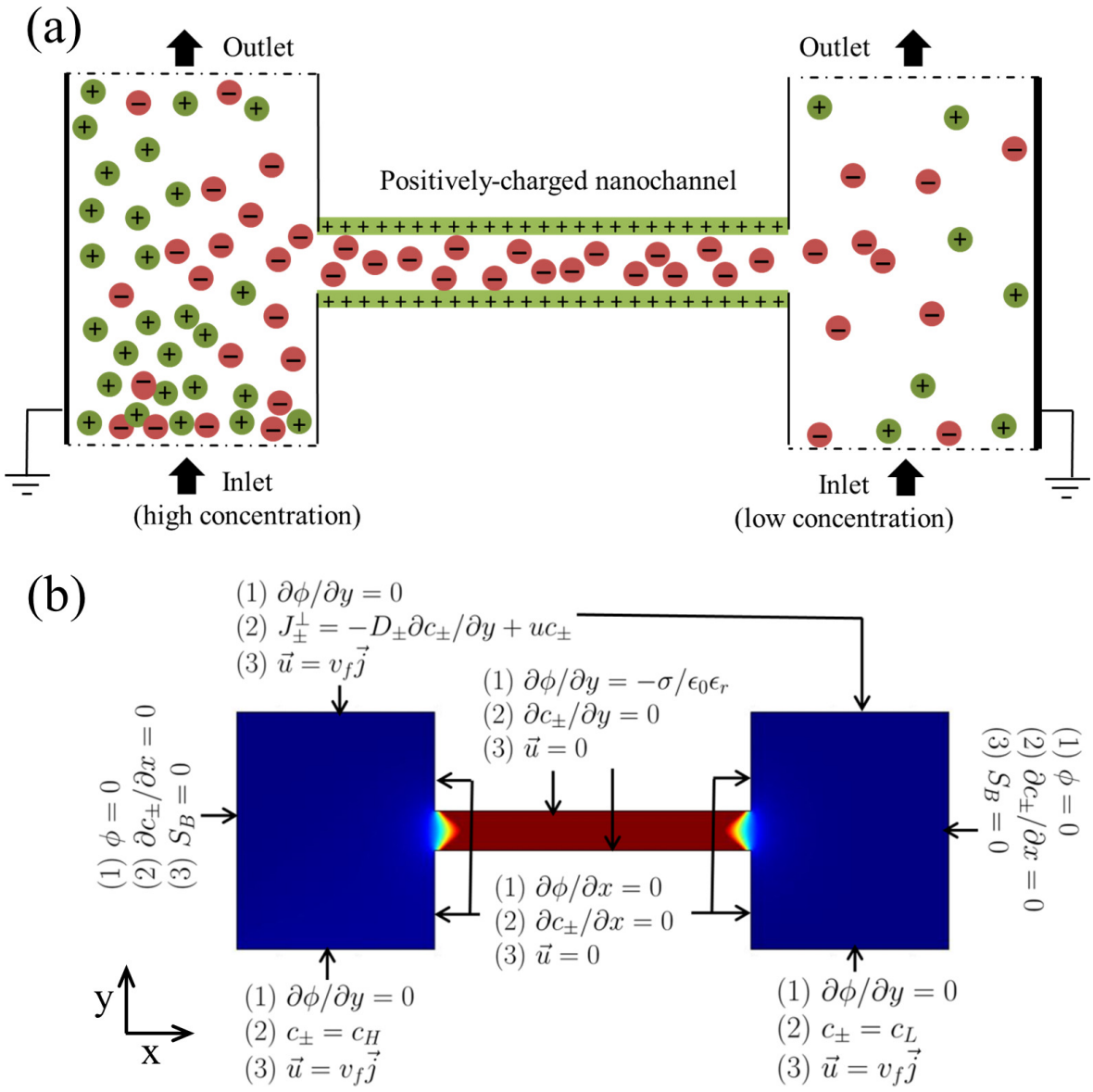

Figure 3.1: (a) Schematic of the simulation model of a 2D diffusioosmotic flow through a charge-selective nanochannel connecting two reservoirs of different electrolyte concentrations; (b) the boundary conditions of the diffusioosmotic flow through a charge selective nanochannel of height (h) and length (l). In (b), the number corresponds to the Eq. number described in the mathematical model (chapter 1).

difference. The thickness of EDL can be characterized by the Debye length, λ_D. For a symmetric monovalent ($z_+ = -z_- = z = 1$) electrolyte, λ_D can be expressed by $\lambda_D = \sqrt{\epsilon_0 \epsilon_r RT/2F^2 c_0}$, where c_0 is the molar concentration of the electrolyte solution [153, 154]. Typical λ_D of our system varies between 10 nm (for $c_0 \approx 1$ mM) and 100 nm (for $c_0 \approx 0.01$ mM), estimated using the average electrolyte concentration in the nanochannel. Narrow nanochannel with overlapping EDL causes the nanochannel to be charge selective due to the repulsion of co-ions and attraction of counter-ions from the charged wall. This charge-selective effect is diminished for wider channel due to insufficient screening of the co-ions (with like charges). Simultaneously, a concentration gradient across the nanochannel due to the difference in electrolyte concentration drives the chemiosmotic transport of the electrolyte solutions. Due to the complex interplay of these different phenomenon, it is fascinating and useful to numerically study diffusioosmotic flow in micro-nano junctions through the conservation of mass, momentum, species and charge.

The distribution of electric potential, ϕ, is governed by the Poisson's equation due to spatial net charges [154]:

$$\epsilon_0 \epsilon_r \nabla^2 \phi = -F(z_+ c_+ + z_- c_-), \tag{3.1}$$

where ϵ_0 ($= 8.854 \times 10^{-12}$ Fm^{-1}), ϵ_r ($= 80.1$) and F ($= 96485$ C mol^{-1}) are the permittivity of a vacuum, relativity permittivity of water, and Faraday constant, respectively. c_+ and z_+ ($= +1$ for K^+ ion) are the concentration and valence of the cation, whereas c_- and z_- ($= -1$ for Cl^- ion) are the concentration and valence of the anion.

The ion concentrations in the solution (i.e., c_+ or c_- for the cation and anion, respectively) are governed by the conservation of ionic species and described by the Nernst-Planck equations. Considering a steady problem, these equations for c_+ and c_- can be modeled as [155, 65]:

$$-\vec{\nabla} \cdot \left(D_\pm \vec{\nabla} c_\pm + \frac{D_\pm}{RT} z_\pm F c_\pm \vec{\nabla} \phi \right) + \vec{u} \cdot \vec{\nabla} c_\pm = 0, \tag{3.2}$$

where T (= 293 K) is the operating temperature, R (= 8.314 $JK^{-1}mol^{-1}$) is the universal gas constant, and D_+ and D_- are the diffusivities of the cation and anion, respectively. Corresponding to the diffusivities of K^+ and Cl^- ions, D_+ and D_- are assumed to be 1.96×10^{-9} m^2/s and 2.0×10^{-9} m^2/s. Physically, the governing Eq. (3.2) describes the conservation of ionic species via diffusive, electromigration, and convective ion-fluxes due to the presence of concentration gradient, electrical forcing, and fluid velocity, respectively, which are represented by the each sequential terms in Eq. (3.2) [24, 65]. The competition among these factors dictates the ionic flux inside the nano-confinement. Integrating Eq. (3.2), we can obtain the cationic (J_+) and anionic (J_-) flux, as shown below:

$$\vec{J}_\pm = \left(-D_\pm \vec{\nabla} c_\pm - \frac{z_\pm D_\pm F c_\pm}{RT} \vec{\nabla}\phi\right) + \vec{u} c_\pm. \tag{3.3}$$

The flow field, $\vec{u}$, is simulated by solving the steady-state Navier-Stokes equations [65, 156], along with the Continuity equation. The Navier-Stokes equations are simplified to the Stokes equations due to the negligible effect of inertia at a low Reynolds number flow (Here, our $Re \approx 10^{-5}$ for l = 100 nm and v_f = 0.01 mm/s):

$$\nabla \cdot \vec{u} = 0, \tag{3.4}$$

$$-\vec{\nabla} p + \mu \nabla^2 \vec{u} \underbrace{-F(z_+ c_+ + z_- c_-)\vec{\nabla}\phi}_{\vec{F}_e = q\vec{E} = -q\vec{\nabla}\phi} = 0, \tag{3.5}$$

where μ is the liquid viscosity (for water, $\mu \simeq 1$ mPa·s at room temperature), $\vec{F}_e$ is the electrical body force, and q ($= z_+ c_+ + z_- c_-$) is the net charge. Eq. sets (3.1)–(3.5) are non-linearly coupled, and we numerically solve for velocity, $\vec{u}$, pressure, p, electrical potential, ϕ, and ion concentrations, $c_\pm$.

The boundary conditions for the governing Eqs. 3.1—3.5 are illustrated in Fig. 3.1b. Along the nanochannel wall, a combination of no-slip ($u_t = \vec{u} \cdot \vec{t} = 0$) and no-penetration ($u_n = \vec{u} \cdot \vec{n} = 0$) conditions are implemented. A constant velocity, v_f, was maintained at the inlet and outlet of the reservoirs in this steady-state model. Solutions of different salt

concentrations (c_H and c_L at left side and right side reservoir, respectively) flow in through the two reservoirs, and interact via the nanochannel due the concentration gradient. This interaction is also affected by the surface charge density of the nanochannel, σ, which was assumed to remain constant and positive for a simulation. This boundary condition can be modeled as: $d\phi/dy = -\sigma/\epsilon_0\epsilon_r$, via the discontinuity of the electrical field in the direction normal to the surface, due to net surface charge [65]. σ was varied as a control parameter. There was no external pressure difference applied to this nanofluidic setup. The boundary stress S_B ($= -p + 2\mu\partial u/\partial n$) was assumed to be zero along the reservoir boundaries as shown in Fig.3.1b.

3.3 Numerical modeling

The numerical simulations were implemented in 2D Cartesian coordinates, based on a finite element model using COMSOL Multiphysics 5.3. We verified our numerical simulations by comparing our results with existing analytical and numerical results of simplified models related to DOF and EOF flows, as explained in details in Chapter 2.

3.4 Results and discussions

We numerically studied the influences of nanochannel dimensions (height h, length l), surface charge density (σ), and electrolyte concentrations (c_H, c_L) on 2D DOF driven by electrical and diffusion processes. For the 2D nano/micro-junction geometry, due to the nonlinear and coupled Eqs. (3.1) – (3.5), we carried out more than 100 simulations in total, by varying the ranges of the key parameters: l = 40 – 160 nm, h = 15 – 80 nm, σ = 0.001 – 0.05 C/m, c_H = 0.01 – 1 mM, with a fixed c_L = 0.01 mM.

3.4.1 Effect of nanochannel dimensions

Shown in Fig. 3.2 are the numerical results for a medium-sized charged-nanochannel of h=60 nm, where the double layers adjacent to the wall do not overlap. Fig. 3.2a shows

the distributions of electric potential, ϕ, as well as the electric field, $\vec{E}$ (in white arrows). The notable variation of electric potential in the transverse direction (i.e. along the width of the nanochannel) demonstrates the non-overlap of EDL. Without an external electric field, the imposed positive surface charge along the nanochannel leads to positive and maximal ϕ adjacent to the charged wall. The electric field $\vec{E}$ ($= -\vec{\nabla}\phi$) directs outward from high towards low electrical potential (i.e., outwards from the nanochannel towards the two reservoirs at the junction). Fig. 3.2b shows that the distribution of cationic concentration, c_+, in our numerical domain. The figure illustrates a higher cationic concentration in the high electrolyte concentration reservoir (of c_H) due to Coulombic repulsion from the positive-charged nanochannel surface. As illustrated in Fig. 3.2c, a net of negative charges merely accumulate close to the positively charged nanochannel, whereas due to comparable cationic and anionic concentrations, a large fraction of of the nanochannel is electrically neutral. Fig. 3.2d reveals that anions accumulate right adjacent to the nanochannel wall because of positive surface charge, and the overall nanoflow field is directed from the reservoir of low towards high concentrations. For a larger h, the electrical neutrality of nanochannel results in weaker electroosmotic effect, and flow is driven primarily by chemiosmosis. Under a concentration gradient between the two reservoirs, water molecules move from c_L to c_H towards equilibrium, thereby producing such flow direction.

Fig. 3.3 shows the numerical results for a narrow channel of height, h = 10 nm. Studying this nanochannel configuration with an overlapping Debye length is important for understanding the inherent mechanism of the charge selectivity and the resultant flow in the nanochannel. The electric potential (ϕ) profile in the 2D geometry is shown in Fig. 3.3a, along with the electric field ($\vec{E}$) in arrows. Due to the overlapping of EDL in this case of h = 10 nm, the variation of ϕ along the width of the nanochannel is less significant when compared with h = 60 nm.

Fig. 3.3b reveals a low cation concentration in the nanochannel since the cations as co-ions are repelled away from the positively charged nanochannel. Therefore, in the high concentration reservoir, cations accumulate in the left bottom corner. On the other hand, as counterions, the anion concentration, c_-, increases significantly inside the nanochannel, resulting in

a net negative charge inside the nanochannel, as illustrated by Fig. 3.3c. The distribution of anion concentration, and velocity profile is shown in Fig. 3.3d. Due to the ion-selective effect of nanochannels with EDL overlap, the cation concentration inside the nanochannel is negligible, and hence the net charge profile (Fig. 3.3c) and the anion distribution (Fig. 3.3d) looks identical. The flow rate inside the nanochannel is from high concentration (c_H) reservoir to the low concentration (C_L) one. Unlike the case of non-overlap of EDL (h = 60 nm), electrical neutrality is not seen in majority of the nanochannel, and electroosmotic flow is dominant. In the absence of external electrical driving force, the local electric field due to surface charge, and resulting charge imbalance directs the overall flow in this narrow nanochannel with EDL overlap ($h = 10$ nm) from the reservoir of high concentration (c_H) to that of low concentration (c_L).

The most striking difference is that the direction of the bulk flow is reversed (from the reservoir of low to high salt concentration) for a relatively wide nanochannel (with a higher h), comparing to that of a narrow ($h = 10$ nm) nanochannel. This reversal of flow direction by tuning nanochannel size can have useful applications of nanofluidic devices for flow control.

3.4.2 Influence of electrolyte concentration difference

The effect of electrolyte concentration gradient on the flow velocity was also studied. Illustrated by Fig. 3.4, the numerical results show that the magnitude of average flow velocity $< |u| >$ in the nanochannel is primarily governed by the concentration difference Δc ($= c_H - c_L$) between the two reservoirs. As shown in Fig. 3.4b, $< |u| >$ increases linearly with Δc. A best least square residual fitting shows $< |u| > \simeq$ 0.88 Δc. The value of this linearly fit coefficient is consistent with that estimated with a characteristic flow velocity, $U = \frac{2RT\lambda_D^2}{\mu}\nabla c$, predicted by Keh et al., for a constant ∇c along a flat charged surface with ions following the Poisson-Boltzmann distribution [137]. To compare with our result, we estimated $\nabla c \simeq \Delta c/l$ and, thus, $U \simeq \frac{2RT\lambda_D^2}{\mu l}\Delta c$. Accordingly, for an average anion concentration of 5.48 mM ($\lambda_D = 4$ nm), the theoretical linear coefficient was estimated to be 0.87, which agrees well with our numerical result.

From our numerical results, surprisingly, Δc does not play an important role in determining

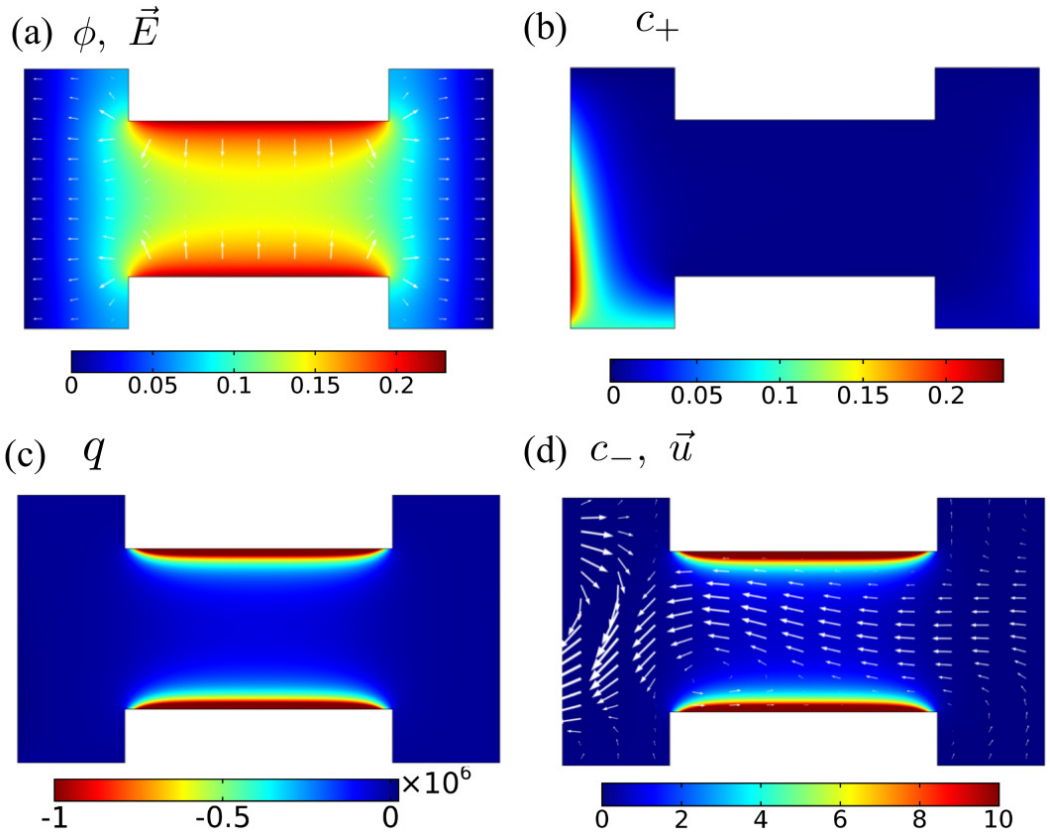

Figure 3.2: Simulation results of diffusioosmosis in straight nanochannels, showing (a) electric potential ϕ (Volts) and field $\vec{E}$ (V/m), in arrows, (b) cation concentration profile c_+ (mM), (c) net charge q (C), and (d) anionic concentration c_- (mM) with velocity field $\vec{u}$, in arrows. For this simulation, we have used nanochannel height, $h = 60$ nm, nanochannel length, $l = 100$ nm, concentration of dilute solution, $c_L = 0.01$ mM, concentration of concentration solution, $c_H = 0.15$ mM, surface charge density, $\sigma = 0.01$ C/m^2, inflow velocity, $v_f = 0.07$ mm/s.

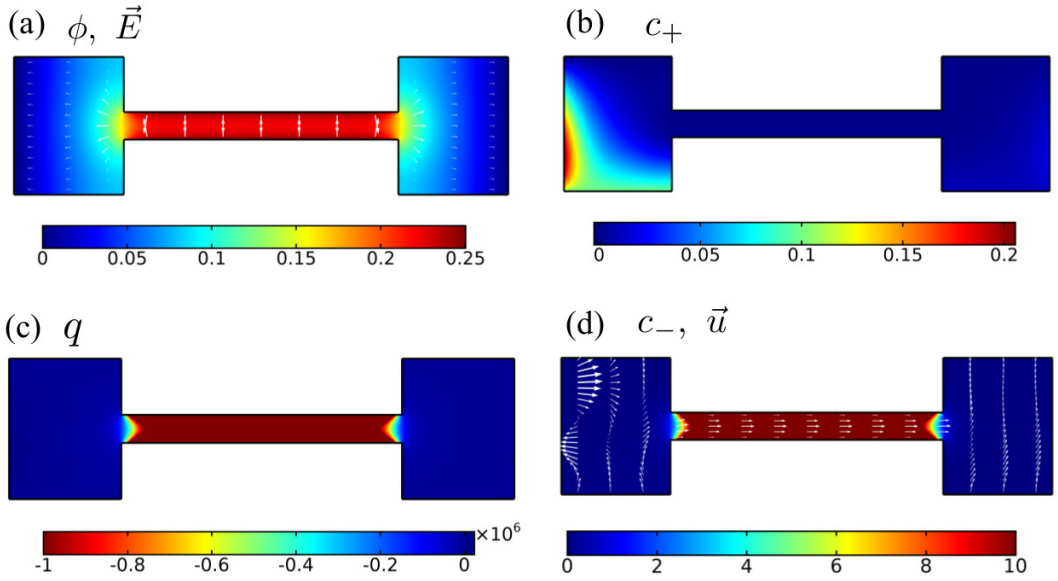

Figure 3.3: Numerical results of the steady-state diffusioosmotic flow in nano/micro-junctions, showing (a) electric potential ϕ (Volts) with electric field $\vec{E}$ (V/m) in arrows, (b) cation concentration c_+ (mM), (c) net charge q ($= z_+c_+ + z_-c_-$) (in C), and (d) anionic concentration c_- (mM) with flow velocity $\vec{u}$ in arrows. The parameters used are $h = 10$ nm, $l = 100$ nm, $c_L = 0.01$ mM, $c_H = 0.15$ mM, $\sigma = 0.01$ C/m^2, and $v_f = 0.07$ mm/s.

the nanoflow direction. Nanoflow in both directions is observed for a wide range of Δc imposed (see Fig. 3.4a). The nanochannel size, on the other hand, influences the nanoflow direction significantly. As shown in Fig. 3.4a, narrower nanochannels (h = 10, 30 nm) tend to have an electroosmosis dominated flow due to the net (negative) charges in the nanochannel with an overlapping Debye length. At the nano/micro-junctions, electrical body force is strong and dominating in the region close to c_H with the electrical body force towards right from c_H to c_L. As a result, the nanoflow moves from the high (c_H) to low concentration (c_L) reservoir. Conversely, for a relatively large nanochannel (e.g. $h = 60$ nm), with a significant fraction of neutral charges, the nanoflow is determined primarily by a diffusion process via an ion concentration gradient, causing the nanoflow ~~to occur~~ from c_L to c_H reservoir.

3.4.3 Controlling nanoflow direction

Our simulation results examining the influence of σ, c_H, c_L, h, and l on a steady-state diffusioosmotic flow show three different modes of flow in the charged nanochannel. These

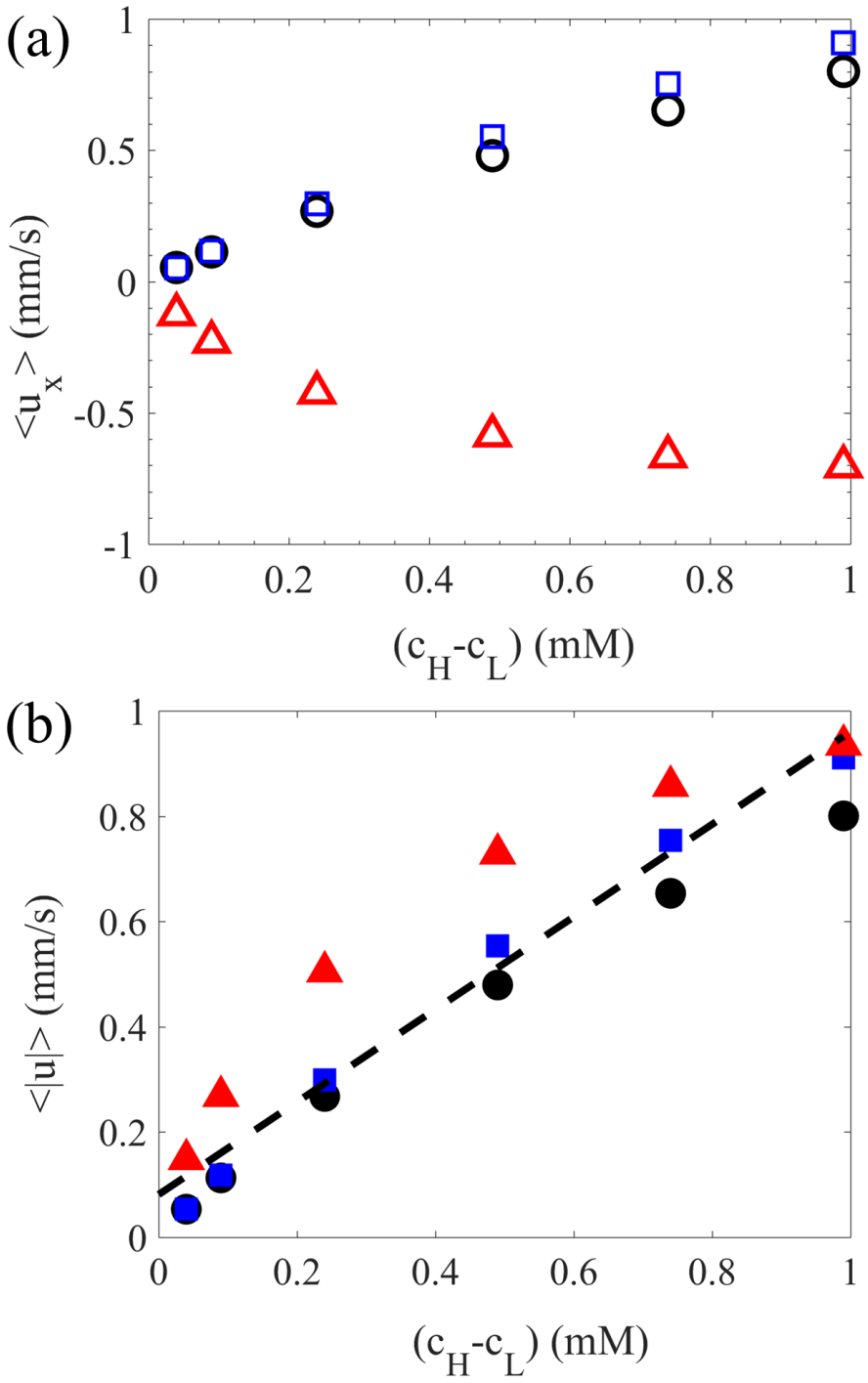

Figure 3.4: Effect of concentration difference on the nanoflow velocity for $l = 100$ nm: (a) Average nanoflow velocity in x-direction, $< u_x >$ and (b) Net average nanoflow velocity, $< |u| >$. Different symbols represent different nanochannel height used: $h = 10$ nm (● and ○), $h = 30$ nm (■ and □), and $h = 60$ nm (▲ and △). The dashed line (- - -) shows the best linear fit, with a slope of 0.88.

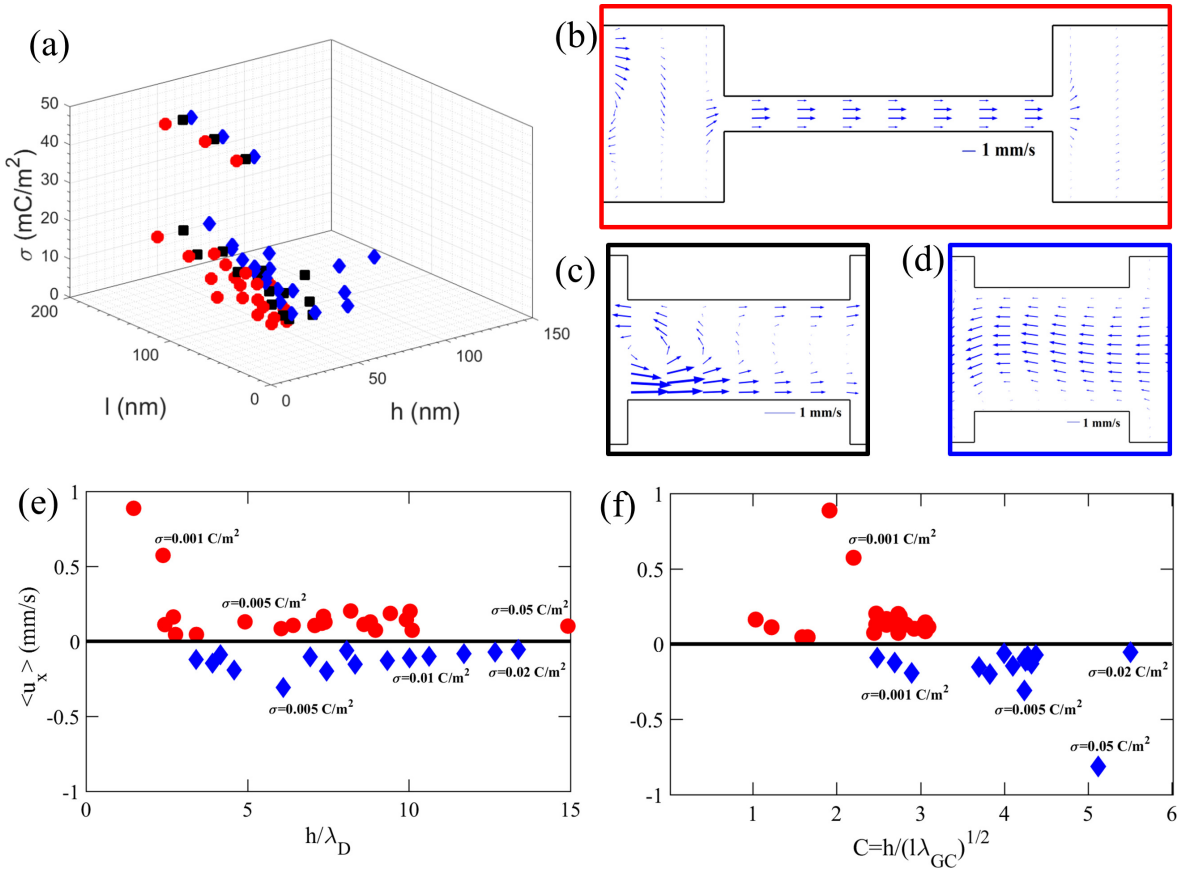

Figure 3.5: (a) Phase diagram of diffusioosmotic nanoflow revealing different flow directions for different nanochannel parameters of h, l, and σ. Flow regime (I), denoted by ●, represents the flow from high to low concentration reservoir; Regime (III) ♦ represents the flow from low to high concentration reservoir; Regime (II), denoted by ■, represents the mixed flow of both directions. Representative flow profiles observed inside the nanochannels are shown for (b) Regime (I), (c) Regime II, and (d) Region III. Variation of (e) h/λ_D, and (f) a critical non-dimensional parameter, C ($= h/\sqrt{l\lambda_G C}$), with average velocity in x-direction inside nanochannel, $< u_x >$. In this analysis, 5 different values of σ in the range of 0.001 – 0.05 C/m^2 have been used, as denoted in (e) and (f).

distinct modes of nanoflow encompass different flow directions: (i) opposite and (ii) parallel to the direction of concentration gradient as well as (iii) a mixture mode of these two directions. By analyzing and plotting different nanoflow regimes against different control parameters, we found that nanoflow direction is primarily controlled by merely a few key parameters for the parameter ranges explored. These major influences are (1) nanochannel height (h), (2) nanochannel length (l), and (3) surface charge density (σ). We noticed that the values of c_H (ranging from 0.001 – 1 mM) and Δc (with a fixed c_L of 0.01 mM) have an insignificant influence on the nanoflow direction.

Revealed in Fig. 3.5 is the influence of diffsioosmosis on nanoflow direction from more than 40 simulations at different h, L and σ, keeping other parameters constant (c_L = 0.01 mM, c_H = 1 mM, v_f = 0.07 mm/s).

Since ion-selectivity of nano-confinements is dictated by the extent of overlap of EDL [23], it is also important to see its effect on DOF. We, thus, investigated the variation of diffusioosmotic velocity $< u_x >$ with h/λ_D, where λ_D is the Debye length (estimated using the average concentration of anions inside nanochannel). However, as evident from in fig. 3.5e, in case of our 2D geometry focusing on micro/nano junction applications, the ratio h/λ_D does not seem to play a vital role in determining DOF direction.

Through the phase diagram analyzing the effects of σ, h and l on direction of diffusioosmotic flow (Fig. 3.5a), and scaling analysis, we found a non-dimensional number, C, which can be used to collapse our data separating different nanoflow regimes and predict the direction of DOF through a nanochannel with the known values of l, h, and σ:

$$C = h/\sqrt{l\lambda_{GC}}. \tag{3.6}$$

where λ_{GC} is known as Gouy-Chapman length, a characteristic length based on the surface charge density σ of the nanochannel, and can be estimated as [157, 158]: $\lambda_{GC} = 2\epsilon_0\epsilon_r RT/\sigma F$. Gouy-Chapman length, λ_{GC} is related to Bjerrum length, λ_B, as: $\lambda_{GC} = e/2\pi\sigma\lambda_B$, where λ_B ($=z^2e^2/4\pi k_B T$) provides us an estimation of electrostatic interaction between two particles in a solution [55]. The dimensionless number, C, indicates the ratio of the nanochannel height to a characteristic length scale associated with the influence of surface charge density on net

charge inside nanochannel.

Figure 3.5f illustrates the variation of average diffusioosmotic velocity in x-direction $< u_x >$ with the parameter C.

Below a critical value of $C \simeq 2.5$, the nanoflow is directed from the reservoir of high concentration (c_H) to that of low concentration (c_L). Above the value of $C \simeq 3.5$, the bulk nanoflow is in the opposite direction, from the low (c_L) to the high (c_H) concentration reservoir. In between these two critical values, circulation and mixing are present inside the nanochannel. These critical values of C were calculated based on the range of surface charge (σ) explored, between 0.001 and 0.05 C/m^2. These numerical values of critical C are very likely specific to the complex 2D nano/micro-junction geometry considered. Previous theoretical study of diffusioosmosis flow under a homogeneous concentration gradient along a charged flat plate shows that Zeta potential [45] or channel aspect ratio [138] plays an important role in the direction of the nanoflow. For our complex flow geometry of nano/micro-junction, we found that C is a better parameter delineating different flow regimes.

The non-dimensional number, C, can be physically interpreted through the interaction between electroosmotic and chemiosmotic flows, which is briefly explained below, and in details in the supplementary document. electroosmotic velocity, u_{EO}, is caused by electromigration of ions due to an external electric field or an induced one (due to interaction between surface charge and ions via a concentration gradient). Under the effect of a tangential electric field, E_x, it can be shown that u_{EO} for a charged nano-confinement of constant zeta potential, ζ, along its surface, is represented as [24, 48, 34]:

$$u_{EO} = -\frac{\epsilon \zeta E_x}{\mu} \tag{3.7}$$

where ϵ ($= \epsilon_0 \epsilon_r$) is the permittivity of the medium, and μ is the fluid viscosity coefficient. Using the boundary condition of constant surface charge density [65] $\left(\vec{\nabla}\phi \cdot \vec{n} = -\sigma/\epsilon\right)$, for an estimation of the electric field, $\vec{E}$ ($= -\vec{\nabla}\phi$), and neglecting the y-component of electric field compared to the x-component), Eq. (3.7) can be approximated as:

$$u_{EO} \simeq -\frac{\zeta \sigma}{\mu}. \tag{3.8}$$

When a nanochannel is subjected to a solution concentration difference, Δc, along its length, a chemical potential gradient develops and initiates fluid flow from one reservoir to another. This flow, known as chemiosmotic velocity, u_{CO}, can be expressed as [48, 49]:

$$u_{CO} = -\frac{k_B T}{\mu} \frac{\ln(1-\gamma^2)}{2\pi\lambda_B} \frac{\Delta c}{l c_0}. \tag{3.9}$$

Here $\gamma = \tanh(ez\phi_s/4k_BT)$: ϕ_s is the surface potential, z is the valence of ions, e is the electronic charge, k_B is the Boltzmann constant and T is the temperature. c_0 is the reference solution concentration, λ_B is known as the Bjerrum length and is related to Gouy-Chapman length, λ_{GC} $\left(= \frac{2\epsilon RT}{\sigma F} = \frac{2\epsilon k_B T}{\sigma e}\right)$, as [55]: $\lambda_{GC} = \frac{e}{2\pi\lambda_B \sigma}$. After considerable simplification (such as linearized Boltzmann distribution of ions [153]) described in details in the supplementary document, we obtained the ratio of chemiosmotic velocity (Eq. (3.9)) and electroosmotic velocity (Eq. (3.8)) to identify the effect of dimensions on electroosmosis and chemiosmosis:

$$\left|\frac{u_{CO}}{u_{EO}}\right| \approx \left(\frac{ez\phi_s}{8k_BT}\right)^2 \frac{\lambda_{GC}}{l} \exp\left(-\frac{y}{\lambda_D}\right). \tag{3.10}$$

Potential gradient along the charged surface can be estimated as $\vec{\nabla}\phi \cdot \vec{n} = d\phi/dy \simeq \phi_s/h$. Surface potential can, thus, be approximated as $\phi_s \simeq -\frac{\sigma h}{\epsilon}$. We substitute this expression for ϕ_s into Eq. (3.10) and obtain:

$$\left|\frac{u_{CO}}{u_{EO}}\right| \approx \frac{1}{8}\frac{h^2}{\lambda_{GC} l} \exp\left(-\frac{y}{\lambda_D}\right) = \frac{1}{8} C^2 \exp\left(-y/\lambda_D\right). \tag{3.11}$$

where C $(= h/\sqrt{l\lambda_{GC}})$ is the non-dimensional number characterizing the direction of nanofluidic transport inside the nanochannel. For $y << \lambda_D$, we can assume $\exp(-y/\lambda_D) \sim 1$, and thus, $|\frac{u_{CO}}{u_{EO}}| \sim \frac{C^2}{8}$. This allows us to express the critical C, C^* to be equal to $2\sqrt{2}$ when $u_{CO} \approx u_{EO}$. In other words, the number, C, can characterize the dominance of either chemiosmotic $(C > C^*)$ or electroosmotic$(C < C^*)$ flow. More details of the analytical formulation of C is provided in Appendix A. In our numerical analysis, we proposed a critical C between 2.5 – 3.5, which agrees well with the analytical prediction.

Based on charge conservation described by Eq. (3.2), diffusioosmotic flow is governed by diffusion, electromigration, and advection. When the nanochannel is narrow and long with sufficiently large Gouy-Chapman length, i.e., equivalent to a smaller value of C, the

electromigration term dominates, and due to charge selectivity of the nanochannel, anionic flow is dominant in the nanochannel and supplied by the solution flowing from the high to the low concentration reservoir (fig. 3.5b). Conversely, for wider and shorter channels of a relatively small Gouy-Chapman length (i.e., a large C), electroosmotic effect diminishes due to almost neutral electric field induced in the bulk. Consequently, the chemiosmotic effect dominates, with water molecules moving from low to high ion concentration area (fig. 3.5c). However, very close to the channel, the electromigration of ions is still dominant within the EDL and resulting electric field. In intermediate scenarios, neither of these effects dominates and a combination of these effects causes circulation and mixing in the nanoflow (fig. 3.5d).

3.5 Conclusion

We investigated the effects of the nanochannel dimensions and surface charge on diffusioosmotic flow in a charged nanochannel connecting two reservoirs of different electrolyte concentrations, which is a common flow geometry for reverse electrodialysis and micro/nanojunctions. In the parameter ranges explored, we empirically quantified a critical non-dimensional number $C = h/\sqrt{\lambda_{GC} l}$ which can essentially predict the direction of the nanoflow, thereby affecting the convective electrical flux in the nanochannel. Essentially, the dimensionless constant C describes a ratio of height to surface charge effect, where $\sqrt{\lambda_{GC} l}$ may indicate a length-scale, characterizing the effect of surface charge along the nanochannel length. A high value of C ($\gtrsim$3.5) indicates an insignificant electroosmosis, and due to chemiosmosis water flows in the same direction as the concentration gradient (from low to high concentration reservoir) for a positively charged nanochannel. In contrast, for a lower value of C ($\lesssim 2.5$) electroosmosis directs nano-DOF from the high to low concentration reservoir (against the concentration gradient) due to local electrical body force in the nanochannel. The nanoflow speed is, however, independent of this non-dimensional number, C, but linearly depends on the concentration difference. In terms of applications, the quantification of the nanoflow direction is important for building nanofluidic devices enabling flow control, currently attracting attention towards nanofluidic desalination and water purification. Our simulation results re-

veal the key quantitative parameter, C, for controlling nanoflow by tuning the nanochannel parameters of length, height, and surface charge.

Chapter 4

Diffusioosmotic flow in conical nanopores

4.1 Introduction

Flow through miniature geometries of the order of nanometers, referred to as nanofluidics, is dominated by several key surface effects, such as electrostatic interactions, surface tension, and capillary force [120, 111]. Exploiting these profound surface interactions, various fascinating micro/nano-fluidic observations, for instance, capillary condensation [159], charge selectivity [34] and DNA deformation [160], have been reported with significant applications in water purification [123, 124], renewable energy [67, 128], and biosensing [161, 162, 163].

An intriguing electrokinetic phenomenon in nano-confinement is the motion of electrolyte along a charged surface owing to an ionic concentration gradient. This phenomenon, widely known as diffusioosmosis, has been studied extensively in straight 1D nanochannels for symmetric electrolytes [142, 136, 137, 143, 45, 144, 145, 164, 165, 46]. A closed-form expression of one-dimensional diffusioosmotic velocity was reported by Keh et al., demonstrating its monotonic increase with increasing zeta potential [136], and non-linearly increase with decreasing porosity [137, 45]. Gupta et al. recently formulated a general one-dimensional analysis of diffusioosmotic velocity inside nanopores for axisymmetric electrolytes [46]. These insight-

ful mathematical formulations were performed with 1-D Poisson-Boltzmann linearization of ion distribution, and consideration of thin electric double layer. However, finite length of nanopores in nano/micro-junctions causes such configurations to be either quasi-2D or 3D in nature [152, 150, 151, 102]. In this regard, numerical investigations of DOF was conducted with 2D configuration for straight nano-confinements [148, 149, 138]. These 2D studies reveal an increase of diffusioosmosis flow (DOF) with increasing surface charge density [148] or increasing nanochannel aspect ratio [138], but report a nonlinear dependence of DOF on electrolyte concentration [148, 149]. Researchers also reported the reversal of DOF direction at a small zeta potential of planar charged nanochannel [136, 45], at a low electrolyte concentration [148], by tuning of width-to-height ratio [138], or through specific combinations of nanochannel parameters (of h, l, and σ) [166].

Diffusioosmosis has been utilized for a number of engineering applications, for instance, the manipulation of micro-particles using ultraviolet lasers [167], particle motion in dead-end pores [168, 169], and zeta potential measurement [170, 171]. In particular, electrokinetic flow in nanochannels of various geometries, such as, conical, hourglass, has been reported to demonstrate a nonlinear electrical response with low-current (high-resistance) ionic flow for a certain voltage bias, whereas a high-current (low-resistance) ionic flow when the voltage bias is reversed, which is commonly referred to as ion current rectification (ICR) [172]. Due to its unique ability to promote or restrict ionic current depending on the applied voltage bias, ICR is useful and significant in several biochemical applications, such as chemical separation [173] and biomimicry [174], which in turn has promoted detailed investigations of ICR [175].

ICR in tapered nano-sized compartments has been reported to vary with EDL and tip size [176], surface charge [177], electrolyte concentration [178], and the type of electrolyte [179]. Inversion of ICR has also been reported due to concentration depletion at the tip [157] and at the over-limiting current threshold [7]. Research on the numerical front focused on the influence of various control parameters on ICR, for instance, the effect of nanopore tip dimension [180], non-uniform surface charge density [181, 182], pore length [183], solution pH [184, 185]. Concerning the tapered nanofluidics, on the one hand, numerical simulations performed by neglecting the flow field have reported surface charge density, salt concentration

gradient, and nanopore geometry as the primary factors affecting ICR in tapered nanopores. [175, 7]. On the other hand, researchers have demonstrated the importance of electroosmotic flow in conical nanochannels by reporting significantly different ICR characteristics for systems with and without the consideration of nanoflow [186, 187]. These results hence, strongly imply the importance of the flow field for a more systematic and complete analysis in the model.

In spite of many analyses of ICR in nano-sized compartments, less attention has been given towards the detailed analysis and mechanism of the flow field through a charged, tapered nanochannel. Investigating such diffusioosmotic flow (DOF) in tapered pores can be instrumental in our understanding of selective ionic transport in biological systems [188]. In this article, we will focus on the analysis of the diffusioosmotic flow field in a tapered nanochannel under a variety of operating conditions. Through our two-dimensional numerical analysis, we aim to report the effect of critical parameters, such as cone angle, nanochannel tip diameter and length, as well as concentration difference on DOF velocity through a charged, tapered nanochannel.

4.2 Numerical model

Fig. 4.1a illustrates a schematic of our computational domain. In the model, two reservoirs are connected with a tapered nanochannel of uniform surface charge. Two solutions of different salt concentrations flow through the reservoirs (c_H and c_L in the left and right reservoir, respectively), generating a concentration gradient across the nanochannel. The positively-charged nanochannel repels cations and thus demonstrates charge selectivity, with an anion-exchange behavior. Due to the interaction between the nanochannel surface charge and ions in the electrolyte, an electric double layer (EDL) forms along the channel, which can be represented by the Debye length, λ_D; for symmetric ($z_+ = -z_- = z$) monovalent ($z = 1$) electrolyte: $\lambda_D = \sqrt{\epsilon_0 \epsilon_r RT/2F^2 c_0}$, where c_0 is the molar concentration of the electrolyte solution [153]. Due to the taper geometry of the nanochannel, the fraction of overlapping of EDL (i.e., λ/h) will not occur uniformly throughout the length of the nanochannel. Consequently, variations in the local electric field along the nanochannel would be observed. Besides, the angle

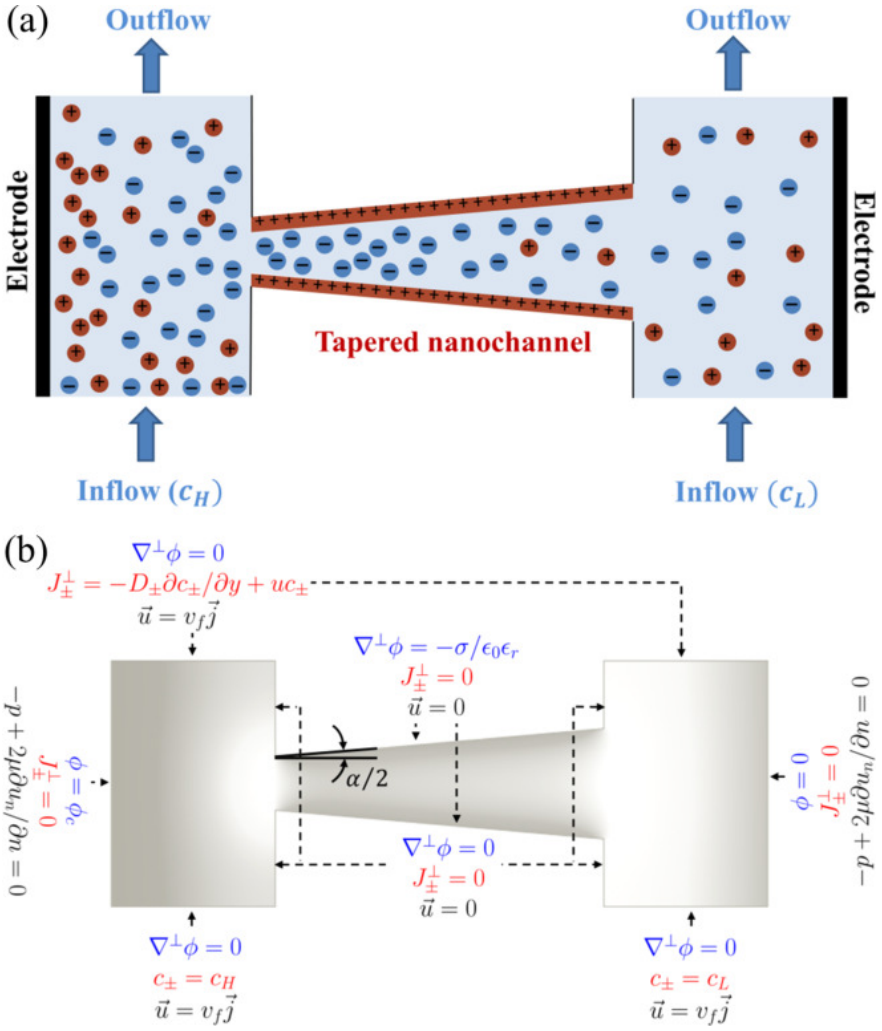

Figure 4.1: (a) Schematic of a positively-charged conical (diverging) nanochannel, connecting two reservoirs through which electrolytes flow at a specific velocity. A solution at high concentration (c_H) flows through the left-hand reservoir, while a dilute solution (c_L) flows through the right-hand reservoir. The corresponding boundary conditions used in the numerical model are shown in (b).

of the tapered nanochannel, α (also known as the cone angle), is expected to influence the ion concentrations and, hence, concentration gradient along the nanochannel. Therefore, here we investigate the significant effect of α on the diffusioosmotic flow field through the nanochannel. In addition, we report the dependence of diffusioosmosis flow velocity on nanochannel length, tip diameter, concentration difference (0–1 mM), and flow rate (over five orders of magnitude). With appropriate adoptions, the present numerical model can be designed to investigate the fields of flow, ionic concentrations, and electrical potential in a micro/nano-junction, where the reservoirs can be considered to be a part of the microchannels.

4.2.1 The governing equations

Nanofluidic transport of ions through nano-confinements involves the coupled interactions of ions and solvent due to surface charge and local electric field, and is dictated by the conservation of mass, momentum, charge, and ionic species. Firstly, the Poisson's equation correlates the distribution of electric potential, ϕ, with the spatial distribution of net charge, q, due to net ionic concentrations (c_i) [65, 154]:

$$\epsilon_0 \epsilon_r \nabla^2 \phi = -q = -F \sum_i z_i c_i, \tag{4.1}$$

where ϵ_0 (= 8.85×10^{-12} Fm $^{-1}$), ϵ_r (= 80.1), and F (= 96,485 Cmol^{-1}) are the permittivity of vacuum, relative permittivity of water, and Faraday's number, respectively. c_i and z_i represent the ionic concentration and valence, where the subscript, i denotes the cation (+), or the anion (−), respectively.

Secondly, the concentration of ions, c_i (for both c_+ and c_-), is modelled by the steady-state Nernst-Planck equation [65]:

$$\vec{\nabla} \cdot \left(-D_i \vec{\nabla} c_i - \frac{z_i D_i F c_i}{RT} \vec{\nabla} \phi \right) + \mathbf{u} \cdot \vec{\nabla} c_i = 0, \tag{4.2}$$

Here, D_i is the diffusivity of the respective ion, denoted by i (=+, −), $\mathbf{u}$ is the flow velocity vector, R (= 8.314 J K^{-1} mol^{-1}) is the universal gas constant, and T (= 293 K) is the temperature of the solution. In the present study, KCl is used as the dissolved salt, with $D_+ = D_{K^+} = 1.96 \times 10^{-9}$ m^2/s and $D_- = D_{Cl^-} = 2.0 \times 10^{-9}$ m^2/s, such that $D_+ \approx D_-$. The three terms

in Eq. (4.2) represent the contributions to the ionic flux by diffusion, electromigration, and convection, respectively. Similarly, the cationic ($\vec{J}_+$) and anionic ($\vec{J}_-$) ion-fluxes consist of the diffusive, electromigration, and convective contributions and can be obtained by integrating Eq. (4.2) [65]:

$$\mathbf{J_i} = \left(-D_i \vec{\nabla} c_i - \frac{z_i D_i F c_i}{RT} \vec{\nabla}\phi\right) + \mathbf{u} c_i. \tag{4.3}$$

The current across the nanochannel cross-section, I, can be calculated from the integration of ionic fluxes using Eq. (4.3):

$$I = \int F \sum_i (z_i \mathbf{J_i})\ dA. \tag{4.4}$$

Last but the least, the steady-state Navier-Stokes equation is implemented for the investigation of velocity profile inside the nano-confinement [156]. For the present nanofluidic system, the Reynolds number, Re ($= v_f l/\nu$, where the nanochannel length, l ~100 nm, inflow velocity, $v_f \approx 10^{-6} - 10^{-2}$ m/s, and kinematic viscosity of water, $\nu \sim 10^{-6}$ m^2/s) varies within the range between 10^{-7} and 10^{-3}. Due to such a small Re, we can neglect the contribution of the inertial terms. The velocity distribution in our geometry can, thus, be simulated using the Stokes equation, along with the Continuity equation:

$$-\vec{\nabla} p + \mu \nabla^2 \mathbf{u} + -q\vec{\nabla}\phi = 0; \tag{4.5}$$

$$\nabla \cdot \mathbf{u} = 0, \tag{4.6}$$

where p is the pressure.

4.2.2 Boundary conditions

The boundary conditions for the governing equations are represented in Fig. 4.1b. The walls of the tapered nanochannels were considered to be positively-charged, with no-slip and no-penetration of fluids and ions, i.e., $\vec{u} = 0$ along the nanochannel surface. The positive surface charge was numerically implemented by assuming the surface charge density, σ, to be constant along the nanochannel, and can be modeled by the following equation [154]:

$$\nabla^{\perp}\phi = -\frac{\sigma}{\epsilon_0 \epsilon_r}, \tag{4.7}$$

where $\nabla^{\perp}$ symbolizes a gradient operator in the direction perpendicular to the tapered nanochannel. We investigate a steady-state flow problem by using constant and equal inflow and outflow velocities in the reservoirs. An influx of ions into the reservoirs occurred at specific concentrations, i.e., at high concentration, c_H (saline water) and low concentration, c_L (freshwater) through the left and right reservoirs, respectively. There was no external pressure difference across the nanofluidic setup. For the investigation of diffusioosmosis without any external electric field, we did not apply any external electrical potential difference in our model (i.e., we considered $\phi_c = 0$, where ϕ_c is the electrode potential in the left-hand side).

4.2.3 Validation

Motivated by nanofiltration technologies,Balannec et al. investigated pressure-driven nanofluidic transport across conical and hourglass-shaped nanopores [6], reporting significant ICR due to co-ion exclusion at the pore tip, and varying electric field along the pore. We validated our numerical model with this numerical investigation of conical nanopores [6], as shown in Fig. 4.2. Our results of the average concentration of anions demonstrated a reasonable agreement with those reported by Balannec et al. [6]. These consistent results of insignificant c_- values also illustrate the charge selectivity of the positively-charged nanochannel.

Shown in Fig. 4.3 is further validation of our model performed with the results of ICR for different voltage bias, reported by Rosentsvit et al. [7]. The numerical simulations were conducted for the negative and positive voltage bias of the same magnitude, and the ICR factor was determined with the ratio of the corresponding current obtained via Eq. (4.4) [7]:

$$\mathrm{ICR} = \frac{|I_{V_0<0}|}{|I_{V_0>0}|}, \tag{4.8}$$

where $I_{V_0<0}$ and $I_{V_0>0}$ are the currents obtained for a negative and positive voltage bias (of the same magnitude), respectively. Overall, in spite of the complexity of the simulations and geometries, consistent values and trends of the ICR variation with voltage are obtained by our model, with our results deviating by 11.6 % from those by Rosentsvit et al. [7]

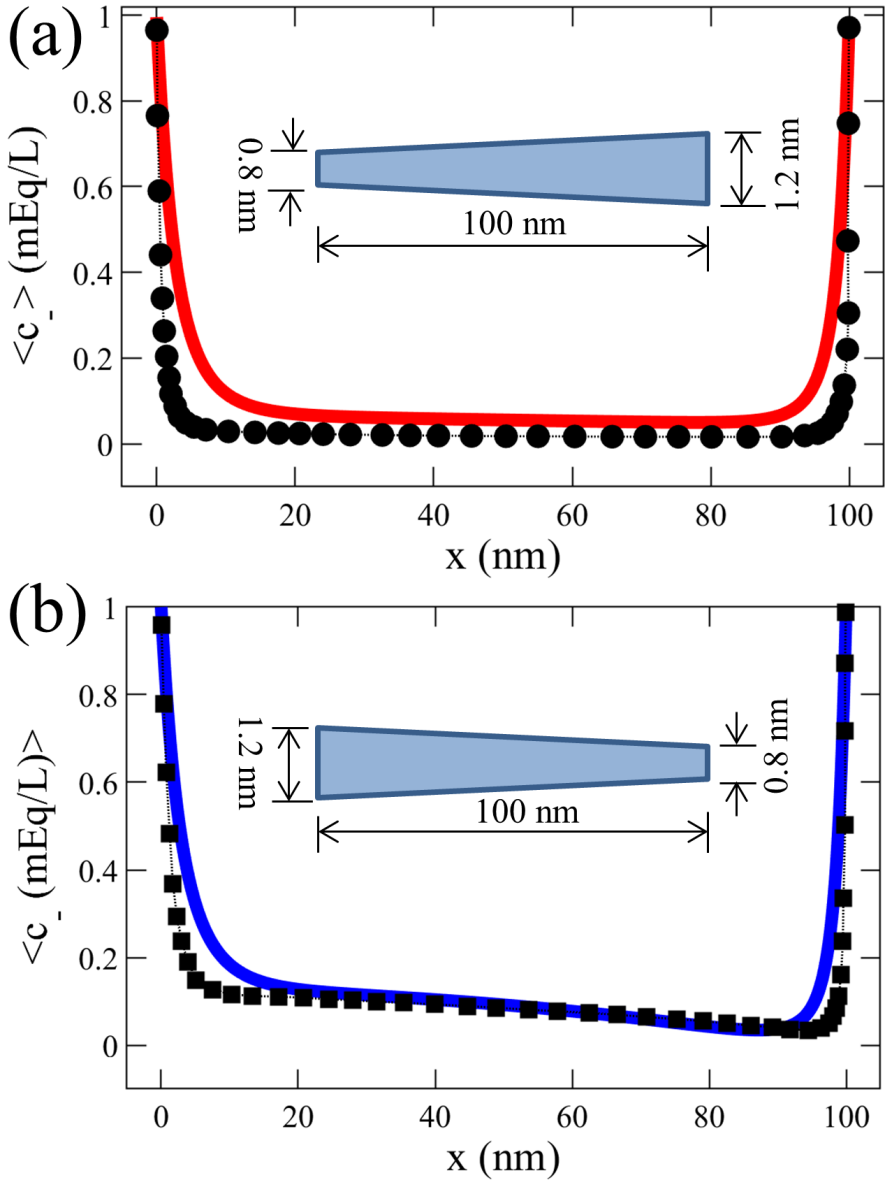

Figure 4.2: Validation of our numerical model of a tapered nanochannel by comparing the average anion concentration profiles ($c_{\pm}$) reported by Balannec et al. investigating pressure-driven ion transport through conical nanopores [6]. The geometries of the nanopores simulated are shown in the figure (not to scale), and the simulations were performed at constant surface charge density, σ =-1 mC/m^2, and a solution concentration of 1 mEq/L, as used by Balannec et al. The results from Balannec et al. for divergent and convergent nanopores are represented by ● in (a) and ■ in (b), respectively. Our corresponding results are shown by — in (a) and — in (b).

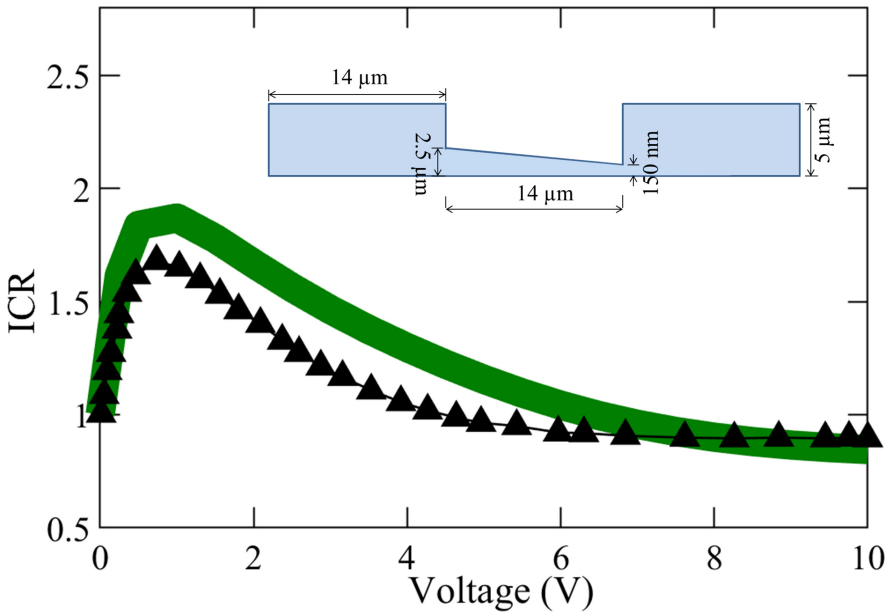

Figure 4.3: Comparison of ICR factor from our numerical model (—) with the that from the investigation of ICR inversion effects by Rosentsvit et al. (▲) for divergent nanopores [7]. The figure inset shows the geometry (not to scale) of the axisymmetric model simulated. Following the parameters used by Rosentsvit et al., we assumed σ =-0.06 C/m^2 and c_0 = 1 μm for this comparison.

4.2.4 Mesh independence analysis

To perform a grid independence study, we used the same geometry as Rosentsvit et al. [7], which is described in the previous section. While keeping σ =-0.06 C/m^2 and c_0 = 1μm constant, we changed the mesh size in increasing steps to identify the optimal grid spacing (which did not alter the simulation output). The results of the mesh independence analysis are illustrated in Fig. 4.4, with the total number of elements ranging from 294 to 246,426. Approximately with a mesh number greater than 10,000, no significant deviation of results was observed. Hence, all further numerical simulations were carried out with the total number of elements exceeding 10,000.

4.3 Results

Diffusioosmosis primarily comprises of two essential components, namely chemioosmosis and electroosmosis. Chemioosmosis is caused due to the concentration gradient inside the nanochan-

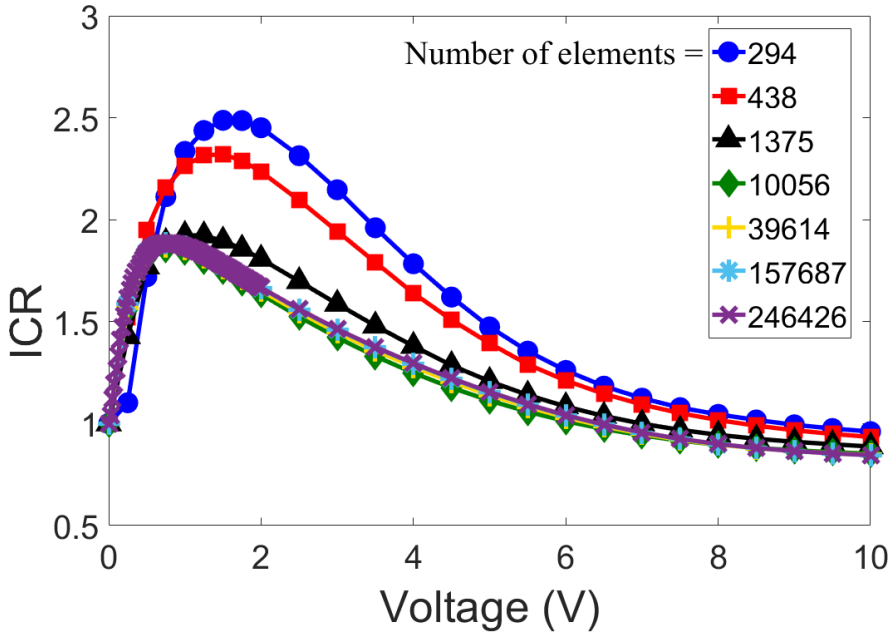

Figure 4.4: Grid independence study of our numerical model, based on the ICR factor for σ = -0.06 C/m^2 and c_0 = 1μm. The corresponding dimensions and model geometry are shown in the inset of Fig. 4.3.

nel, whereas electroosmosis occurs as a result of the induced local electric field due to the EDL and surface charge. In this particular case of a tapered geometry, besides these two effects, the cross-section changes along the channel length, which based on the mass conservation can either accelerate or decelerate the overall flow for a convergent or divergent nanochannel, respectively. A complex interplay between these effects contribute to the resultant diffusioosmosis flow through a tapered, charged nanochannel. The geometric parameters in our model are kept more than 5 nm for all our cases, in accordance with the acceptable results for continuum modeling in nanofluidics. [111]

4.3.1 Impact of cone angle

We investigate the effect of cone angle (α) on diffusioosmotic flow velocity, with a constant tip diameter (d_t), nanochannel length (l), concentration difference (Δc), and solution inflow velocity (v_f). To observe the behavior of both converging and diverging channels, we vary α in the range of ±20°, while keeping d_t, l, c_H, c_L and v_f fixed at 20 nm, 100 nm, 0.15 mM, 0.01 mM,

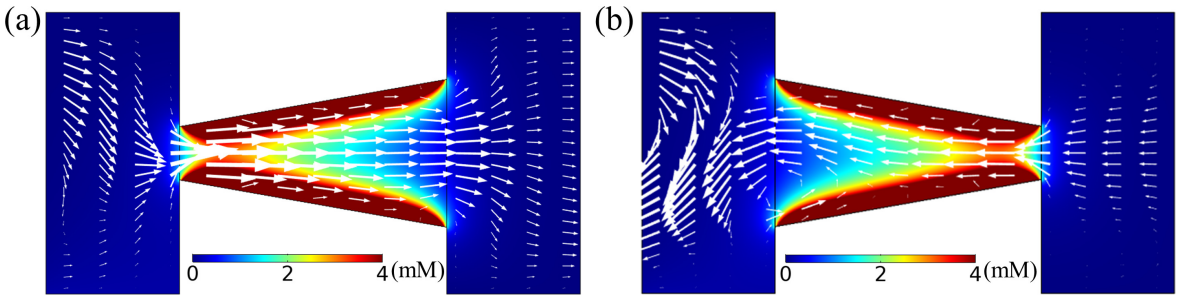

Figure 4.5: Anion concentration distribution (color map) and diffusioosmotic velocity profile (in arrows), for a nanochannel of length l = 100nm and tip diameter d_t = 20 nm, for a tapered geometry of tilt angle α = 15° (diverging) in (a), and α = -15° (converging) in (b). Here, v_f=7 μm/s and Δc= 0.14 mM.

and 7 μm/s, respectively. Typical flow fields for α = +15° (diverging) and -15° (converging) tapered nanochannels are illustrated in Fig. 4.5. Flow, in both cases, is directed from the edge with the smaller orifice to the wider one. Due to the effect of (positive) surface charge along the nanochannel wall, the anion concentration is higher inside the nanochannel compared to those of the two reservoir flows of the dilute and concentrated electrolyte solutions. There is a greater EDL overlapping adjacent to the smaller orifice due to the narrower gap between the charged walls. As evident from Fig. 4.5, the concentration of anions near the smaller orifice is greater than that close to the wider orifice. Therefore, a stronger concentration gradient locally develops near the smaller orifice, which results in a more dominant chemiosmotic flow (of water movement) from the nearby reservoir towards the smaller nanochannel orifice. Conversely, adjacent to the wider orifice, the concentration gradient is not as strong as that in the smaller orifice. Hence, due to a smaller driving force, this flow is overtaken by the stronger chemiosmotic flow from the smaller orifice towards the wider gap.

To investigate the contribution of the electroosmotic component in these two flow scenarios, we observed the distribution of electric potential, ϕ, and electric field, $\mathbf{E}$ = -$\vec{\nabla}\phi$ of our simulations (with their corresponding figures given in section 5.5. In both the diverging and converging nanochannels, the average electric potential at the small and large orifices was comparable, resulting in a similar electroosmotic effect. The electric field directed away from the nanochannel near the orifices for both diverging and converging nanochannels. Here, we noticed the maximum electric field near the center of the nanochannel, instead of close to the

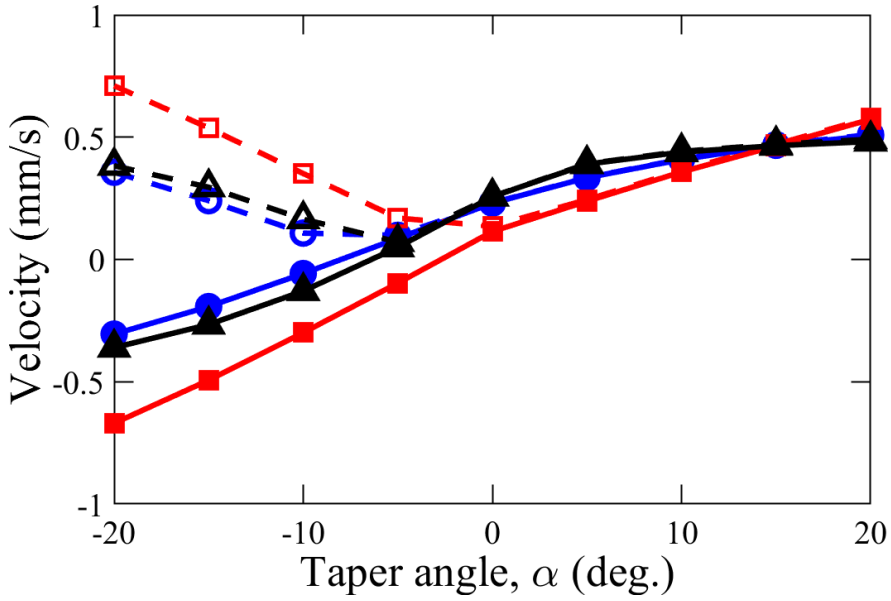

Figure 4.6: Variation of average velocity in x-direction (solid line) and velocity magnitude (dashed line) with angle of taper, α, in a nanochannel of various length l and tip diameter d_t: (i) l = 100 nm and d_t=20 nm (●), (ii) l = 100, d_t = 40 nm (■), and (iii) l = 200, d_t = 20 nm (▲). Other control parameters were kept constant: Δc=0.14 mM, v_f=7 μm/s, and σ=0.01 C/m^2.

nanochannel tip. This is probably due to the overlapping of EDL near the nanochannel narrow tip, leading to a reduction of the electric potential gradient and, hence, the electric field. Thus, in these cases of investigations, the electroosmotic effect was found to be negligible when compared to its chemiosmotic counterpart.

A comparison of the diffusioosmotic flow (DOF) velocity for various taper angles, α, is shown in Fig. 4.6 for three different scenarios of l and d_t. Since there is stronger DoF flow adjacent to the smaller orifice of the tapered nanochannel, the overall DOF direction is in the direction of increasing nanochannel height or gap-thickness, h (i.e., from high to low concentration reservoir) for a positive angle of taper ($\alpha > 0$). Similarly, when α is negative, DOF occurs also in the direction of increasing nanochannel height, h (while, in this case, directed from the low to the high concentration one). This preferable flow direction reveals that the cone angle (α) plays a vital role in the direction of DOF. In addition, the DOF flow velocity increases with an increase in the magnitude of the cone angle.

The effect of the cone angle was also investigated for different tip diameters, d_t, and

nanochannel length, l. Keeping nanochannel length fixed ($l = 100$ nm), when the tip diameter, d_t is changed from 20 nm to 40 nm, weaker DOF is observed when α<15°. Moreover, in this case of d_t = 40 nm, the change of DOF velocity with a taper angle was approximately linear (when compared to the other cases studied). This observation can be attributed to a substantial EDL overlap in d_t = 20 nm, which causes a higher chemiosmotic transport, whereas a much weaker or nearly no-overlap of EDL in case of d_t = 40 nm. Therefore, according to the mass conservation, for a higher nanochannel d_t without overlapping of EDL, the diffusioosmotic velocity in the '2D' geometry changes inversely linear with the change in flow cross-sectional area ($A = d_t * w$, where w is the thickness of the nanochannel, and can be assumed to be of unity for the 2D geometry). Keeping d_t = 20 nm, when l was changed from 100 nm to 200 nm, an insignificant variation in the DOF results were observed.

4.3.2 Effect of tip diameter and nanochannel length

To carefully analyze the effect of nanochannel length, l, and tip diameter, t_p, we analyzed the x-directional velocity profile inside the nanochannel, illustrated by Fig. 4.7. To facilitate better visualization, we non-dimensionalized the x-coordinate along the nanochannel with the nanochannel length, l, with the zero (reference point) in the normalized x-coordinate representing the left-hand side edge of the tapered nanochannel. Under constant cone angle, nanochannel length, concentration difference, and inflow velocity, we observed the effect of varying d_t on DOF in the range of $10 - 50$ nm, as shown in Fig. 4.7a. In all the simulations, we observed the maximum flow velocity at the narrowest orifice of the nanochannel. This observation is consistent with the mass conservation principle because the flow rate remains constant throughout the nanochannel and, hence, the maximum velocity would occur near the minimum flow cross-section area.

Theoretically, DOF velocity decreases with the increase of the diameter along the tapered nanochannel. Even though the taper angle and nanochannel length are the same for all the simulations, we observe that a decreasing in velocity with increasing channel height is more rapid for smaller tip diameter. With α and l kept constant for all the simulations in Fig. 4.7a, we observe that the diffusioosmotic velocity decreases as the gap-diameter increases, with the

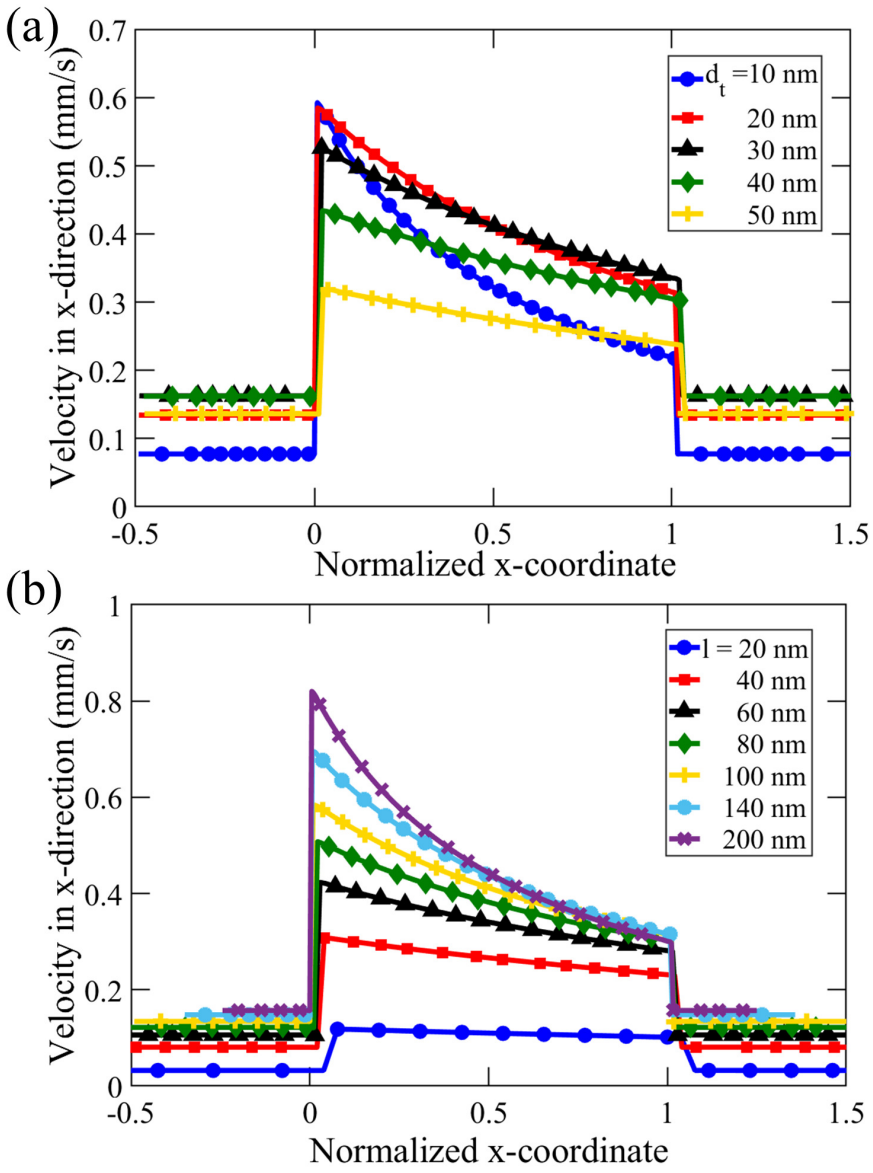

Figure 4.7: Average velocity in x-direction along a nanochannel of constant cone angle, $\alpha = 10°$, inflow velocity, $v_f = 7$ μm/s, and concentration difference, $\Delta c = 0.14$ mM to study the effect of (a) nanochannel tip diameter, d_t, in the range $10 - 50$ nm, with l=100 nm, and (b) nanochannel length, l, in the range $20 - 200$ nm, with $d_t = 20$ nm. The x-coordinate is normalized with the nanochannel length, l.

maximum value at the (narrow) tip and the minimum amount at the (broad) base of the tapered nanochannel. This decrease in DOF is more rapid for nanochannels with a smaller d_t. For instance, in case of d_t = 10 nm, the flow velocity near the base (v_b) is about half of that at the tip (v_t), i.e., $v_t/v_b \approx 2$, which is consistent with the corresponding (cross-sectional) area ratio $A_t/A_b = d_t/d_b \approx 1.88$). Meanwhile, for d_t = 50 nm, average DOF velocity is comparable at the tip and the base; in this case, $v_t/v_b \approx 1.2$ is consistent with the ratio of cross-sectional area, $A_t/A_b \approx 1.35$. This shows that the effect of the tip diameter is enhanced for smaller d_t-values, when the EDL overlap is more pronounced, which in turn causes a stronger concentration gradient.

In addition, DOF decreases non-linearly for smaller d_t (10 – 20 nm). The overlapping of EDL can cause higher concentration in the nanochannel, and, hence, results in a higher concentration difference when compared to the electrolyte concentration in the reservoir. This results in a stronger chemiosmotic effect, contributing to an overall higher diffusioosmotic flow for smaller d_t. However, in the case of larger d_t (30 – 50 nm), there is much lesser EDL overlap near the smaller orifice (See SI for quantitative analysis). The above effect of higher DOF due to EDL overlap was not observed in such channels with wider tips. Flow velocity in nanochannels with larger d_t, thus, shows an approximately linear decrease from the tip to the base along the length of the nanochannel due to dilation of the 2D cross-sectional area, which is proportional to the gap thickness. For further illustration, we looked at the simulations results shown in Fig. 7a, and found that a tapered nanochannel with d_t = 50 nm has a much smaller average anion concentration ($\langle c_- \rangle$) of 0.65 mM at the tip, when compared to that of a nanochannel with d_t = 20 nm ($\langle c_- \rangle$ =1.33 mM). As a result, the corresponding diffusioosmotic velocity near the nanochannel tip is u = 0.32 mm/s in case of d_t = 50 nm, which is much less than that for d_t = 20 nm (u = 0.58 mm/s).

To obtain a complete picture of the effect of dimensions for tapered nano-confinements, we vary the nanochannel length (l), while keeping the other parameters constant. Shown in Fig. 4.7b are the results of our investigation of variation of l in the range of 20 – 200 nm. The maximum speed increases with an increase in l, even when d_t remains constant. With a larger l, the total surface charge is higher, and thus, the overall effect on DOF is stronger via the

electroosmotic component of the DOF, which is manifested by a higher DOF velocity at the nanochannel tip. The minimum speed inside the nanochannel is of comparable magnitude for various nanochannel length for $l > 20$ nm. Fig. 4.7b further demonstrates that the decrease in velocity in terms of the normalized x-coordinate is higher for a larger l.

4.3.3 Influence of concentration difference

We investigated the effect of concentration difference on the DOF velocity in a tapered nanoduct, by varying the concentration c_H, while keeping c_L constant at 0.01 mM. The external concentration difference, Δc ($= c_H - c_L$) was varied from 0 to 1 mM while maintaining constant values of the other control parameters, as illustrated by Fig. 4.8. The diffusioosmotic velocity shows a nonlinear increase with an increase in Δc, for all the three simulated cases of different nanochannel dimensions. The increase of DOF with Δc can be fitted using a quadratic polynomial (i.e., $u_{DO} \approx a(\Delta c)^2 + b\Delta c + c$, where a, b and c are fitting resutls, which may be a function of nanochannel parameters). For example, in case of a tapered nanochannel of $d_t = 20$ nm, $l = 100$ nm, and $\alpha = 10°$, the fitting results show $a = 0.75$, $b = 1.7$, and $c = 0.17$. This quadratic relation observed is in contrast to the observations for straight, charged nanochannel, where a linear dependence of DOF velocity with Δc was reported [166].

The nonlinearity may arise due to the changing gap-thickness, which causes the fractional EDL overlapping (i.e., λ/h) along the nanochannel to vary. This partial overlap of EDL causes variation in local (anion) concentration along the channel, affecting the chemioosmotic flow along the channel. Further, the electric field, perturbed by the local variations in concentration influences the electroosmotic component. The complex interplay between chemioosmotic and electroosmotic flows depending on Δc, contributing to a nonlinear dependence of DOF velocity on Δc. When the tip diameter was increased from 20 nm to 40 nm, a significant reduction in DOF magnitude was observed. For instance, in case of $\Delta c = 1$ mM, average velocity inside the tapered nanochannel reduced from 1.15 mm/s for $d_t = 20$ nm to 0.75 mm/s for $d_t = 40$ nm. Moreover, the nonlinearity in Δc dependence also increases. These observations may be due to the fact that the nanochannel tip diameter, d_t, affects the overlap of EDL, and hence, the overall flow. On the other hand, an increase of nanochannel length from 100 nm to 200 nm,

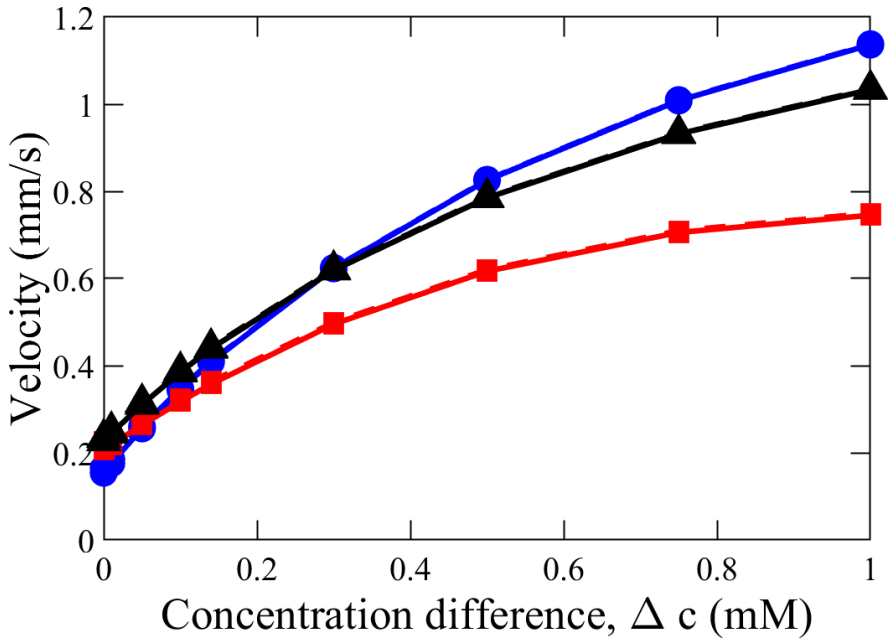

Figure 4.8: Variation of average velocity in x-direction (solid line) and velocity magnitude (dashed line) with concentration difference, Δc, in a nanochannel of (a) length, l=100nm and tip diameter, d_t=20 nm (●), (b) l=100, d_t=40 nm (■), and (c) l=200, d_t=20 nm (▲). Other control parameters were kept constant: α=10°, v_f=7 μm/s, and σ=0.01 C/m^2.

while keeping d_t constant at 20 nm, did not cause a noticeable variation in the DOF velocity for different Δc in the range of 0 – 1 mM.

Even when there was no concentration difference across the tapered nanochannel (i.e., Δc = 0), non-zero DOF was still observed inside the tapered nanochannel. This flow can probably be attributed to the taper in the nanochannel, resulting in local concentration differences along the channel due to partial EDL overlap. This local concentration difference and induced electric field drive localized chemiosmotic and electroosmotic effects in tapered nanochannels, causing an overall flow.

4.3.4 Effect of inflow rate

We studied the effect of inflow velocity, varying over five orders of magnitude in the range of 0.7 μm/s – 7 mm/s. The inflow velocity, v_f, was kept equal for both the left (high concentration, c_H) and right (low concentration, c_L) reservoirs. Revealed in Fig. 4.9 are our simulation results of the diffusioosmotic flow velocity for various v_f in a semi-logarithmic plot.

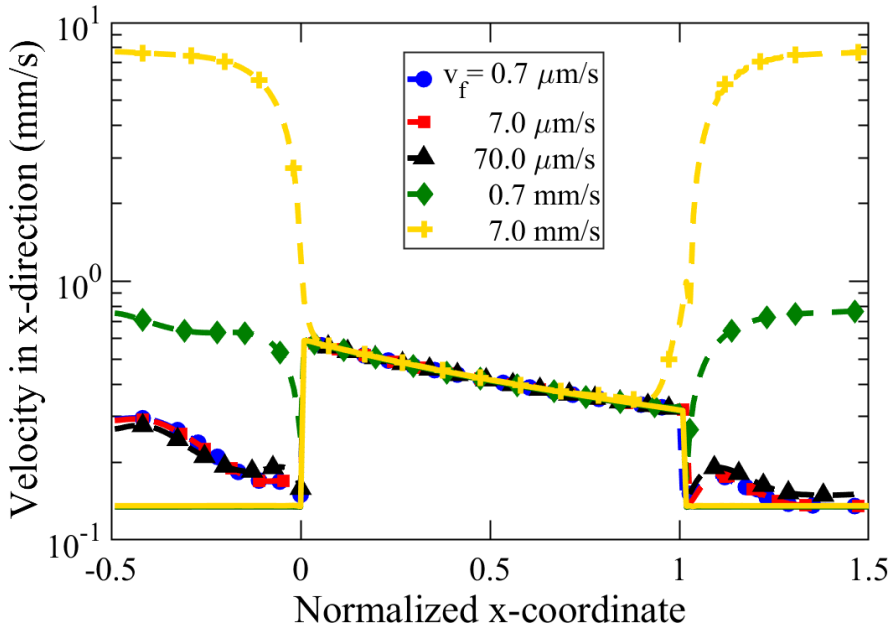

Figure 4.9: Average velocity in x-direction (solid lines) and velocity magnitude (dashed lines) along a nanochannel of length l = 100 nm, tip diameter, d_t = 20 nm, cone angle, α = 10°, and concentration difference, Δc = 0.14 mM. The x-coordinate has been normalized with the nanochannel length, l.

For the range of flow velocities analyzed, the inflow velocities did not alter the flow pattern inside the nanochannel. A higher inflow velocity (e.g., v_f= 7 mm/s) causes an increase in the y-component of DOF near the edges of the tapered nanochannel, illustrated in Fig. 4.9 by the high value of velocity magnitude. However, we observe the insignificant impact of the inflow rate on the DOF speed inside the tapered nanochannel, as the velocity in x-direction and velocity magnitude matched with each other. Hence, the flow inside the nanochannel is dominated by x-directional flow, with an insignificant y-directional velocity component. Such an observation is likely due to our investigation in the low Peclet number regime ($Pe = v_f h/D \lesssim 0.1$, where $v_f \leq 7$ mm/s, $h \leq 50$ nm, $D \simeq 2 \times 10^{-9}$m^2/s). Here, higher flow velocity was not investigated, since such high flow velocities are difficult to implement and are rarely reported for micro/nano-fluidic experiments. In case of very high inflow velocity (v_f = 7 mm/s) in Fig. 4.9, we observed that a large reservoir inflow velocity could influence the DOF near the edges of the tapered nanochannel, which is manifested in terms of high-velocity magnitude near the nanochannel orifices.

4.4 Conclusion

We present a two-dimensional numerical analysis of diffusioosmosis in nanochannels of tapered geometry to investigate the importance of various operating parameters, such as cone angle, nanochannel dimensions, and flow rate. In the low Peclet number regime ($Pe \lesssim 0.1$), an insignificant variation of DOF inside the nanochannel was observed when the external flow velocity of solutions through the reservoirs was varied over five orders of magnitude. The angle of taper was found to have a very prominent effect of the direction of diffusioosmotic velocity, where positive taper angle (i.e., diverging shape) facilitates flow in the direction towards increasing gap thickness (i.e., from high to low concentration reservoir in our setup). In contrast, a negative taper angle favors flow in the opposite direction from low to high concentration (but still in the direction towards increasing gap thickness). The primary reason for such an observation is likely due to the overlap of EDL at the narrower orifice, causing a higher concentration gradient, which in turn promotes greater chemiosmotic flow (from the nearby reservoir towards the smaller orifice via water transport). By the same token, a smaller tip diameter increases the DOF. Due to an influence of the surface charge on the ionic concentration distribution inside the nanochannel, a longer nanochannel length increases the flow velocity via higher net surface charge and, hence, electroosmotic effect. In contrast to previous analysis in a straight, charged nanochannels, reporting a linear dependence of DOF velocity on Δc [166], a nonlinear increase of DOF with an increase in concentration difference was observed, which can be described via an empirical relation of a second-order polynomial. The nonlinearity of this dependence increases when the tip diameter is smaller, whereas a change in channel length did not cause a significant impact on the overall DOF.

Chapter 5

Numerical simulation of renewable power generation using reverse electrodialysis [1]

5.1 Introduction

The quest for clean energy meeting the global needs has advanced extensive research and development in sustainable energy sources [189, 190, 191, 192], such as geothermal [190], solar [193, 194], wind [195], and hydroelectric [196, 197] energy. Another promising renewable source is salinity gradient energy (SGE), obtained from the thermodynamic free energy of mixing two electrolyte solutions of different concentrations [83, 198]. SGE can be harnessed primarily by two processes, namely pressure-retarded osmosis [199] and reverse electrodialysis (RED) [200, 67]. The latter, RED is an emerging and mainstream technology for harnessing such energy by preferential transfer of ions across ion-selective interfaces, such as nanoporous, ion-exchange membranes [198, 67, 80, 201] or charged nanochannels using micro- and nano-fluidics [98, 202, 203, 204]. In these two types of RED methods (using charged membranes or nanochannels), physically, due to the surface charge of nanopores via electrostatic interaction,

[1] Chanda & Tsai, Energy 176 (2019) 531–543.

counter-ions flow through the confinement whereas co-ions are repelled. The transportation of (attracting) counter-ions and (repelling) co-ions across the nanopore under an external chemical potential gradient can result in an ionic flow producing electrical energy [80]. It has been estimated that ideally the maximum SGE of $\approx$ 2.3 MJ could be captured when 1 m^3 of freshwater (from a river) is mixed with seawater [205]. Thus, with a global freshwater flow rate of $\approx 1.2 \times 10^6$ m^3/s [206], a power output $\approx$ 2.7 TW could be extracted. Therefore, large-scale RED technology could potentially provide adequate sustainable energy and, hence, is a vital topic.

Pattle first experimentally demonstrated the concept and feasibility of RED technology obtaining SGE power, by flowing freshwater (e.g., from a river) and salty-water through (acidic and basic) ion-exchange membranes [81]. Motivated by this exciting finding, theoretical studies were carried out to understand the mechanism of ion transport and electrical interactions of such RED cells [83, 207, 82, 208, 84, 85]. A theoretical capillary model (mimicking charged porous membrane) revealed a high efficiency of energy conversion for narrow confinements, with the assumption of 1D Debye-Hückel linearization considering large [83] and small [82] concentration differences. Recently, Vermaas et al. estimated a maximum power density of 2.7 W/m^2 with the present technological advances using a RED stack model, a phenomenological model analyzing various resistance components with the Nernst Equation. [84], and further demonstrated that a recirculation of the feed water could achieve an efficiency of more than 50% using co-, counter- and cross-flow methods [85, 209]. However, because of complex membrane geometry and pore-scales, most previous theoretical investigations on RED use assumptions or/and simplified geometry of a single nanopore.

Since Pattle [81], various laboratory experiments have been conducted to aim at better understanding and efficiency for RED operations using membranes [201, 205, 89, 88, 86, 87, 92, 91]. These investigations revealed the effects of different concentrations and flow velocities [86], an exponential decay of power output with time [87], a better energy output by lowering inter-membrane distance [88], and a strong influence of salinity gradient on membrane resistance [89]. To improve the RED efficiency, researchers have recently fabricated new membranes, used different flow conditions, and improved stack designs of RED cells for optimal power

generation [67, 80, 201, 92, 91, 90, 93].

Several numerical investigations of RED have been undertaken to gain the fundamental understanding of the RED process and corresponding efficient designs. Most of the numerical work focused on the analysis of a single nano-confinement (nanopore or nanochannel) for computational simplicity [4, 94, 5] since a full, accurate simulation considering nonlinear, coupled (flow and electrical) interactions within nanoporous membranes is challenging. A two-dimensional (2D) numerical simulation of RED concluded that power generation could be maximized by minimizing the cross-sectional area, increasing surface charge density, and optimizing the length of the charged nanochannel [4]. However, this model focused on ionic interactions without considering the fluid flow. The model was improved later by computing flow field using the Stokes flow model [5], revealing a decrease of electrical conductance with an increase in nanopore length. More recently, researchers have numerically studied RED process using a more complex geometry, for instance, pH-regulated conical nanopores [186], a cell pair with cation and anion exchange membranes [210], asymmetric bilayered nanopore [211], and nonuniform surface charge distribution [212]. However, these numerical studies did not investigate the effect of external flow through the reservoirs, as expected in a realistic RED cell with injections of salt solutions.

In the present work, we consider the addition of external flows through the reservoirs connecting a charged nanochannel. The simulations aim to develop a better understanding of the variation of energy conversion efficiency and power density under the influences of different concentrations of salt solutions, concentration gradient, nanochannel dimensions, and external flow. In particular, to the best knowledge of our, the effect of external flow on RED electrical outputs with a charged nanochannel has not been reported numerically.

5.2 Mathematical model

We numerically examine the flow, ion concentration, and electric potential fields in a steady-state reverse electrodialysis process using a single nanochannel to understand the effectiveness of a charged nanopore in harnessing SGE. Fig. 5.1a shows the schematic of the model, in

which a single nanochannel connects two reservoirs with a constant and positive surface charge density (σ). A salt solution of high concentration (c_H) flows through one reservoir (on the left), whereas a diluted one (c_L) through the other (on the right). We inject the electrolyte streams through the reservoir with the same velocity, $v_f\hat{j}$, and we do not apply any external pressure gradient to drive flow across the nanochannel between the two reservoirs. The flow is therefore primarily driven by the chemical potential due to salt concentration difference and electrical forcing inside the charged nanochannel.

The charged nanochannel with overlapping of Debye length can exhibit charge selectivity, allowing counter-ions to pass through while repelling the co-ions. This charge separation induces electrical field adjacent to the charged nanochannel, while a chemical potential gradient exists due to electrolyte concentration difference (i.e., $c_H - c_L$) between the reservoirs. The interplay between these driving forces and the charge selectivity of the nanochannel give rise to complex and nonlinear flow, ion-concentration profiles, and the resulting electrical current and outputs.

5.2.1 The governing equations

The governing equations are based on the conservation of mass, momentum, charge and ionic species [65]. The distribution of electric potential, ϕ, is governed by the Poisson's equation due to spatial net charges [154]:

$$\epsilon_0\epsilon_r\nabla^2\phi = -q = -F(z_+c_+ + z_-c_-), \tag{5.1}$$

where ϵ_0 ($= 8.854 \times 10^{-12}$ Fm $^{-1}$), ϵ_r ($= 80.1$), and F ($= 96{,}485$ Cmol^{-1}) are the permittivity of vacuum, relative permittivity of water, and Faraday's number, respectively. c_+ and z_+ are the concentration and valence of the cation, respectively, whereas c_- and z_- are their anionic counterparts.

Based on the continuity of electric current consisting of diffusive, electromigration, and convective fluxes, the concentration fields of ions (c_i, $i = +, -$ representing the cation and anion concentrations, respectively) in the solution are modelled by the Nernst-Planck equation in a

steady-state [65]:

$$-\vec{\nabla}\cdot\left(D_{\pm}\vec{\nabla}c_{\pm}+\frac{D_{\pm}}{RT}z_{\pm}Fc_{\pm}\vec{\nabla}\phi\right)+\vec{u}\cdot\vec{\nabla}c_{\pm}=0, \tag{5.2}$$

where T (= 293 K) is the operating temperature, R (= 8.314 $JK^{-1}mol^{-1}$) is the universal gas constant, and D_+ and D_- are the diffusivities of the cation and anion, respectively. Corresponding to the diffusivities of K^+ and Cl^- ions, D_+ and D_- are assumed to be 1.96×10^{-9} m^2/s and 2.0×10^{-9} m^2/s. Physically, the sequential terms in Eq. (5.2) describe diffusion, electromigration, and convection of ions, respectively [24, 65]. The competition among these factors dictates the ionic flux inside the nano-confinement.

Integrating Eq. (5.2), we can obtain the cationic ($\vec{J}_+$), and anionic ($\vec{J}_-$) flux, and is defined by the following equation, consisting of diffusive, electromigration, and convective ion-flux [65]:

$$\vec{J}_{\pm}=\left(-D_{\pm}\vec{\nabla}c_{\pm}-\frac{z_{\pm}D_iFc_{\pm}}{RT}\vec{\nabla}\phi\right)+\vec{u}c_{\pm}. \tag{5.3}$$

The ion concentrations in the solution (i.e., c_+ or c_- for the cation and anion, respectively) are governed by the conservation of ionic species and described by the Nernst-Planck equations. Considering a steady problem, these equation can be represented as [155, 65]:

The flow field is simulated by solving the steady-state Navier-Stokes equation, along with the continuity equation. Due to the miniature geometry used here, the dimensionless Reynolds number, defined by the ratio of inertia to viscous effect, $Re\equiv ul/\nu\approx10^{-5}-10^{-4}$, where u is typical nanoflow speed, l is nanochannel length, and ν is fluid kinetic viscosity. Hence, the contributions of the inertial terms can be neglected. We thus simulate a steady-state Stokes flow [156]:

$$\nabla\cdot\vec{u}=0, \tag{5.4}$$

$$-\vec{\nabla}p+\mu\nabla^2\vec{u}\underbrace{-F(z_+c_++z_-c_-)\vec{\nabla}\phi}_{\vec{F}_e=q\vec{E}=-q\vec{\nabla}\phi}=0, \tag{5.5}$$

where μ is the liquid viscosity (for water, $\mu \simeq 1$ mPa·s at room temperature), $\vec{F}_e$ is the electrical body force, and q ($= z_+c_+ + z_-c_-$) is the net charge. Eq. sets (5.1)–(5.5) are non-linearly coupled, and we numerically solve for velocity, $\vec{u}$, pressure, p, electrical potential, ϕ, and ion concentrations, $c_\pm$.

5.2.2 Boundary conditions

The boundary conditions (BCs) used for the governing Eq. (5.1)–(5.5) are listed in Fig. 5.1b. To solve for the electrical potential (ϕ), we first assumed constant surface charge density, σ, along the charged nanochannel wall. σ is described by the discontinuity of electric field normal to the wall (in $\hat{j}$ direction) [4, 154]:

$$\nabla^{\perp}\phi = -\sigma/\epsilon_0\epsilon_r. \tag{5.6}$$

Even though the surface charge density may slightly vary depending on a number of factors, such as pore diameter and concentration [5], it was assumed to be constant to maintain the simplicity of the problem. As shown in Fig. 5.1b, constant electrode potential across the nanofluidic RED cell, acting as a battery, was modelled, i.e. $\phi = k$, where $k = 0$ for the right-hand-side electrode and $k = \phi_c$ for the left-hand-side electrode [94, 5]. Here, the boundary condition of ϕ_c is associated with the operating voltage of the RED battery cell, with a net ion flux due to diffusion, electromigration, and convection. Along the rest of the walls, due to no accumulation of a net surface charge, following Eq. (5.6) we used the boundary conditions of $\nabla^{\perp}\phi = 0$, i.e., the gradient of ϕ in the direction normal to the wall is zero.

To compute the concentration of cations and anions, c_+ and c_- were numerically solved based on the Nernst-Planck Eq. set (5.5) with appropriately specified boundary conditions for cation/anion concentrations (c_+ and c_-) or fluxes (J_+ and J_-). To model a simplified, realistic operation of RED with external flow, two different concentrations of electrolyte: c_H for high and c_L for low concentration solution were injected and thus specified for both c_+ and c_- at the two reservoir inlets. Whereas, at the reservoir outlets, ionic flux is conserved and determined according to the local diffusive and advective ionic flux, without an electro-

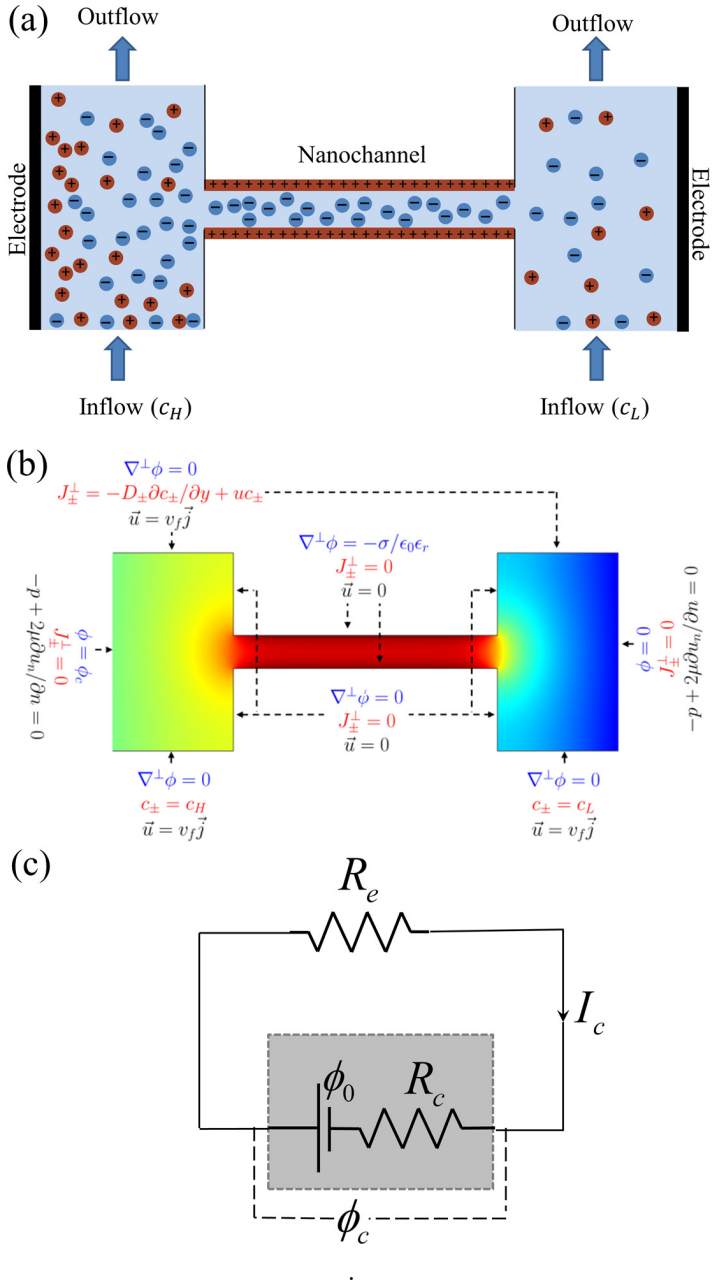

Figure 5.1: (a) Schematic diagram, (b) boundary conditions, and (c) equivalent electrical circuit of our computational model studying reverse electrodialysis flow, comprised of two reservoir flows of different salt concentrations connected by a positively charged nanochannel. In (c), ϕ_0, ϕ_c, R_c, R_e and I_c are the open-circuit voltage, operating voltage, nanochannel resistance, external resistance, and circuit current, respectively.

migration counterpart (as $\nabla^{\perp}\phi = 0$ at the reservoir outlets). Along the charged nanochannel and vertical surfaces, the boundary condition of $J_{\pm}^{\perp} = 0$ is used [4], corresponding to no net fluxes of ions outwards (in the direction normal to the surfaces). This vanishing ionic flux at the boundary is due to non-perpetrating ionic flow and a constant surface charge (steady σ on the nanochannel surface or zero on the vertical surfaces) and, therefore, zero normal component of the ionic fluxes ($J_{\pm}^{\perp} = 0$) at these boundaries.

For solving for the flow field, a combination of no-slip ($u_t = \vec{u} \cdot \hat{t} = 0$) and no-penetration ($u_n = \vec{u} \cdot \hat{n} = 0$) boundary conditions for the flow velocity was imposed along the nanochannel wall. More specifically, $\vec{u} = u_t = u_n = 0$ along the non-moving solid walls. Two different concentrations of electrolyte (c_H for high and c_L for low concentration solution) were injected at the two reservoir inlets with the same speed $\vec{u} = v_f \hat{j}$. Along the side-boundary of the two large reservoirs, the boundary stress ($= -p + 2\mu\partial u_n/\partial n$) was assumed to be zero (as we do not impose a pressure gradient horizontally across the RED cell). As a 2D model, the parameters were considered independent of z direction.

5.2.3 Electrical outputs computed

Fig. 5.1c shows the equivalent electrical circuit for the present RED model. The central grey portion represents the modeled RED cell, which essentially acts as a miniature battery with an electric potential (ϕ_0) and internal resistance (R_c), providing electrical energy to an external circuit. When connected to an external resistance (R_e), the voltage supplied by the RED cell is ϕ_c with an electric current (I_c). Since a fraction of ϕ_0 is consumed by the nanochannel internal resistance, R_c, the effective RED cell voltage (ϕ_c) can be expressed as:

$$\phi_c = \phi_0 - I_c R_c. \tag{5.7}$$

As visible from the electrical circuit diagram shown in Fig. 5.1c, the operating voltage (ϕ_c) can also be expressed as:

$$\phi_c = I_c R_e. \tag{5.8}$$

The current I_c can be calculated from the cationic and anionic flux across the nanochannel

cross-section [65, 155], using

$$I_c = \int F\left(z_+ J_+ + z_- J_-\right) dA. \tag{5.9}$$

The maximum supply voltage of the RED cell is termed as open-circuit voltage, ϕ_0 [84, 93, 5] (when no external current I_c is present). The maximum current that can flow through the circuit for a given configuration is termed as short-circuit current (I_{sc}) and is mathematically expressed as $I_{sc} = \phi_0/R_c$ [94]. I_{sc} can also be defined as the current flowing through the circuit when there is no external resistance.

In the simulations, we obtain the current-voltage characteristics of the RED cell using the numerical integral of Eq. (5.9). The method consists of using several different values of operating voltage ϕ_c (or equivalently, varying external resistance R_e) and obtain the resultant I_c using Eq. (5.9). The resultant I-V curve of the RED cell reveals a linear relationship described by Eq. (5.7), and we perform a curve fitting of least-square residuals. The corresponding open-circuit voltage, ϕ_0, and nanochannel resistance, R_c, are calculated from the y-intercept and the (negative) slope of the best linear I-V fitting, respectively.

The power output for a single nanochannel $P_c'\,(= \phi_c I_c)$ can be estimated by combining Eq. (5.7)–eq5.8,

$$P_c' = \phi_0^2 \frac{R_e}{\left(R_e + R_c\right)^2}. \tag{5.10}$$

By optimizing Eq. (5.10), the maximum power output, $P_{c,m}'$, occurs when the channel resistance is equal to the external resistance (i.e., $R_e = R_c$) or, equivalently, when the operating voltage is equal to the half of the open circuit voltage: $\phi_c = \phi_0/2$. Hence, $P_{c,m}'$ can be estimated using

$$P_{c,m}' = \frac{\phi_0^2}{4R_c}. \tag{5.11}$$

The maximum power output density ($P_{c,m}$) is the maximum power output ($P_{c,m}'$) per unit cross-sectional area $A_c\,(= h\times 10\ \mu\text{m})$ of the nanochannel, where the width of the nanochannel is considered to be 10 μm (similar to that used in previous numerical studies without external flow [4]).

Energy conversion efficiency (η) for the RED process can be defined as the ratio of output energy ($= \phi_c I_c$) to the Gibbs free energy due to the salinity difference [5]. The power generation is maximized at $\phi_c = \phi_0/2$, and the corresponding energy conversion efficiency at the maximum power output (η_m) is calculated via the following equation [83]:

$$\eta_m = \frac{\phi_0 I_c}{2RT \ln(c_H/c_L) J_s}, \tag{5.12}$$

where J_s is the total number of ions transported through the nanochannel per unit time and is equal to the integration of the sum of cationic and anionic flux over the nanochannel cross-section ($J_s = \int (J_+ + J_-)\, dA$). Here, we have assumed the activity coefficient of all species to be constant and equal [65].

To investigate the percentage of ions transported from one reservoir to the other via the nanochannel, we calculate the ratio of outflow to inflow concentration of the counter-ion (i.e., anion) in the high-concentration reservoir. We quantify this anion concentration ratio, δ, using

$$\delta = \frac{c_{-,out}}{c_H}, \tag{5.13}$$

where $c_{-,out}$ is the average anion concentration at the (left-hand-side) c_H reservoir exit. $\delta = 1$ indicates the concentration at entry and exit are equal, and hence there may be no effective ion transfer through the nanochannel. $\delta = 0$ may represent a complete transfer of anions towards the nanochannel from the reservoir. This analysis is based on the anion concentration (c_-) because anions dominate the charge distribution in the positively-charged nanochannel.

5.3 Numerical simulations

The present 2D numerical simulation has been performed in COMSOL Multiphysics, and the details of our numerical simulation including code validation, and grid independence analysis has been provided in chapter 2.

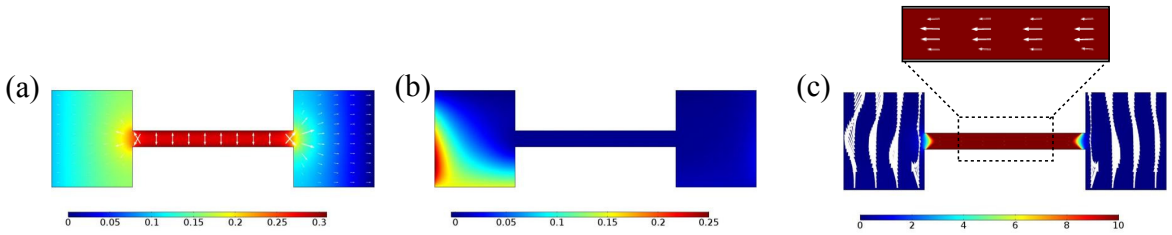

Figure 5.2: Simulation results for a charged nanochannel of $h = 10$ nm: (a) electric potential, ϕ, with electric field, $\vec{E}$ (in arrows), (b) cationic concentration, c_+, and (c) anionic concentration, c_-, with velocity vector, $\vec{v}$ (in arrows). The inset in (c) show the flow velocity vectors in the charged nanochannel. Here, $l = 100$ nm, $c_L = 0.01$ mM, $c_H = 0.15$, $\sigma = 0.01$ C/m^2, and $v_f = 0.07$ mm/s, with $\phi_c = 0.1$ V.

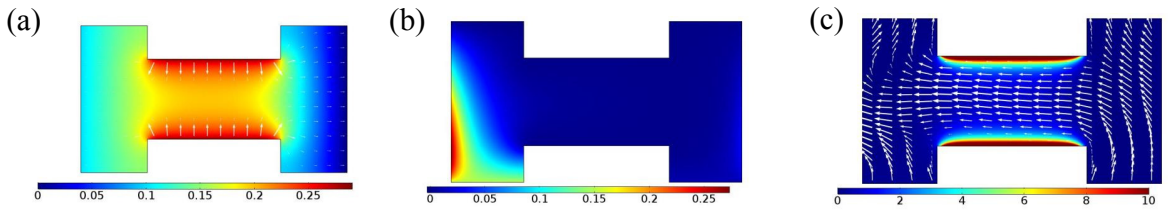

Figure 5.3: Simulation results for a wider nanochannel with $h = 60$nm: (a) electric potential, ϕ, with electric field, $\vec{E}$ (in arrows), (b) cationic concentration, c_+, (c) anionic concentration, c_-, with velocity vector, $\vec{v}$ (in arrows). Here, $l = 100$ nm, $c_L = 0.01$ mM, $c_H = 0.15$, $\sigma = 0.01$ C/m^2, and $v_f = 0.07$ mm/s, with $\phi_c = 0.1$ V.

5.4 Results and discussions

The control parameters of a RED energy harvesting unit include the concentrations of concentrated (c_H) and dilute (c_L) solutions, nanochannel dimensions (l, h), flow velocity (v_f), and surface charge density (σ). These factors can have a significant impact on the maximum power output density, $P_{c,m}$, and energy conversion efficiency, η_m, of the power generation process. Here, we investigate the influence of the first five listed parameters (c_H, c_L, l, h, v_f), while keeping the surface charge density (σ) constant.

5.4.1 Typical results

The distributions of ion concentrations (c_+, c_-), electric potential (ϕ), and velocity vector ($\vec{u}$) for two different nanochannel configurations, $h = 10$ and 60 nm, are shown in Figs. 5.2 and 5.3, respectively. The range of nanochannel dimensions was chosen based on typical scales of charged (membrane) nano-pores or nanochannels used by other experiments [100, 102] and by previous simulations [4, 5]. The nanochannel size is chosen to span the range comparable to the Debye length of the RED system, ($\lambda_D = \sqrt{\epsilon_0 \epsilon_r RT/2F^2 c_0} \simeq 10$ nm for electrolyte concentration $c_0 = 1$ mM [65]) since the ratio represents the effectiveness of the charge selectivity of the nano-confinement. The key idea here is to test this typical range of dimension to obtain optimal power generation, spanning narrow channels of $\mathcal{O}$ (10 nm)—which are charge selective due to overlapping Debye length—and wider channels of $\mathcal{O}$ (60 nm).

Fig. 5.2 shows the results for a relatively narrow nanochannel ($h = 10$ nm) with overlap of electric double layer (EDL). Electric double layer (EDL) plays a crucial role in nanofluidic flow under an electrical field, particularly in determining the charge selectivity of a nanopore. For instance, electric Coulombic force between the charges repels the co-ions from entering the EDL adjacent to the charged nanochannel. Thus, a strong charge-selectivity can be observed inside the nano-confinement when there is EDL overlap.

Fig. 5.2a shows the distribution of electric potential, ϕ, and the electric field, $\vec{E}$ $(= -\vec{\nabla}\phi)$. For the overlapping EDL case of $h = 10$ nm, due to strong and positive surface charge, σ, the highest electric potential is observed inside the nanochannel, leading to the electric field directing outward from the nanochannel towards the reservoirs. Combined with Eq. (5.1), the boundary condition of σ determines the local distribution of ϕ through Eq. (5.6), where $\nabla^{\perp}\phi = -\sigma/\epsilon_0\epsilon_r < 0$ in the direction normal to the nanochannel surface. As positive σ repelling (co-ion) cations away while attracting anions, Fig. 5.2b shows the accumulation of co-ions (cations) towards the edge of the reservoirs due to the repulsion from the positively-charged nanochannel. As counter-ions, anions are attracted to the nanochannel resulting in a high anion concentration inside the nanochannel, as illustrated by Fig. 5.2c. Consequently, net negative charge is present in the nanochannel. The flow velocity (depicted by arrows in the

inset of Fig. 5.2c) is directed from low (c_L) to high (c_H) concentration reservoir, primarily, due to the electric forcing (with $\phi_c = 0.1$ V on c_H-sided and 0 V on c_L-sided electrode) acting on overall negatively-charged solution present in the nanochannel.

Fig. 5.3 shows the profiles of output parameters for a wider nanochannel ($h = 60$ nm) without EDL overlapping. By the same token, the distributions of electric potential (ϕ) and cationic concentration (c_+) (shown in Fig. 5.3(a) and (b), respectively) are similar to those in a narrow nanochannel (Fig. 5.2). However, in contrast to $h = 10$ nm, the variation of electric potential in the y-direction is clearly visible in this case since the double layer do not overlap for $h = 60$ nm. Fig. 5.3c illustrates that the anionic concentration (c_-) is greater close to the walls of the nanochannel while relatively lower in the bulk of the nanochannel. Thus, without an overlapping EDL, the charge selectivity of the nanochannels is diminished in a wider channel. As illustrated by Fig. 5.3(c), for a wider channel, the nanoflow direction is from low to high concentration reservoir for some configurations. Such diffusioosmotic flow driven by chemiosmotic and electroosmotic processes has been studied in detail elsewhere [136, 148, 140, 166]. Here, we focus on the RED electrical characteristics and power generation of such nanofluidic configurations.

5.4.2 Influence of nanochannel dimensions

The nanochannel height, h, affecting the overlapping of EDL, is one of the significant parameters for RED [213]. Besides, the nanochannel length, l, can also contribute to the charge-selective effect by strengthening the Coulomb repulsion of the co-ions as more surface charge is present when l is increased. Using Eq. (5.7)-(5.13), we examine the variation of electrical outputs with nano-channel length (l) for three different heights ($h = 10$ nm, 30 nm, and 50 nm), while keeping the other parameters (c_H, c_L, v_f, σ) constant.

The variation of nanochannel resistance, R_c (Fig. 5.4a), open-circuit voltage, ϕ_0 (Fig. 5.4b), and energy conversion efficiency, η_m (Fig. 5.4e) with l for different h reveal a similar trend, demonstrating an insignificant impact of nanochannel height (h) for the h-range explored. For example, R_c increases monotonically with an increase in l for all h, which can be explained with the increasing electrical resistance with length (since $R = \rho_R \frac{l}{A}$, where ρ_R is

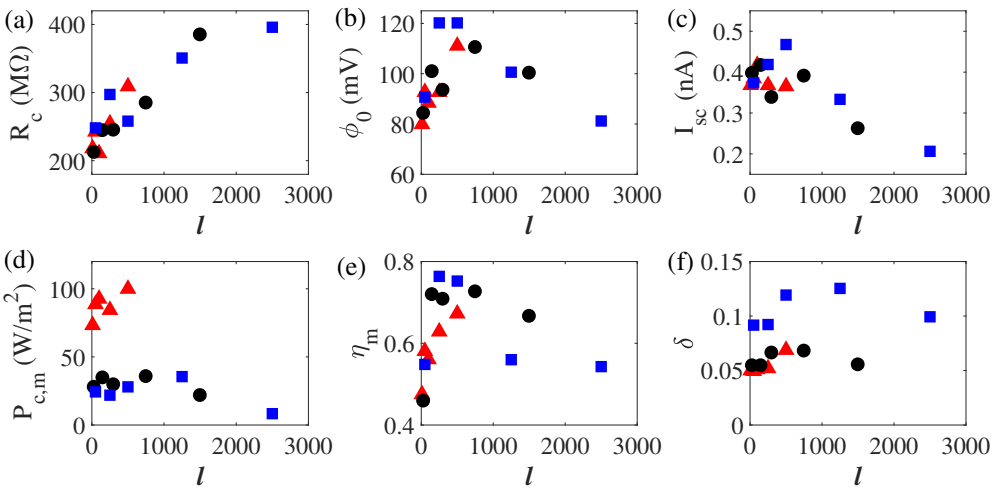

Figure 5.4: Dependence of (a) nanochannel resistance, R_c (in MΩ), (b) open-circuit voltage, ϕ_0 (in mV), (c) short-circuit current, I_{sc} (in nA), (d) power output density, $P_{c,m}$ (in W/m^2), (e) energy conversion efficiency, η_m, and (f) anion concentration ratio, δ, on nanochannel length, l (in nm), for different height h = 10 nm (▲), 30 nm (●) and 50 nm (■). Here, c_H = 0.25 mM, c_L = 0.01 mM, v_f = 0.01 mm/s, and σ = 0.01 C/m^2.

the electrical resistivity of the material, and A is the cross-sectional area).

ϕ_0 rapidly increases with l for l < 300 nm and subsequently decreases with increasing l between 400 and 3000 nm. Both ϕ_0 and η_m are observed to reach a maximum value at a specific l (≈ 300 nm) after which both decrease as l increases. Overall, these electric outputs show an optimal channel length for higher and efficient power output. The following factors likely explain such optimization with respect to l. As l increases, the total charges along the nanochannel increase, and Coulombic forces are strengthened to enhance the electroosmotic transport. On the other hand, an increase in l decreases the concentration gradient ($\sim \Delta c/l$) in the nanochannel and lessens the chemiosmotic transport. Because of the combination of these competing factors, a critical l was observed for the maximization of power generation. Fig. 5.4c illustrates the variation of the short-circuit current, I_{sc}, which decreases with an increase in l and shows small variation with different h. The observed reduction in I_{sc} with increasing l can be attributed to increasing R_c and the reduction of strength of the driving force due to concentration gradient with increasing l.

Revealed in Fig. 5.4d is the variation of maximum power output density ($P_{c,m}$ obtained

using Eq. (5.11)) with l for different h, showing a much higher value of $P_{c,m}$ for narrower channel ($h = 10$ nm). To explain this, we observed that the power output ($P'_{c,m}$) for all three heights are of the same order of magnitude, while the density ($P_{c,m}$) is the power divided by the effective cross-sectional area A_c ($= h\times 10\ \mu$m) and hence increases with decreasing h. The variation of $P_{c,m}$ with l was less pronounced.

The variation of anion concentration ratio, δ, defined in Eq 5.13, with nanochannel dimensions, shown in Fig. 5.4f, reveals the dependence of δ primarily on h but not on l. In particular, when h = 50 nm, δ is increased about twice compared to those for h = 10 and 30 nm. The higher δ observed for larger h indicates that most anions pass through the reservoirs and do not transport through the nanochannel, as expected for the case of a wider nanochannel ($h > \lambda_D$) with less charge selectivity.

Previous 1D investigations have reported that the nanochannel aspect ratio ($n_R = l/h$) could be an important factor in determining the flow profile and characteristics of DOF, especially when $n_R < 5$ [138]. In this regard, we also studied the dependence of electrical outputs on n_R for our geometry with a constant external flow of ionic solutions. Nanochannel resistance R_c increased linearly with increase in n_R. However, it was observed that all the electric outputs except R_c did not demonstrate any significant influence of n_R for the parameter ranges explored. Fig. 5.5 shows the variation of output parameters with nanochannel aspect ratio ($n_R = l/h$) for different h. Nanochannel resistance, R_c, increases linearly with n_R but does not change much with h (Fig. 5.5a). The variation of open circuit voltage, ϕ_0, and energy conversion efficiency at maximum power, η_m, are shown in Fig. 5.5b and Fig. 5.5e, respectively, showing no noticeable influence of n_R and h. Short-circuit current (I_{sc}) increases with decreasing h but does not change with n_R (see Fig. 5.5c). Fig. 5.5d reveals that maximum power output density, $P_{c,m}$, increases with increasing h but remains fairly constant for different n_R. Fig. 5.5f shows that anion concentration ratio, δ, is independent of n_R but dependent on h to some extent. This analysis shows that most electrical outputs do not change significantly with varying n_R for the parameter ranges used.

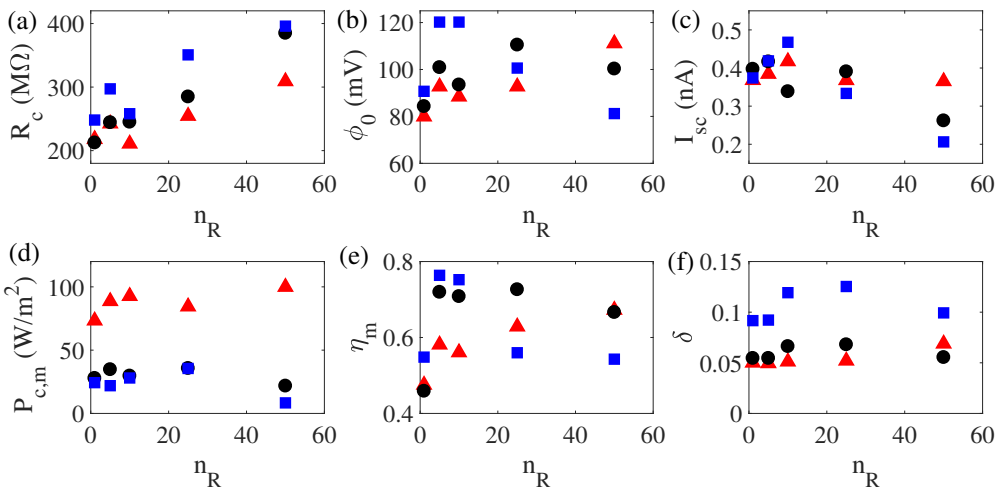

Figure 5.5: Variation of (a) nanochannel resistance, R_c (in MΩ), (b) open-circuit voltage, ϕ_0 (in mV), (c) short-circuit current, I_{sc} (in nA), (d) power output density, $P_{c,m}$ (in W/m^2), (e) energy conversion efficiency, η_m, and (f) anion concentration ratio, δ, with nanochannel ratio $n_R = l/h$ for different heights h = 10 nm (▲), 30 nm (●), and 50 nm (■). Here, c_H = 0.25 mM, c_L = 0.01 mM, v_f = 0.01 mm/s, and σ = 0.01 C/m^2.

5.5 Electric outputs with varying channel aspect ratio

5.5.1 Effect of concentration gradient

We also study the effects of changes in concentration (and concentration gradient) on RED power generation. The analysis is performed by varying c_H and c_L, while keeping other control parameters (l, h, v_f, σ) constant.

Fig. 5.6a shows the variation of the nanochannel resistance, R_c, for different concentration ratio, c_R (= c_H/c_L). An exponential dependence of R_c on c_R is observed, where R_c decreases with increasing c_R. R_c also decreases as c_L increases. These R_c dependence reveals an enhanced ion transport (resulting in a lower R_c) with greater concentration ratio due to diffusion and electromigration (i.e., the first two terms in Eq. (5.2)). By the same token, Fig. 5.6b shows that the open circuit voltage, ϕ_0, increases with an increase of c_R for $c_R \leq 50$, albeit with a decreasing rate. For $c_R > 50$, ϕ_0 vary slightly with c_R and can be considered to remain nearly constant. On the other hand, it can be seen from Fig. 5.6c that there is a linear increase in short-circuit current (I_{sc}) with c_R. In other words, this maximum available

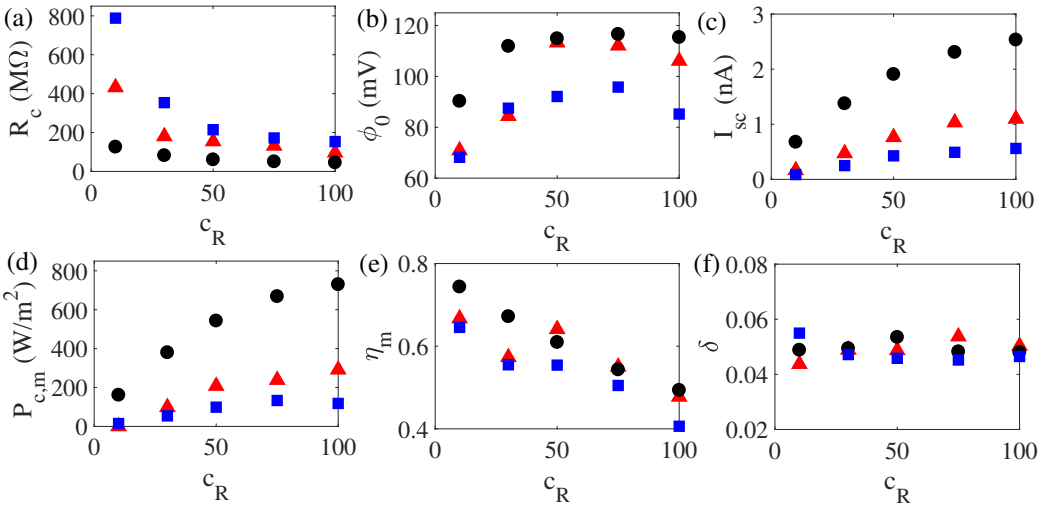

Figure 5.6: The influence of concentration ratio, $c_R(= c_H/c_L)$, on the electric outputs of (a) nanochannel resistance, R_c (in MΩ), (b) open-circuit voltage, ϕ_0 (in mV), (c) short-circuit current, I_{sc} (in nA), (d) power output density, $P_{c,m}$ (in W/m^2), (e) energy conversion efficiency, η_m, and (f) anion concentration ratio, δ ($< \delta > \simeq 0.05$), for different c_L=0.005 mM (■), 0.01 mM (▲), and 0.05 mM (●). Here, h = 10 nm, l = 100 nm, σ = 0.01 C/m^2, and v_f = 0.01 mm/s.

current is increased with c_R (for a fixed c_L) since the concentration gradient is a primary driving force for the ionic transport and, hence, the resultant current. In addition, I_{sc} also increases with an increase in c_L. For a constant c_R, if c_L increases, the concentration gradient is greater and causes an increase in ionic flow and circuit current.

Fig. 5.6d shows the variation of maximum power output density ($P_{c,m}$) with concentration ratio (c_R) for different c_L, illustrating that $P_{c,m}$ increases almost linearly with increase in c_R. This increase of $P_{c,m}$ with c_R is higher for larger c_L. High values of both c_R and c_L can enhance ion flux due to chemiosmosis in the nanochannel and, hence, generate larger $P_{c,m}$.

The variation of energy conversion efficiency (η_m) (at the maximum power output using Eq. (5.12)) with c_R is shown in Fig. 5.6e. Interestingly, η_m decreases nearly linearly with an increase of c_R, implying a reduction in the RED process efficiency if the concentration ratio is very high. The approximate linear dependence of η_m observed can be expressed as $\eta_m = 0.0023(300 - c_R)$ using a least-square linear fit. However, η_m is nearly independent of the concentration of the dilute solution (c_L). It was interesting to note from Fig. 5.6f that

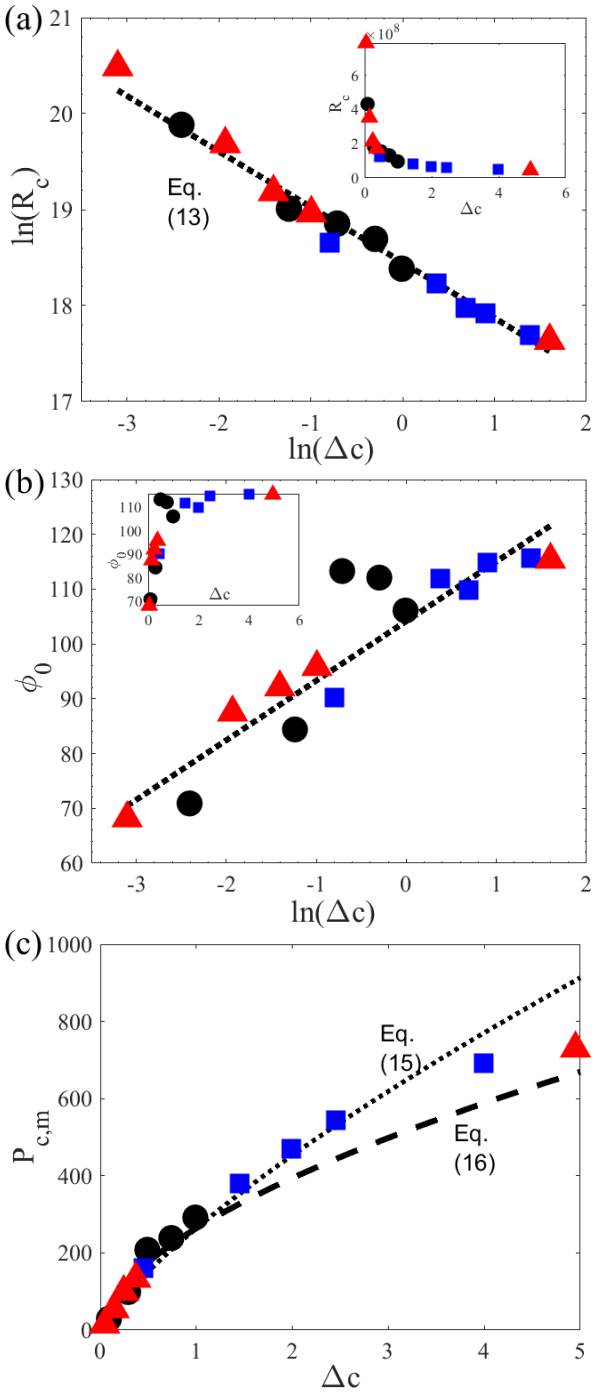

Figure 5.7: Variation of (a) R_c (in MΩ), (b) ϕ_0 (im mV), and (c) $P_{c,m}$ (in W/m^2) with the concentration difference, $\Delta c = c_H - c_L$ (in mM), for $c_L = 0.005$ mM (▲), 0.01 mM (●), and 0.05 mM (■). Here, $h = 10$ nm, $l = 100$ nm, $\sigma = 0.01$ C/m^2, and external flow velocity $v_f = 0.01$ mm/s. The lines indicate the best fitting curves in accordance to the empirical relations observed, with their corresponding Eq. numbers labeled.

anion concentration ratio (δ) does not significantly change with solution concentrations and remains fixed at around 5% for low external-flow velocity ($\sim$ 0.01 mm/s).

These results reveal that electrolyte concentration ratio (c_R) plays a significant role in maximizing sustainable power outputs. As shown by Fig. 5.6 for h = 10 nm and c_L = 0.05 mM, due to strongly enhanced chemiosmosis transport a greater $c_R \approx 100$ can greatly decrease nanochannel resistance (R_c by 5.1 times), increase short-circuit current (I_{sc} by 6.4 times), and increase maximizing power density ($P_{c,m}$ by 4.5 times) compared to the cases for c_R = 10. Moreover, for a fixed c_R, a large ion concentration (c_L) benefits the RED process and electrical outputs since more ions are available contributing to greater ionic fluxes.

When we plot the electrical outputs, R_c, ϕ_0, and $P_{c,m}$ *vs.* the concentration difference Δc ($= c_H - c_L$), remarkably, all data points for different c_H and c_L could be fitted into a single curve. As illustrated by Fig. 5.7a, a power-law dependence can be obtained for the channel electric resistance, R_c:

$$R_c = A\Delta c^{-\alpha}, \tag{5.14}$$

where A and α are positive constants which could depend on other factors, such as nanochannel dimensions, surface charge density, and flow velocity. For the present configuration (h =10 nm, l = 100 nm, σ = 0.01 C/m^2, and v_f = 0.01 mm/s), A = 102.86 and α = 0.58 (when R_c is in $M\Omega$). Since a lower value of channel resistance is desired for higher electrical output, the empirical relation suggests an optimization using a higher value of Δc, i.e., a greater concentration gradient. Eq. (5.14) also reveals that the electrical conductance, $K_c \sim 1/R_c \sim \Delta c^{\alpha}$, increases exponentially with the concentration gradient.

Shown in Fig. 5.7b is the dependence of ϕ_0 on Δc, which can be expressed through a logarithmic relation:

$$\phi_0 = B \ln \Delta c + \beta, \tag{5.15}$$

where for the present configuration, B = 10.87 and β = 104.18 (when ϕ_0 is in mV). These constants may be functions of other factors which are considered constant in the present analysis. When $B \ln \Delta c \ll \beta$, we can approximate $\phi_0 \approx \beta$ (see the inset in Fig. 5.7b) for $\Delta c \gtrsim 1$.

The maximum power output density ($P_{c,m}$) is related to R_c and ϕ_0 according to Eq. (5.11). Thus, the variation of $P_{c,m}$ can be obtained using the relations (5.14) and (5.15):

$$P_{c,m} = \frac{\phi_0^2}{4R_c}\frac{1}{A_c} = \frac{(B\ln\Delta c + \beta)^2}{4A\Delta c^{-\alpha}}\frac{1}{A_c}. \tag{5.16}$$

Upon expansion of Eq. (5.16), the contribution of two of the three terms were found to be negligible. Thus, a further approximation of the above equation can be performed by expressing $P_{c,m}$ as a power-law dependence on Δc, with the absolute value of the exponent α being the same as in Eq. (5.14). This simplified equation is described by

$$P_{c,m} \approx C\Delta c^{\alpha}\frac{1}{A_c}, \tag{5.17}$$

where the constant $C = \beta^2/4A$ ($\simeq 26.4$). The behavior of the approximated functions given by Eq. (5.16) and (5.17) are illustrated in Fig. 5.7c. Our numerical results show an increasing $P_{c,m}$ with Δc, consistent with the experimental results reported by Kim et al. using anodic alumina nanoporous membranes [152]. In brief, the new empirical relations of R_c, ϕ_0 and $P_{c,m}$ (i.e., Eq. (5.15), 5.14 and 5.17) found numerically depend on Δc and are useful for an easy prediction of RED operations for optimal electrical outputs.

5.5.2 Effect of Peclet number

The influence of Peclet number due to external flow on the electric outputs for the nano/micro-junction RED is unraveled for the first time, by Fig. 5.8. The Peclet number is defined as the ratio of convective to diffusive transport. Here, we use $Pe = v_f h/D$, where v_f, h and D ($= 2\times10^{-9}$ m^2/s) are the inflow velocity, nanochannel height, and average diffusivity, respectively. In our model using K^+ and Cl^- ions, the ionic diffusivities are of the same order of magnitude as the nanochannel height. Thus, a very high flow velocity ($\sim$ 1 m/s) would be required to achieve high Pe flows. It is experimentally rather challenging to reach such velocities in nano-confinements because extremely large forcing is required to overcome nano/micro-flow viscous dissipation. Due to nanoscale devices, our analysis hence focuses on $Pe \leq 10$.

The internal resistance of the RED cell (R_c) remains fairly constant in low Peclet number and decreases when $Pe \gtrsim 1$, as shown in Fig. 5.8a. No considerable changes of the electrical

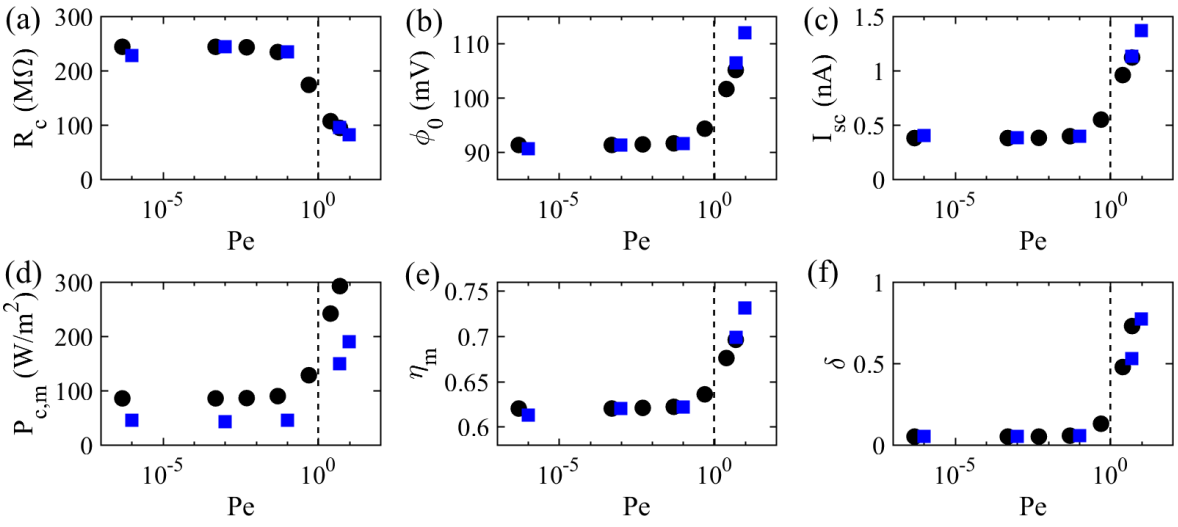

Figure 5.8: Impact of the Peclet number ($Pe = v_f h/D$) due to external flow on the electrical outputs of (a) nanochannel resistance, R_c (in MΩ), (b) open-circuit voltage, ϕ_0 (in mV), (c) short-circuit current, I_{sc} (in nA), (d) power output density, $P_{c,m}$ (in W/m^2), (e) energy conversion efficiency, η_m, and (f) anion concentration ratio, δ, for different nanochannel heights: h = 10 nm (■) and 20 nm (●).

outputs with Pe are observed for low Peclet number, $Pe \lesssim 1$. It is worthy noting that the significant increase of ϕ_0, I_{sc}, and $P_{c,m}$ when $Pe \gtrsim 1$ reveals the strong influence of convection (Figs. 5.8b, 5.8c, and 5.8d). These observations can be explained by the fact that at high Pe, in addition to diffusion, advection due to external flow can contribute to larger ion flux and, hence, greater electric power output for the RED system.

Our numerical data show that the average flow inside the nanochannel when $Pe \gtrsim 1$ is at least an order of magnitude greater than that for $Pe < 1$. Higher flow velocity facilitates a higher transfer of counter-ions across the nanochannel and, therefore, increases the ion transfer. Enhanced ionic flow results in a higher current through the RED circuit; consequently, power output density increases as well. More quantitatively, the output power density was found to increase 2.3× for both h = 10 nm and 20 nm when the flow changes from low ($Pe < 1$) to high Peclet number regime ($Pe \geq 1$). Similarly, energy conversion efficiency, η_m, displays the same trend as I_{sc} and ϕ_0, staying nearly constant for $Pe < 1$ while increasing when $Pe \gtrsim 1$ (see Fig. 5.8e). As the inflow velocity is increased, the conversion of Gibb's free energy of mixing to electrical energy is boosted by 10% due to the dominance of convection

over diffusion when $Pe \geq 1$ with ample supply of fresh ions from the external flow.

A high inflow velocity (i.e., $Pe > 1$) ensures a steady supply of ions across the nanochannel and enables higher electrical output. However, because of this high velocity, most ions flow out of the reservoir, and only a small fraction of total ions supplied crosses from one reservoir to another to generate current. This causes a high salt concentration of the outflow solution, and thus the ratio δ ($= c_{-,out}/c_H$) increases with Pe, as revealed by Fig. 5.8f. The concentration of the outflowing anionic solution increases by more than 50% when the flow transitions from $Pe < 1$ to $Pe \geq 1$. This may generate an abundance of wasting saline and reduces the utilization of available resources. For the nanochannel height explored here, these electrical outputs did not vary significantly for different h used.

5.6 Conclusion

We numerically investigate the performance of a reverse electrodialysis cell under the influence of external flows in two reservoirs, which are connected by a charged nanochannel. Electrolyte solutions of different concentrations flow through the reservoirs and generate a chemical potential gradient across the nanochannel. The governing equations are based on the conservation of mass, charges, and momentum, describing the nonlinear and coupled relations between electric potential, ion concentration, and flow fields. The nonlinear coupling of surface charge, concentration gradient, and the resultant local electric fields govern the ionic flow through the nanochannel. The effect of electrolyte concentration, nanochannel dimensions, and external flow velocity on the maximum power output density ($P_{c,m}$), conversion efficiency (η_m), and anion concentration ratio (δ) have been analyzed in detail.

These electrical outputs were found to depend on both nanochannel height (h) and length (l). The simulation results show that a smaller h and an optimum value of l are desired for maximizing power density, $P_{c,m}$. The open-circuit voltage, ϕ_0, and energy conversion efficiency, η_m, increase with l till $l \approx 300$ nm, after that it remains relatively constant. Our investigation also reveals an insignificant dependence of electrical outputs on nanochannel aspect ratio, $n_R = l/h$, for the parameters explored.

Both $P_{c,m}$ and ϕ_0 increases with an increase in concentration ratio, c_R, whereas the channel electric resistance, R_c, decrease exponentially. Energy conversion efficiency, η_m, on the other hand, shows a steady decrease with an increase of c_R. This implies that the overall efficiency of capturing the Gibbs free energy of mixing decreases as c_R increases. More importantly, the RED electrical output characteristics can be empirically modeled based on concentration difference Δc $(= c_H - c_L)$, using Eq. (5.14)–(5.16). While, R_c and $P_{c,m}$ also show a power-law dependence on Δc. To the best knowledge of ours, effect of inflow velocity of both reservoirs was numerically analyzed for the first time for the RED using single nanochannel. Both $P_{c,m}$ and η_m increase with an increase in Pe when $Pe \geq 1$, as the supply of fresh ions is abundant. However, a linear decreasing relationship was observed between anion concentration ratio, δ, and Pe.

In summary, the key numerical results by systematically varying several control parameters reveal that maximum power output ($P_{c,m}$) of the RED cell requires smaller h (such that $h \approx \lambda_D$), optimal l (≈ 300 nm), larger Δc, and higher v_f (Pe ≥ 1). These quantitative parameter values for the optimal RED output shed light on the importance of strong charge selectivity of the nanopores (facilitating ion transport in the nanochannel), appropriate l (for optimizing total electroosmotic and chemiosmosis ionic transport), greater ΔC (enhancing chemiosmosis transport due to strong drive of chemical potential gradient), and external flow (constantly supplying with fresh ions) for maximizing sustainable RED power. The study provides not only quantitative results of nonlinearly coupled flow, electric potential, and ion concentration fields for different flow conditions in a RED cell but significant parameters of experimental designs of nanopores for optimizing the renewable RED power under external flow. This work can be further developed to analyze the effect of multiple nanochannels on reverse electrodialysis energy. In future, it would also be very interesting to numerically investigate the effect of the combination of an alternating cation, and anion exchange membrane in a steady-state RED cell, with alternating flow of dilute and concentrated solutions. Moreover, motivated by biological ion-channels, it is exciting and crucial to numerically investigate the local flow, ion concentrations, and electrical outputs for a conical-shaped, charged nanochannel subjected to a (salt-) concentration gradient and external flow.

Chapter 6

Power generation through reverse electrodialysis using Nafion membrane

6.1 Introduction

Salinity gradient energy (SGE) is a promising source of renewable energy that can be harnessed by utilizing the chemical potential difference between freshwater and seawater. SGE can be captured using several technologies [214], such as reverse electrodialysis (RED) [80, 67], pressure-retarded osmosis [215], and electric double layer (EDL) capacitor [216]. Among these methods, RED, which exploits the charge selectivity of nanopores, has been an attractive, pollution-free alternative to harness the Gibbs free energy of mixing of electrolyte solutions [205]. The RED technology could potentially extract a power amounting to 2.24 MW when 1 m^3 of freshwater is mixed with seawater, [217] thereby potentially producing a sustainable power output of $\approx$ 2.6 TW, [198] estimated with a global freshwater flow-rate of $\approx 1.2 \times 10^6$ m^3/s. [206]

Since the first experimental record of RED by Pattle using alternating chambers of fresh and saline water separated by acidic and basic membranes, [81] there have been active the-

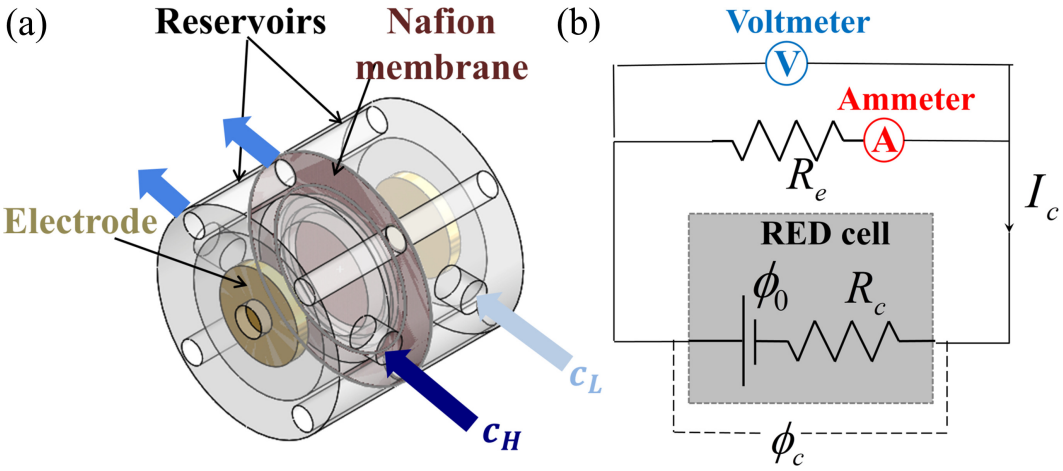

Figure 6.1: (a) Schematic and (b) the equivalent electrical circuit of the reverse electrodialysis (RED) cell, comprised of two reservoirs separated by a cation-selective Nafion membrane. Solutions of different salt concentrations (c_H and c_L) flow through the reservoirs. When connecting an external circuit to the two side-electrodes, we obtain the open-circuit voltage (ϕ_0) and internal resistance (R_c) of the RED cell under a constant flow rate, by measuring the operating voltage (ϕ_c) and current (I_c) with a voltmeter and ammeter, respectively, while varying the external resistance (R_e) connected.

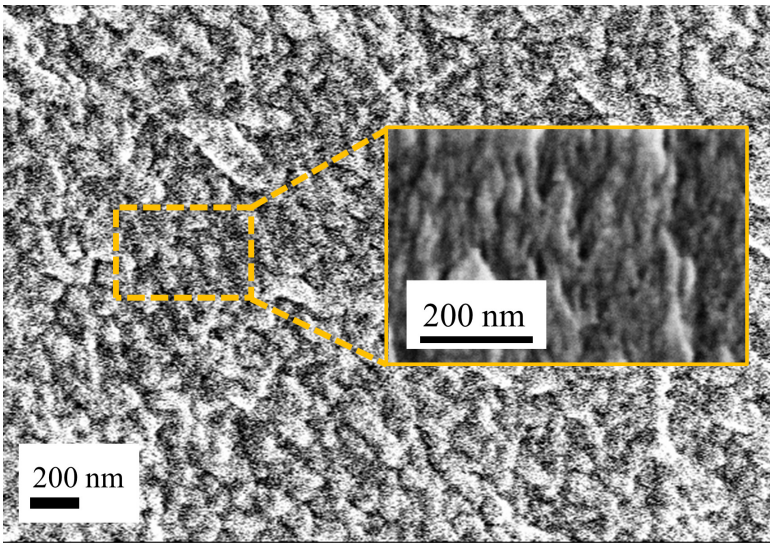

Figure 6.2: SEM image of the Nafion membrane used, with approximate nanopore diameter of 20 – 25 nm.

oretical, numerical, and experimental investigations to elucidate the underlying mechanisms and improve cell designs for better power output [83, 4, 94, 210, 5, 128, 212]. Theoretical studies of simplified RED models for a single charged nanochannel, using 1D Poisson-Boltzmann linearization of ionic concentrations, report the increase in energy conversion efficiency with an optimum ratio of the nanochannel radius to the Debye length [82, 83]. To elucidate pore-scale observations and understanding, researchers have recently investigated micro/nanofluidic RED processes to measure I-V characteristics of single [178, 218, 219] or an array of charged nanochannels [220, 221] between two microfluidic reservoirs under Δc. For example, to obtain clear pore-scale visualization, experimentalists used nanofabrication techniques to chemically etch single-pore nano/micro-junction RED cells on a polyimide membrane using NaClO and reported power output of the order of 26 pW [222, 223]. Besides, membrane-less RED cell design with closely-packed nanoparticles reported a much higher power output of the order of magnitude of nW [224, 150]. On the numerical front, the electrical responses of a single charged nanopore in two-dimensional micro/nano-junctions have been reported without external flow [4, 5], with an external flow of electrolytes [128], and for inhomogeneous surface charge [212].

For optimizing the large-scale implementation of RED technology with membranes, laboratory-scale experiments are performed with ion-exchange membranes to analyze the electrical response for various configurations of the RED cells, e.g., using different designs of spacers [225, 91, 226, 227], cyclic voltage variation [228], and wastewater as the electrolyte solutions [229]. Vermaas et al. reported a simplified model to obtain the net power density using the Nernst equation, which accounted for Ohmic losses [84], and compared their findings with experimental results of RED stack design for feedwater recirculation [85], co-, counter- and cross-flow [89], and multivalent ions [230].

Researchers have further investigated the energy harvesting capability of RED cell designs using various ion-exchange membranes, such as microfiltration membranes [95], commercial polymeric membranes [96], silica nanochannel of various heights and porosity [98, 99, 100], porous diaphragm [101], Al_2O_3 membrane [102], and charged polymeric membranes with tunable pore size and porosity.[97] One such membrane which demonstrates excellent charge-

selective characteristics is the Nafion membrane. Previous investigations using Nafion membranes, which focused on the electrokinetic energy conversion characteristics, reported a conversion efficiency ≃ 18% [103], and a monotonous increase of efficiency with temperature [104]. In spite of these comprehensive reports, to the best knowledge of ours, a detailed analysis of steady-state electrical measurements of a RED cell using the widely-used ion-selective Nafion membrane under various Δc has not been reported. Besides, the effect of the flow rate of incoming electrolyte solutions on the RED electrical output has been rarely explored. To fill these knowledge gaps, we experimentally investigate the electrical characteristics (e.g., internal resistance, open-circuit, and power output density) of a Nafion membrane, by systematically varying (salt-)concentration difference and flow rates of the electrolytes.

6.2 Materials and methods

We designed and fabricated a RED renewable power generation unit consisting of two reservoirs separated by a charge-selective Nafion membrane, illustrated in Fig. 6.1a. The fluidic cell was 3D-printed using stereo-lithography. A syringe pump was used to inject salt solutions of different concentrations through the two reservoirs at a particular flow rate. The salt solution was made by dissolving different amounts of sodium chloride (NaCl) in deionized water. The dilute solution used is deionized water, without any salt added. The cation-exchange membrane (CEM) used is a commercially available Nafion membrane (The Fuel Cell Store). The Nafion nanopores varied in shapes and sizes and were observed under a scanning electron microscope (SEM) to find an approximate pore-diameter to be 20–25 nm, as shown in Fig. 6.2. The cross-sectional diameter of the membrane held by the fluidic assembly is 17 mm, with the corresponding cross-sectional area, $A_c = 227$ mm^2.

When electrolyte solutions with a salt-concentration difference flow across the CEM, the RED cell-assembly (Fig. 6.1a) acts like a miniature battery with an electric potential (ϕ_0) and internal resistance (R_c), as depicted through the electrical circuit unit in Fig. 6.1b. ϕ_0 is known as the open-circuit voltage, or the voltage output when no current flows through the electrical circuit. When connected to an external resistance (R_e), the voltage supplied by the

RED cell is ϕ_c with an electric current, I_c. A voltmeter (Keithley 2450 Sourcemeter) and an ammeter (DigiKey 2831E) were used for electrical measurements of ϕ_c and I_c, respectively, while a variable resistance was used to control the external resistance, R_e. We used ten different values of R_e between 20 kΩ – 700kΩ, and the current (I_c) and voltage (ϕ_c) readings were recorded at 15 Hz for one minute. The I-V characteristics of the RED cell were obtained from the time-averaged values of I_c and ϕ_c, reaching a steady-state.

6.3 Results and discussions

Based on the electrical circuit diagram (see Fig. 6.1b), the I-V relation can be mathematically described as: $\phi_c = \phi_0 - I_c R_c$. Using this equation, both ϕ_0 and R_c of the RED cell can be calculated with a best linear-fit of our I-V measurements (i.e., ϕ_c and I_c data) from the y-intercept and the slope, respectively. We can also express ϕ_c using the external resistance (R_e): $\phi_c = I_c R_e$. Using the above two relations, we can obtain the RED power output $P_c' (= \phi_c I_c)$ in terms of the internal and external resistances:

$$P_c' = \phi_0^2 \frac{R_e}{(R_e + R_c)^2}. \tag{6.1}$$

By optimization, the RED power output, P_c', has a maximum when the operating voltage is equal to the half of the open circuit voltage: $\phi_c = \phi_0/2$, and can be estimated via:

$$P_{c,m}' = \phi_0^2/(4R_c). \tag{6.2}$$

The maximum power output density, $P_{c,m}$, is the maximum power output ($P_{c,m}'$) per unit cross-sectional area of the membrane (A_c). We analyzed the effects of Δc and flow rate on the electrical outputs and power density of the RED cell. We further compared our experimental results with numerical results of the RED electrical characteristics using a single charged nanochannel [128].

Revealed in Fig. 6.3a are the typical I-V measurements obtained for the RED cell under different flow rates, q_f. In the range of flow rates investigated (10 – 1000 μl/min), voltage ϕ_c has a linear dependence on I_c, showing a constant internal resistance ($R_c = -dV/dI$) of the RED cell. Further, as revealed by Fig. 6.3a, the I-V response does not vary significantly with

the change in the flow rate of the solutions. The power output density (P_c) from our setup can be found out from the I-V data using the relation: $P_c = I_c\phi_c/A_c$, where A_c is the membrane cross-sectional area confined by the fluidic assembly. Fig. 6.3b shows the results of the power output density, P_c for various q_f. In a good agreement with Eq. (6.2), the maximum power output density is always observed when $\phi_c = \phi_0/2$ for all the cases.

6.3.1 Influence of flow rate

We first investigated the influence of flow rates on the RED electrical and power outputs. For each flow rate, at least three experiments were conducted to obtain the error bars reported based on the standard deviation, while keeping the concentration difference constant (Δc = 0.86 M). As illustrated by Fig. 6.5, the internal resistance of RED cell, open-circuit voltage, and maximum power density demonstrated a slight variation with changes in the inflow rate. The average maximum power output density, $P_{c,m}$ was found to be around 0.5 mW/m^2. The average internal resistance (R_c) and open-circuit voltage (ϕ_0) were calculated to be 0.14 MΩ and 0.23 V, respectively.

In our experiments, we explored different flow rates over three orders of magnitude, ranging from 10 to 1000 μl/min. We found that a higher flow rate above 1 ml/min is too fast to achieve a complete set of steady-state electrical I-V measurements for our setup. Therefore, the flow range explored corresponds to a low Peclet number regime (via $Pe = v_f h/D$, which can be estimated with the flow velocity, v_f, a characteristic length scale for the RED processes, h, which could be approximated with the membrane thickness or dimension of the nanopores, and ion diffusion coefficient, D), where diffusion is expected to dominate over advection. When approximating h with the nanopore dimension or membrane thickness, the corresponding Peclet number ranges between 10^{-9} and 10^{-5} for our setup.

6.3.2 Effect of concentration difference

We further carried out a systematic study of a wide range of concentration difference Δc (= $c_H - c_L$), ranging from 0.51 mM to 1.71 mM. For the electrical measurements, we kept the salt concentration of the dilute solute fixed ($c_L \approx 0$), while the molarity of the concentrated

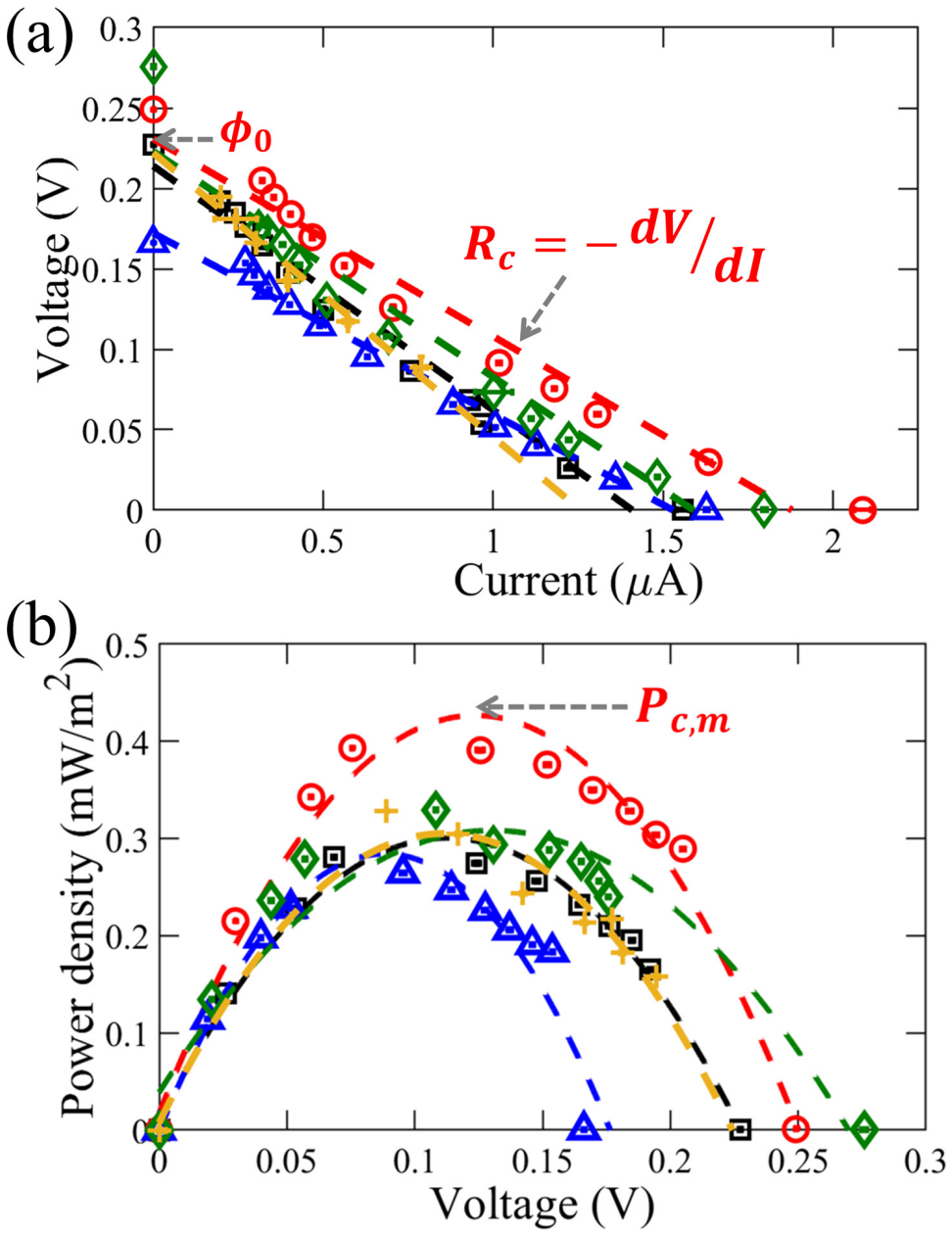

Figure 6.3: (a) Typical current-voltage (I-V) data measured and (b) the corresponding power density at different voltages of the RED cell using a Nafion membrane. Measurements of the open-circuit voltage (ϕ_0) and membrane internal resistance ($R_c = -dV/dI$) are obtained from the y-intercept and slope of the best linear fit of the I-V curve, respectively. The greatest value of the power density curve in (b) denotes the maximum power density, $P_{c,m}$. Here, each set of the experiments are ran at different flow rates, q_f = 10 (□), 100 (○), 500 (△), 750 (◊) and 1000 (+) μl/min, but with a constant salt-concentration difference, Δc = 0.86 M.

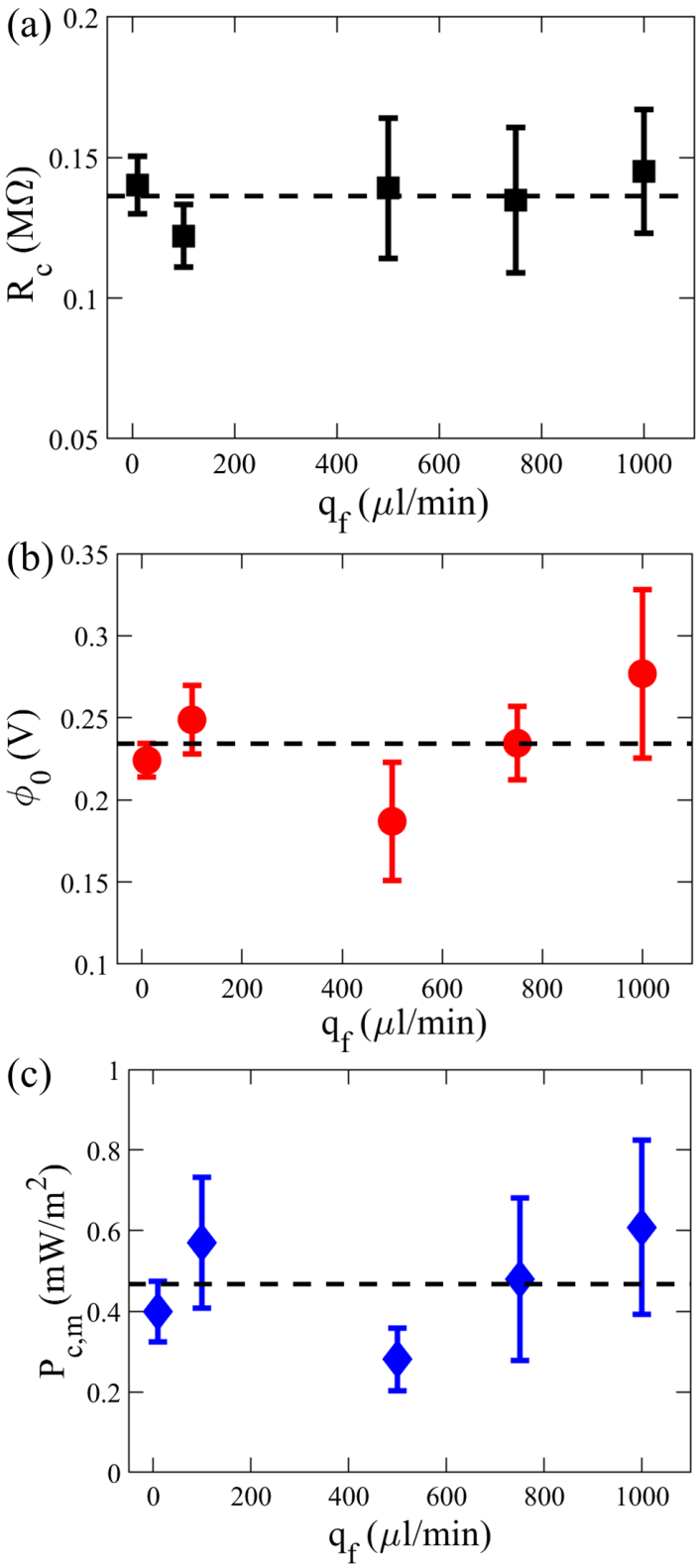

Figure 6.4: Insignificant variations of (a) internal resistance, R_c, (b) open-circuit voltage, ϕ_0, and (c) maximum power output density with a wide range of flow rate, q_f. The dashed lines in (a), (b) and (c) represent the average value of R_c, ϕ_0 and $P_{c,m}$ respectively.

solution was varied. The flow rate was kept constant at 1000 μl/min for studying the effect of Δc. We carry out investigations with five different values of Δc. For each Δc, at least three independent experiments were performed. Fig. 6.5 demonstrates the effect of Δc on the electrical characteristics, namely internal resistance, open-circuit voltage, and maximum power density, of the RED cell using a Nafion membrane.

Shown in Fig 6.5a is the measurement of nanochannel internal resistance, R_c, under different Δc. When $\Delta c \gtrsim 0.2$, R_c is nearly constant, with little variation with Δc. Besides, we observed a power-law dependence of the internal resistance on the concentration difference. In comparison, an empirical power-law relation between R_c and Δc was previously reported with a 2D numerical simulation for a single charged nanochannel RED cell [128]:

$$R_c = A\Delta c^{-\alpha}, \tag{6.3}$$

where A and α are constants independent of Δc but could be dependent on other factors. In the numerical model compared [128], coupled, nonlinear equations, based on the Poisson equation and the conservation of mass, momentum, and charged species (i.e., the continuity, Navier-Stokes, and Nerst-Planck equations, respectively), are simulated to obtain electrical potential, flow velocity, ionic concentrations, and hence the resultant electrical outputs. Although different configurations of charged interfaces used here, our case of the RED experiment using the Nafion nano-porous membrane shows such a power-law relation of R_c, given in Eq. (6.3), with the pre-factor 0.15 and the power-law scaling $\alpha = 0.23$.

To explain such power-law relation observed for our experimental membrane cell, one could approximate the nano-porous, CEM membrane as bundle of charged nanochannels parallel to each other. To a first order approximation, for N number of parallel nano-channels (each with internal electrical resistance R_i) the effective electric resistance R_{eff} could be estimated as N numbers of electrical resistors in parallel and, hence, $1/R_{\text{eff}} = \sum_i^N 1/R_i$, i.e., $R_{\text{eff}} \approx A\Delta c^{-\alpha}/N$, also exhibiting a power-law relation.

Shown in Fig. 6.5b is our further experimental investigation of the dependence of the open-circuit voltage, ϕ_0, on Δc, revealing a logarithmic dependence. The general trend shows that ϕ_0 is increased with Δc, as a larger Gibbs free energy of mixing is available to harness

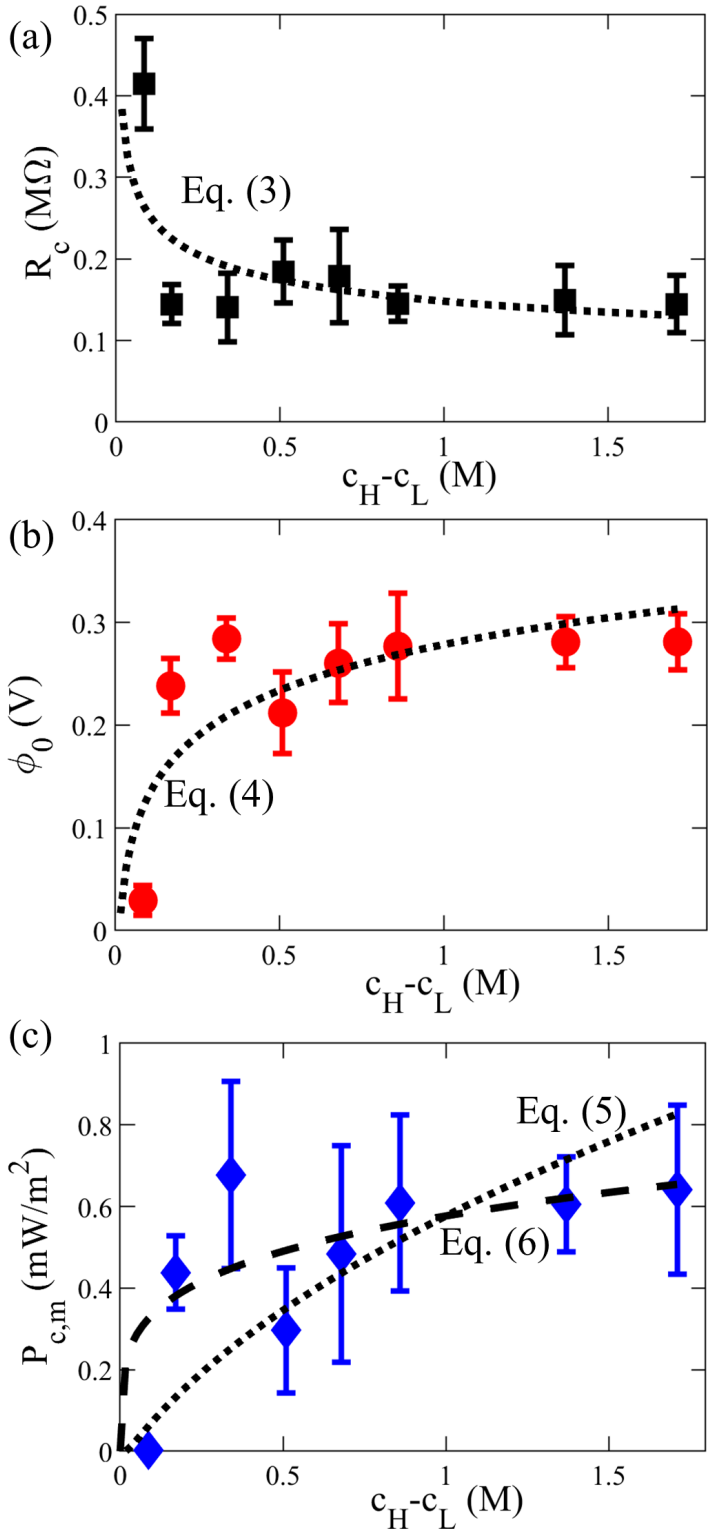

Figure 6.5: Variation of (a) internal resistance, R_c, (b) open-circuit voltage, ϕ_0, and (c) maximum power output density, $P_{c,m}$, with concentration difference, Δc (= $c_H - c_L$). The dotted lines in (a), (b) and (c) represent Eqs. (6.4), (6.3) and (6.5), respectively. The dashed line in (c) demonstrates the curve-fit using the simplified relation (6.6).

electricity. Intriguingly, such a logarithmic relation was also reported by the numerical simulation of a single charged nanochannel RED between the two reservoirs, with the following expression [128]:

$$\phi_0 = B \ln \Delta c + \beta, \tag{6.4}$$

where B and β are constants independent of Δc but may depend on other parameters, such as membrane type and geometry, which were not explored in the simulation [128]. Fitting our data with the logarithmic relation of Eq. (6.4), we found the best fitting results of $B = 0.065$ and $\beta = 0.28$, based on a least-square residual fitting method. Our experimental data shows that ϕ_0 can be approximated to a constant for a sufficiently large Δc, which is consistent with the logarithmic relation, Eq. (6.4) since $\phi_0 \approx \beta$ for large Δc.

Fig. 6.5c reveals how the maximum output power density, $P_{c,m}$, varies with Δc. Despite scattering of the data, the general tends can be consistently described by the above empirical relations found for R_c and ϕ_0 varying with Δc. Using Eqs. (6.3) and (6.4), one can obtain an empirical relation for $P_{c,m}$ from Eq. (6.1) [128]:

$$P_{c,m} = \frac{\phi_0^2}{4R_c}\frac{1}{A_c} = \frac{(B \ln \Delta c + \beta)^2}{4A\Delta c^{-\alpha}}\frac{1}{A_c}, \tag{6.5}$$

where α is the same theoretical exponent as in Eq. (6.3). Consistently, our experimental data of $P_{c,m}$ shown in Fig. 6.5c yields the best fitting result of $\alpha \approx 0.26$. Considering the approximation $\phi_0 \approx \beta$, this equation can be further simplified to:

$$P_{c,m} \approx C\Delta c^{\alpha}/A_c, \tag{6.6}$$

where C $(= \beta^2/4A) = 0.131$. The maximum power output density, $P_{c,m}$, was observed to remain in the range of 0.4 to 0.6 mW/m^2 with change in Δc between 0.51 and 1.71 mM. In comparison, other experiments have reported a power density $P_{c,m} \approx 0.5$ W/m^2 using 10 units of commercial ion-exchange membranes, such as Ralex, Neosepta, and Fujifilm (e.g., Fig. 4 by Vermaas et al. [230]), and a maximum power output $P'_{c,m} \approx 1$ μW (e.g., Fig. 10 by Chein et al. [102]) from a single cell RED design using a charged alumina membrane under $c_H/c_L = 1000$ with $c_L = 10^{-4}$ M.

6.4 Conclusion

A RED power generation unit was designed, consisting of two reservoirs separated by a cation-selective Nafion membrane. Solutions of different salt concentration flow through the reservoirs, establishing a concentration gradient across the nanoporous membrane. Exploiting the membrane charge-selectivity and electro-migration of ions, this setup generates electricity by harnessing renewable salinity gradient energy. In the present study, we analyzed the effect of concentration difference and flow rate on the RED electrical I-V characteristic. On one hand, the inflow rate—varied over three order of magnitudes—shows an insignificant impact of the RED electrical outputs. This may be explained by the dominance of diffusive transport over advection in the low Peclet number nature for the RED cell exploiting nanoporous CEM membrane. On the other hand, the experimental data show that both internal resistance (R_c) and maximum power density ($P_{c,m}$) demonstrates a power-law dependence on concentration difference, whereas open-circuit voltage (ϕ_0) shows a logarithmic dependence. Both the power-law and logarithmic dependence on Δc found with the experimental RED using a charged membrane are consistent with previous simulation results of the RED outputs using a charged nanochannel. These empirical relations of the electrical outputs depending on Δc can be useful for future designs of similar RED membrane cells. In terms of applications, experimentally when $\Delta c \gtrsim 0.2$ M, the change in open-circuit voltage with Δc was found to be negligible, implying an optimal operation for the RED membrane cell. Finally, consistent and robust renewable electricity generation with the open-circuit voltage of $\phi_0 = 0.23V$ was produced using a Nafion membrane RED cell using common salt solutions with $\Delta c \gtrsim 0.2$ M.

Chapter 7

Summary

This doctoral thesis reports the transport of ions through charged nano-confinements and its engineering applications in the area of renewable energy. More specifically, we perform detailed numerical investigations of diffusioosmotic flow and reverse electrodialysis using COMSOL Multiphysics. In addition, we carry out experimental study of reverse electrodialysis through appropriate electrical measurements in a fluidic cell designed using commercially available cation-selective Nafion membrane.

In Chapter 2, the numerical model was described in detail, focusing on the elaborate description of the simulation algorithm, error analysis, and model validation, including a detailed mesh independence study.

Investigation of diffusioosmotic flow in straight nanochannels nano-confinements is reported in Chapter 3. In this chapter, we discuss the variation in flow velocity magnitude and direction through a positively-charged nanochannel due to an external concentration gradient. We observe that the concentration difference across the nanochannel dictates the magnitude of diffusioosmotic velocity. In contrast, the flow direction inside the channels is not significantly affected by the concentration gradient, but by nanochannel parameters, such as nanochannel dimensions, and surface charge. Based on a comparative analysis of electroosmotic, and chemiosmotic components of diffusioosmositic flow, we, henceforth, reported a non-dimensional number based on the nanochannel properties and dimensions that can

predict the flow direction inside the charged nanochannel.

In Chapter 4, we extend the investigation of diffusioosmotic flow to a charged, tapered nanochannel. In this analysis, we find that the taper angle in a nanochannel of linearly varying height plays a very crucial role in the diffusioosmotic flow, whereas the location of the nanochannel tip predominantly dictated the nanoflow direction. Fluid motion, in this case, is always directed from the nanochannel tip (i.e., the location of minimum channel height) to the base. This observation is due to a stronger overlap of EDL near the smaller orifice, increasing the overall anion concentration, hence causing higher chemiosmotic flow. We further report that the flow rate of inflowing solutions in the reservoirs did not play a significant role in the flow characteristics of diffusioosmosis in the low Peclet number regime.

Fluid transport through charged nanofluidic setups has been exploited in various engineering applications, such as water desalination, power generation, DNA segmentation, and chromatography. In this doctoral research, we investigated the generation of renewable energy by providing an external concentration gradient of flowing electrolytes across a charged ion-selective membrane. This process of power generation is known as reverse electrodialysis. Chapter 5 discusses the electrical characteristics and the effect of a flow rate of a reverse electrodialysis cell with a single positively-charged nanochannel. The nanochannel is connected to two reservoirs on either side, where solutions of different concentrations flow. The power output due to the combined effect of surface charge, concentration gradient, and local electric fields is analyzed through the conservation of mass, momentum, energy, and chemical species. Our numerical simulations results report a power-law dependence of internal resistance of the RED cell, and a logarithmic dependence of open-circuit voltage on on external concentration difference, Δc. By varying several control parameters systematically, we revealed that the maximum power output of the reverse electrodialysis cell requires smaller nanochannel height, optimal nanochannel length, more significant diffusion coefficient, and higher flow rate.

Finally, in Chapter 6, we illustrate the possibility of renewable energy generation through reverse electrodialysis using a cation-selective Nafion membrane. In our experimental setup, solutions of different concentration flow through two reservoirs at a constant rate. Any form of interaction in the reservoirs can occur only via the charged ion-selective Nafion membrane,

and the power output is recorded through the electrodes. Here, the average power output density and open-circuit voltage were found to be 0.5 mW/m^2 and 0.23 V, respectively, for low Peclet number flow. In a qualitative agreement with our numerical simulation results, RED cell internal resistance, and open-circuit voltage demonstrated an exponential, and logarithmic dependence on Δc, respectively. The present experiments using Nafion membrane performed for input flow rates, varied over 3 orders of magnitude in the low Peclet number regime, did not show any notable effect on the electrical characteristics of the RED cell.

In conclusion, the present doctoral dissertation provides an in-depth insight into diffusioosmotic flow and reports a procedure to empirically predict the flow direction through nanochannels, based on the nanochannel characteristics. Applications of such flows for renewable energy generation through reverse electrodialysis were also explored in this thesis both experimentally and numerically.

7.1 Future work

The present research about nanofluidic transport was conducted for simple geometries and experimental setups with a single reverse electrodialysis cell. Further improvement can be made in both numerical and experimental fronts, some of which are listed below:

1. **Diffusioosmosis in hour-glass nanochannel** A good number of reports have studied diffusioosmosis in straight channels. However, not a significant amount of research has not been observed for tapered, or hourglass-shaped nanochannels. Due to ion current rectification and ion current polarization in tapered or hourglass-shaped nanochannels, these nano-confinements of varying height could be used in lab-on-a-chip devices for nanofluidic valves, and also provide a deeper understanding of ionic transport in biotic systems. While the study of diffusioosmotic flow in tapered nanochannel has been addressed in this doctoral research work, diffusioosmosis in hourglass-shaped nanochannels has not been explore here, and can be addressed to extend the present work.

2. **Numerical simulation with more than one nano-confinement:** Due to the huge complexity of modeling and computing multi-channel geometries, with three coupled governing equations, we performed the numerical simulations for a single nano-confinement in this project and also, in most of the numerical simulations in the literature. However, for more accurate simulations to mimic actual reverse electrodialysis cell designs, it is important to observe the contribution of multiple channels, and their interactions towards electrical characteristics. The investigation of electrical power output through multiple nano-confinements can be a significant step ahead in the area of numerical computation of the reverse electrodialysis process.

3. **Three-dimensional numerical investigation of reverse electrodialysis:** Our present numerical investigation of reverse electrodialysis is in a 2D geometry, assuming the effect of the z-direction is insignificant. Due to the absence of experiments on such small scale setups till date, this assumption has not been verified experimentally. Thus, the question of validity of the above assumption always remains, unless experimentally verified, or compared with a three-dimensional model. This necessitates the complete three-dimensional modeling of a reverse electrodialysis cell for verification of simplified numerical models. In addition, a detailed three-dimensional numerical model of such could provide a complete understanding of the process of reverse electrodialysis.

4. **Experimental study of reverse electrodialysis cell stack design:** Investigations of reverse electrodialysis stack design has been done for various AEM and CEM combinations. Meanwhile, the prospect of using a Nafion membrane as the CEM seems promising based on our experimental observations. Thus, in our quest for better power output, it is reasonable to attempt new AEM/CEM combinations (with Nafion membrane as the CEM), and investigate the electrical output from such configurations.

5. **Real-time experimental visualization of reverse electrodialysis** In so far, the research in the area of reverse electrodialysis has focused on the electrical output. Little exploration was done to visualize the pore-scale interaction and observe the flow inside nano-confinements. An interesting study in this area would be to experimen-

tally visualize the flow in micro/nano-scale to potentially quantify the analytical and numerical predictions, which could be achieved through experiments with transparent reservoirs performed under high magnification microscopes. Such small-scale visualization, if achieved, would immensely benefit our understanding of the fluid and ionic interactions.

References

[1] COMSOL AB, Stockholm, Sweden. *COMSOL Multiphysics User's Guide*, 2017.

[2] D. Burgreen and F .R. Nakache. Capillary Slits'. *J . Phys. Chem.*, 68:1084–1091, 1964.

[3] Peter Pivonka and D. Smith. Investigation of nanoscale electrohydrodynamic transport phenomena in charged porous materials. *Int. J. Numer. Methods Eng.*, 63(14):1975–1990, 2005.

[4] Dong Kwon Kim. Numerical study of power generation by reverse electrodialysis in ion-selective nanochannels. *J. Mech. Sci. Technol.*, 25(1):5–10, 2011.

[5] Byeong Dong Kang, Hyun Jung Kim, Moon Gu Lee, and Dong-Kwon Kim. Numerical study on energy harvesting from concentration gradient by reverse electrodialysis in anodic alumina nanopores. *Energy*, 86:525–538, 2015.

[6] Béatrice Balannec, Aziz Ghoufi, and Anthony Szymczyk. Nanofiltration performance of conical and hourglass nanopores. *J. Membr. Sci.*, 552:336 – 340, 2018.

[7] Leon Rosentsvit, Wei Wang, Jarrod Schiffbauer, Hsueh-Chia Chang, and Gilad Yossifon. Ion current rectification in funnel-shaped nanochannels: Hysteresis and inversion effects. *J. Chem. Phys.*, 143(22):224706, 2015.

[8] Lydéric Bocquet and Patrick Tabeling. Physics and technological aspects of nanofluidics. *Lab Chip*, 14(17):3143, June 2014.

[9] Yong Chen and Anne Pepin. Nanofabrication: Conventional and nonconventional methods. *Electrophoresis*, 22(2):187–207, 2001.

[10] Geoffrey A Ozin, Kun Hou, Bettina V Lotsch, Ludovico Cademartiri, Daniel P Puzzo, Francesco Scotognella, Arya Ghadimi, and Jordan Thomson. Nanofabrication by self-assembly. *Materials Today*, 12(5):12–23, 2009.

[11] Stephen Y Chou, Peter R Krauss, and Preston J Renstrom. Nanoimprint lithography. *Journal of Vacuum Science & Technology B: Microelectronics and Nanometer Structures Processing, Measurement, and Phenomena*, 14(6):4129–4133, 1996.

[12] Kathryn Wilder, Calvin F Quate, Bhanwar Singh, and David F Kyser. Electron beam and scanning probe lithography: A comparison. *Journal of Vacuum Science & Technology B: Microelectronics and Nanometer Structures Processing, Measurement, and Phenomena*, 16(6):3864–3873, 1998.

[13] Manuel G Velarde. Drops, liquid layers and the marangoni effect. *Philosophical Transactions of the Royal Society of London. Series A: Mathematical, Physical and Engineering Sciences*, 356(1739):829–844, 1998.

[14] Peichun Amy Tsai. Slippery interfaces for drag reduction. *Journal of fluid mechanics*, 736:1–4, 2013.

[15] P-F Hao, Catherine Wong, Z-H Yao, and K-Q Zhu. Laminar drag reduction in hydrophobic microchannels. *Chemical Engineering & Technology: Industrial Chemistry-Plant Equipment-Process Engineering-Biotechnology*, 32(6):912–918, 2009.

[16] Xi Zhang, Feng Shi, Jia Niu, Yugui Jiang, and Zhiqiang Wang. Superhydrophobic surfaces: from structural control to functional application. *Journal of Materials Chemistry*, 18(6):621–633, 2008.

[17] S Farhadi, M Farzaneh, and SA Kulinich. Anti-icing performance of superhydrophobic surfaces. *Applied Surface Science*, 257(14):6264–6269, 2011.

[18] Joost W Van Honschoten, Nataliya Brunets, and Niels R Tas. Capillarity at the nanoscale. *Chemical Society Reviews*, 39(3):1096–1114, 2010.

[19] GN Peggs. A review of the fundamental methods for measuring gauge pressures up to 1 kpa. *Journal of Physics E: Scientific Instruments*, 13(12):1254, 1980.

[20] Bo Zhang, Edmund T Bergstroem, David M Goodall, and Peter Myers. Capillary action liquid chromatography. *Journal of separation science*, 32(11):1831–1837, 2009.

[21] Mark Denny. Tree hydraulics: how sap rises. *European Journal of Physics*, 33(1):43, 2011.

[22] Kahp Y Suh, Yun S Kim, and Hong H Lee. Capillary force lithography. *Advanced Materials*, 13(18):1386–1389, 2001.

[23] Zdenek Slouka, Satyajyoti Senapati, and Hsueh-Chia Chang. Microfluidic Systems with Ion-Selective Membranes. *Annu. Rev. Anal. Chem.*, 7:317–335, 2014.

[24] R.J. Hunter. *Zeta Potential in Colloid Science: Principles and Applications*. Academic Press, 1981.

[25] Stefan Howorka and Zuzanna Siwy. Nanopore analytics: sensing of single molecules. *Chemical Society Reviews*, 38(8):2360–2384, 2009.

[26] Antonio Ramos, Hywel Morgan, Nicolas G Green, and A Castellanos. Ac electrokinetics: a review of forces in microelectrode structures. *Journal of Physics D: Applied Physics*, 31(18):2338, 1998.

[27] W Sparreboom, A van den Berg, and J C T Eijkel. Transport in nanofluidic systems: a review of theory and applications. *New Journal of Physics*, 12(1):015004, 2010.

[28] Frank HJ van der Heyden, Douwe Jan Bonthuis, Derek Stein, Christine Meyer, and Cees Dekker. Power generation by pressure-driven transport of ions in nanofluidic channels. *Nano letters*, 7(4):1022–1025, 2007.

[29] Yongqiang Ren and Derek Stein. Slip-enhanced electrokinetic energy conversion in nanofluidic channels. *Nanotechnology*, 19(19):195707, 2008.

[30] Derek Stein, Frank HJ van der Heyden, Wiepke JA Koopmans, and Cees Dekker. Pressure-driven transport of confined dna polymers in fluidic channels. *Proceedings of the National Academy of Sciences*, 103(43):15853–15858, 2006.

[31] Mainak Majumder, Nitin Chopra, Rodney Andrews, and Bruce J Hinds. Nanoscale hydrodynamics: enhanced flow in carbon nanotubes. *Nature*, 438(7064):44, 2005.

[32] Xiangchun Xuan and Dongqing Li. Solute separation in nanofluidic channels: Pressure-driven or electric field-driven? *Electrophoresis*, 28(4):627–634, 2007.

[33] G.K. Batchelor. *An introduction to fluid dynamics*. Cambridge university press, 2000.

[34] Reto B. Schoch, Jongyoon Han, and Philippe Renaud. Transport phenomena in nanofluidics. *Rev. Mod. Phys.*, 80:839–883, 2008.

[35] J Dainty, PC Croghan, and DS Fensom. Electro-osmosis, with some applications to plant physiology. *Canadian Journal of Botany*, 41(6):953–966, 1963.

[36] M Iwata, T Tanaka, and MS Jami. Application of electroosmosis for sludge dewatering—a review. *Drying Technology*, 31(2):170–184, 2013.

[37] Shulin Zeng, Chuan-Hua Chen, James C Mikkelsen Jr, and Juan G Santiago. Fabrication and characterization of electroosmotic micropumps. *Sensors and Actuators B: Chemical*, 79(2-3):107–114, 2001.

[38] S S Dukhin. Non-Equilibrium Electric Surface Phenomena. *Adv. Colloid an.d Interface Sci.*, 44:1–134, 1993.

[39] Armand Ajdari and Jacques Prost. Free-flow electrophoresis with trapping by a transverse inhomogeneous field. *Proceedings of the National Academy of Sciences*, 88(10):4468–4471, 1991.

[40] Zaifang Zhu, Joann J Lu, and Shaorong Liu. Protein separation by capillary gel electrophoresis: a review. *Analytica chimica acta*, 709:21–31, 2012.

[41] Paul H Johnson and Lawrence I Grossman. Electrophoresis of dna in agarose gels. optimizing separations of conformational isomers of double-and single-stranded dnas. *Biochemistry*, 16(19):4217–4225, 1977.

[42] Vratislav Kostal and Edgar A Arriaga. Recent advances in the analysis of biological particles by capillary electrophoresis. *Electrophoresis*, 29(12):2578–2586, 2008.

[43] Hermann Schägger and Gebhard Von Jagow. Tricine-sodium dodecyl sulfate-polyacrylamide gel electrophoresis for the separation of proteins in the range from 1 to 100 kda. *Analytical biochemistry*, 166(2):368–379, 1987.

[44] Ryan T Turgeon and Michael T Bowser. Micro free-flow electrophoresis: theory and applications. *Analytical and bioanalytical chemistry*, 394(1):187–198, 2009.

[45] Huan J. Keh and Li Y. Hsu. Diffusioosmosis of electrolyte solutions in fibrous porous media. *Microfluid. Nanofluidics*, 5(3):347–356, 2008.

[46] Ankur Gupta, Bhargav Rallabandi, and Howard A. Stone. Diffusiophoretic and diffusioosmotic velocities for mixtures of valence-asymmetric electrolytes. *Phys. Rev. Fluids*, 4:043702, Apr 2019.

[47] Dennis C. Prieve. Migration of a colloidal particle in a gradient of electrolyte concentration. *Adv. Colloid Interface Sci.*, 16(1):321–335, 1982.

[48] Simon Gravelle. *Nanofluidics: a theoretical and numerical investigation of fluid transport in nanochannels*. Phd thesis, University of Lyon, 2015.

[49] D. C. Prieve, J. L. Anderson, J. P. Ebel, and M. E. Lowell. Motion of a particle generated by chemical gradients. Part 2. Electrolytes. *J. Fluid Mech.*, 148:247–269, 1984.

[50] Sangwoo Shin, Patrick B Warren, and Howard A Stone. Cleaning by surfactant gradients: Particulate removal from porous materials and the significance of rinsing in laundry detergency. *Physical Review Applied*, 9(3):034012, 2018.

[51] PJ Whitmore. Thermo-and diffusiophoresis for small aerosol particles. *Journal of Aerosol Science*, 12(1):1–9, 1981.

[52] AS Dukhin, ZR Ulberg, VI Karamushka, and TG Gruzina. Peculiarities of live cells' interaction with micro-and nanoparticles. *Advances in colloid and interface science*, 159(1):60–71, 2010.

[53] Dennis C Prieve, Stephanie M Malone, Aditya S Khair, Robert F Stout, and Mazen Y Kanj. Diffusiophoresis of charged colloidal particles in the limit of very high salinity. *Proceedings of the National Academy of Sciences*, 116(37):18257–18262, 2019.

[54] Darrell Velegol, Astha Garg, Rajarshi Guha, Abhishek Kar, and Manish Kumar. Origins of concentration gradients for diffusiophoresis. *Soft matter*, 12(21):4686–4703, 2016.

[55] Lydéric Bocquet and Elisabeth Charlaix. Nanofluidics, from bulk to interfaces. *Chem. Soc. Rev.*, 39:1073–1095, 2010.

[56] V María Barragán and Signe Kjelstrup. Thermo-osmosis in membrane systems: a review. *Journal of Non-Equilibrium Thermodynamics*, 42(3):217–236, 2017.

[57] Anthony P Straub, Ngai Yin Yip, Shihong Lin, Jongho Lee, and Menachem Elimelech. Harvesting low-grade heat energy using thermo-osmotic vapour transport through nanoporous membranes. *Nature Energy*, 1(7):16090, 2016.

[58] Harvey A Zambrano, Jens H Walther, Petros Koumoutsakos, and Ivo F Sbalzarini. Thermophoretic motion of water nanodroplets confined inside carbon nanotubes. *Nano letters*, 9(1):66–71, 2008.

[59] Rakesh Rajegowda, Sridhar Kumar Kannam, Remco Hartkamp, and Sarith P Sathian. Thermophoretic transport of ionic liquid droplets in carbon nanotubes. *Nanotechnology*, 28(15):155401, 2017.

[60] Christoph J Wienken, Philipp Baaske, Ulrich Rothbauer, Dieter Braun, and Stefan Duhr. Protein-binding assays in biological liquids using microscale thermophoresis. *Nature communications*, 1:100, 2010.

[61] Philipp Reineck, Christoph J Wienken, and Dieter Braun. Thermophoresis of single stranded dna. *Electrophoresis*, 31(2):279–286, 2010.

[62] Gunther E Molau. Heterogeneous ion-exchange membranes. *Journal of Membrane Science*, 8(3):309–330, 1981.

[63] Tao Luo, Said Abdu, and Matthias Wessling. Selectivity of ion exchange membranes: A review. *Journal of membrane science*, 555:429–454, 2018.

[64] Michael A Hickner, Andrew M Herring, and E Bryan Coughlin. Anion exchange membranes: Current status and moving forward. *Journal of Polymer Science Part B: Polymer Physics*, 51(24):1727–1735, 2013.

[65] Ronald F. Probstein. *Physicochemical hydrodynamics : An Introduction*. Butterworths Publishers, 1989.

[66] Anna Lee, Jeffrey W Elam, and Seth B Darling. Membrane materials for water purification: design, development, and application. *Environmental Science: Water Research & Technology*, 2(1):17–42, 2016.

[67] Ying Mei and Chuyang Y. Tang. Recent developments and future perspectives of reverse electrodialysis technology: A review. *Desalination*, 425:156–174, 2018.

[68] Shaurya Prakash, Aigars Piruska, Enid N Gatimu, Paul W Bohn, Jonathan V Sweedler, and Mark A Shannon. Nanofluidics: systems and applications. *IEEE Sensors Journal*, 8(5):441–450, 2008.

[69] BL Pangarkar, SK Deshmukh, VS Sapkal, and RS Sapkal. Review of membrane distillation process for water purification. *Desalination and Water Treatment*, 57(7):2959–2981, 2016.

[70] Vijay Kumar Thakur and Stefan Ioan Voicu. Recent advances in cellulose and chitosan based membranes for water purification: a concise review. *Carbohydrate polymers*, 146:148–165, 2016.

[71] Lindsey Grant. When will the oil run out? *Science*, 309(5731):52–54, 2005.

[72] S. Mekhilef, R. Saidur, and A. Safari. A review on solar energy use in industries. *Renewable and Sustainable Energy Reviews*, 15(4):1777 – 1790, 2011.

[73] Gang Li, Rui Zhu, and Yang Yang. Polymer solar cells. *Nature photonics*, 6(3):153, 2012.

[74] John K Kaldellis and Dimitris Zafirakis. The wind energy (r) evolution: A short review of a long history. *Renewable energy*, 36(7):1887–1901, 2011.

[75] G.M. Joselin Herbert, S. Iniyan, E. Sreevalsan, and S. Rajapandian. A review of wind energy technologies. *Renewable and Sustainable Energy Reviews*, 11(6):1117 – 1145, 2007.

[76] Annamalai Kirubakaran, Shailendra Jain, and RK Nema. A review on fuel cell technologies and power electronic interface. *Renewable and Sustainable Energy Reviews*, 13(9):2430–2440, 2009.

[77] G D Mehta. Performance of present-day ion-exchange membranes for power generation using a saturated solar pond. *J. Memb. Sci.*, 11:107–120, 1982.

[78] J. E. O'Connor, J. J. Duda, and G. E. Grant. 1000 dams down and counting. *Science*, 348(6234):496–497, 2015.

[79] Emilio F. Moran, Maria Claudia Lopez, Nathan Moore, Norbert Müller, and David W. Hyndman. Sustainable hydropower in the 21st century. *Proceedings of the National Academy of Sciences*, 115(47):11891–11898, 2018.

[80] Jin Gi Hong, Bopeng Zhang, Shira Glabman, Nigmet Uzal, Xiaomin Dou, Hongguo Zhang, Xiuzhen Wei, and Yongsheng Chen. Potential ion exchange membranes and system performance in reverse electrodialysis for power generation: A review. *J. Memb. Sci*, 486:71–88, 2015.

[81] R. E. Pattle. Production of electric power by mixing fresh and salt water in the hydroelectric pile. *Nature*, 174:660, 1954.

[82] R. J. Gross and J. F. Osterle. Membrane transport characteristics of ultrafine capillaries. *J. Chem. Phys.*, 49:228–234, 1968.

[83] J. C. Fair and J. F. Osterle. Reverse Electrodialysis in Charged Capillary Membranes. *J. Chem. Phys.*, 54(1971):3307, 1971.

[84] David A. Vermaas, Enver Guler, Michel Saakes, and Kitty Nijmeijer. Theoretical power density from salinity gradients using reverse electrodialysis. *Energy Procedia*, 20:170–184, 2012.

[85] David A. Vermaas, Joost Veerman, Ngai Yin Yip, Menachem Elimelech, Michel Saakes, and Kitty Nijmeijer. High efficiency in energy generation from salinity gradients with reverse electrodialysis. *ACS Sustainable Chem. Eng.*, 1(10), 2013.

[86] M. Turek and B. Bandura. Renewable energy by reverse electrodialysis. *Desalination*, 205(1-3):67–74, 2007.

[87] F. Suda, T. Matsuo, and D. Ushioda. Transient changes in the power output from the concentration difference cell (dialytic battery) between seawater and river water. *Energy*, 32(3):165–173, 2007.

[88] Jan W. Post, Hubertus V. M. Hamelers, and Cees J. N. Buisman. Energy recovery from controlled mixing salt and fresh water with a reverse electrodialysis system. *Environ. Sci. and Tech.*, 42(15):5785–5790, 2008.

[89] A. H. Galama, D. A. Vermaas, J. Veerman, M. Saakes, H. H M Rijnaarts, J. W. Post, and K. Nijmeijer. Membrane resistance: The effect of salinity gradients over a cation exchange membrane. *J. Membrane Sci.*, 467:279–291, 2014.

[90] J W Post, C H Goeting, J Valk, S Goinga, J Veerman, H V M Hamelers, and P J F M Hack. Towards implementation of reverse electrodialysis for power generation from salinity gradients. *Desalin. Water Treat.*, 16:182–193, 2010.

[91] Adam M. Weiner, Ronan K. McGovern, and John H. Lienhard V. A new reverse electrodialysis design strategy which signifi cantly reduces the levelized cost of electricity. *J. Memb. Sci.*, 493:605–614, 2015.

[92] Jin Gi Hong and Yongsheng Chen. Nanocomposite reverse electrodialysis (red) ion-exchange membranes for salinity gradient power generation. *J. Memb Sci.*, 460:139–147, 2014.

[93] Bopeng Zhang, Haiping Gao, and Yongsheng Chen. Enhanced ionic conductivity and power generation using ion-exchange resin beads in a reverse-electrodialysis stack. *Environ. Sci. Technol*, 49:14717–14724, 2015.

[94] Hoe-In Jeong, Hyun Jung Kim, and Dong-Kwon Kim. Numerical analysis of transport phenomena in reverse electrodialysis for system design and optimization. *Energy*, 68:229–237, 2014.

[95] Ramin Banan Sadeghian, Oxana Pantchenko, Daniel Tate, and Ali Shakouri. Miniaturized concentration cells for small-scale energy harvesting based on reverse electrodialysis. *Appl. Phys. Lett.*, 99:173702, 2011.

[96] Anders Bentien, Tatsuhiro Okada, and Signe Kjelstrup. Evaluation of nanoporous polymer membranes for electrokinetic energy conversion in power applications. *The Journal of Physical Chemistry C*, 117(4):1582–1588, 2013.

[97] Sofie Haldrup, Jacopo Catalano, Mogens Hinge, Grethe V. Jensen, Jan S. Pedersen, and Anders Bentien. Tailoring membrane nanostructure and charge density for high electrokinetic energy conversion efficiency. *ACS Nano*, 10(2):2415–2423, 2016.

[98] Dong-Kwon Kim, Chuanhua Duan, Yu-Feng Chen, and Arun Majumdar. Power generation from concentration gradient by reverse electrodialysis in ion-selective nanochannels. *Microfluid. Nanofluidics*, 9:1215–1224, 2010.

[99] Dong-Kwon Kim, Duckjong Kim, Sung Jin Kim, and Sang-Jin Park. Effect of ionic mobility of working electrolyte on electrokinetic energy conversion in sub-micron channels. *International Journal of Thermal Sciences*, 49(7):1128 – 1132, 2010.

[100] Sang Woo Lee, Hyun Jung Kim, and Dong-Kwon Kim. Power generation from concentration gradient by reverse electrodialysis in dense silica membranes for microfluidic and nanofluidic systems. *Energies*, 9(1), 2016.

[101] M Marino, L Misuri, A Carati, and D Brogioli. Boosting the voltage of a salinity-gradient-power electrochemical cell by means of complex-forming solutions. *Appl. Phys. Lett.*, 105:033901, 2014.

[102] Reiyu Chein and Boyan Liu. Energy conversion from electrolyte concentration gradient using charged nano-pores. *Int. J. Green Energy*, 13:1400–1411, 2017.

[103] Bjørn Sjøgren Kilsgaard, Sofie Haldrup, Jacopo Catalano, and Anders Bentien. High figure of merit for electrokinetic energy conversion in nafion membranes. *Journal of Power Sources*, 247:235 – 242, 2014.

[104] Jacopo Catalano and Anders Bentien. Influence of temperature on the electrokinetic properties and power generation efficiency of nafion® 117 membranes. *Journal of Power Sources*, 262:192 – 200, 2014.

[105] Jan Willem Post. *Blue Energy: electricity production from salinity gradients by reverse electrodialysis*. PhD thesis, 2009.

[106] B Muhthassim, XK Thian, and KN Md Hasan. Energy harvesting from salinity gradient. In *IOP Conference Series: Earth and Environmental Science*, volume 140, page 012045, 2018.

[107] J Sonnefeld, A Gobel, and W Vogelsberger. Surface charge density on spherical silica particles in aqueous alkali chloride solutions Part 1. Experimental results. *Colloid Polym. Sci.*, 273:926–931, 1995.

[108] J. Sonnefeld. Surface charge density on spherical silica particles in aqueous alkali chloride solutions Part 2. Evaluation of the surface charge density constants. *Colloid Polym. Sci.*, 273:932–938, 1995.

[109] Christopher D. F. Honig and William A. Ducker. Squeeze film lubrication in silicone oil: Experimental test of the no-slip boundary condition at solid−liquid interfaces. *The Journal of Physical Chemistry C*, 112(44):17324–17330, 2008.

[110] *MUltifrontal Massively Parallel Solver (MUMPS 5.1.2) Users' Guide*, 2017.

[111] Hirofumi Daiguji. Ion transport in nanofluidic channels. *Chem. Soc. Rev.*, 39:901–911, 2010.

[112] C. L. Rice and R. Whitehead. Electrokinetic flow in a narrow cylindrical capillary. *J. Phys.Chem.*, 69:4017–4024, 1965.

[113] David C. Grahame. The electrical double layer and the theory of electrocapillarity. *Chemical Reviews*, 41(3):441–501, 1947.

[114] Jacob H Masliyah and Subir Bhattacharjee. *Electrokinetic and colloid transport phenomena*. John Wiley & Sons, 2006.

[115] G.B. Westermann-Clark and C.C. Christoforou. The exclusion-diffusion potential in charged porous membranes. *J. Electroanal. Chem. Interfacial Electrochem.*, 198(2):213 – 231, 1986.

[116] Byron D. Gates, Qiaobing Xu, Michael Stewart, Declan Ryan, C. Grant Willson, and George M. Whitesides. New approaches to nanofabrication: Molding, printing, and other techniques. *Chem. Rev.*, 105(4):1171–1196, 2005.

[117] Zdenek Slouka, Satyajyoti Senapati, and Hsueh-Chia Chang. Microfluidic Systems with Ion-Selective Membranes. *Annu. Rev. Anal. Chem.*, 7:317–335, 2014.

[118] Ana Egatz-gomez, Ceming Wang, Flora Klacsmann, Zehao Pan, Steve Marczak, Yunshan Wang, Gongchen Sun, Satyajyoti Senapati, and Hsueh-Chia Chang. Future mi-

crofluidic and nanofluidic modular platforms for nucleic acid liquid biopsy in precision medicine. *Biomicrofluidics*, 10:032902, 2016.

[119] Yu Yan, Yunshan Wang, Satyajyoti Senapati, Jarrod Schiffbauer, Gilad Yossifon, and Hsueh Chia Chang. Robust ion current oscillations under a steady electric field: An ion channel analog. *Phys. Rev. E*, 94(2):1–6, 2016.

[120] Jan C T Eijkel and Albert Van Den Berg. Nanofluidics : what is it and what can we expect from it ? *Microfluid. Nanofluidics*, pages 249–267, 2005.

[121] B. V. Derjaguin, S. S. Dukhin, and M. M. Koptelova. Capillary osmosis through porous partitions and properties of boundary layers of solutions. *J. Colloid Interface Sci.*, 38(3):584–595, 1972.

[122] Daosheng Deng, E Victoria Dydek, Ji-hyung Han, Sven Schlumpberger, Boris Zaltzman, and Martin Z Bazant. Overlimiting Current and Shock Electrodialysis in Porous Media. *Langmuir*, pages 1–46, 2013.

[123] Sven Schlumpberger, Nancy B. Lu, Matthew Suss, and Martin Z. Bazant. Scalable and Continuous Water Deionization by Shock Electrodialysis. *Environ. Sci. Technol. Lett.*, pages 367–372, 2015.

[124] Sungmin Park, Yeonsu Jung, Seok Young Son, Inhee Cho, Youngrok Cho, Hyomin Lee, Ho-young Kim, and Sung Jae Kim. Capillarity ion concentration polarization as spontaneous desalting mechanism. *Nat. Commun.*, 7(May 2015):1–9, 2016.

[125] O V Hulko, B J Robinsin, and R N Kleiman. Fabrication of nanoscale single crystal InP membranes. *Appl. Phys. Lett.*, 91:053119, 2007.

[126] Frederick Gertz, Rustam Azimov, and Alexander Khitun. Biological cell positioning and spatially selective destruction via magnetic nanoparticles. *Appl. Phys. Lett.*, 101:013701, 2012.

[127] Su Hong Kwak, Seung-Ryong Kwon, Seol Baek, Seung-Min Lim, Young-Chang Joo, and Taek Dong Chung. Densely charged polyelectrolyte-stuffed nanochannel arrays for power generation from salinity gradient. *Sci. Rep.*, 6:26416, 2016.

[128] Sourayon Chanda and Peichun Amy Tsai. Numerical simulation of renewable power generation using reverse electrodialysis. *Energy*, 176:531 – 543, 2019.

[129] Jordi Moreno, Simon Grasman, Ronny van Engelen, and Kitty Nijmeijer. Upscaling reverse electrodialysis. *Environmental Science & Technology*, 52(18):10856–10863, 2018.

[130] Hong-Ren Jiang, Natsuhiko Yoshinaga, and Masaki Sano. Active motion of a janus particle by self-thermophoresis in a defocused laser beam. *Phys. Rev. Lett.*, 105:268302, Dec 2010.

[131] Mojtaba Taghipoor, Arnaud Bertsch, and Philippe Renaud. Thermal control of ionic transport and fluid flow in nanofluidic channels. *Nanoscale*, 7(44):18799–18804, 2015.

[132] P. B. Umbanhowar, V. Prasad, and D. A. Weitz. Monodisperse emulsion generation via drop break off in a coflowing stream. *Langmuir*, 16(2):347–351, 2000.

[133] Chirodeep Bakli and Suman Chakraborty. Capillary filling dynamics of water in nanopores. *Appl. Phys. Lett.*, 101:153112, 2012.

[134] Hsueh-Chia Chang, Gilad Yossifon, and Evgeny A Demekhin. Nanoscale Electrokinetics and Microvortices : How Microhydrodynamics Affects Nanofluidic Ion Flux. *Annu. Rev. Fluid Mech.*, 44:421–426, 2012.

[135] Huan J. Keh and Li Y. Hsu. Diffusioosmotic flow of electrolyte solutions in fibrous porous media at arbitrary zeta potential and double-layer thickness. *Microfluid. Nanofluidics*, 7(6):773, Apr 2009.

[136] Huan J. Keh and Yeu K. Wei. Osmosis through a fibrous medium caused by transverse electrolyte concentration gradients. *Langmuir*, 18(26):10475–10485, 2002.

[137] Huan J. Keh and Hsien Chen Ma. Diffusioosmosis of electrolyte solutions along a charged plane wall. *Langmuir*, 21(12):5461–5467, 2005.

[138] Vahid Hoshyargar, Seyed Nezameddin Ashrafizadeh, and Arman Sadeghi. Diffusioosmotic flow in rectangular microchannels. *Electrophoresis*, 37(5-6):809–817, 2016.

[139] Wu, Jan H. and Huan J. Keh. Diffusioosmosis and electroosmosis in a capillary slit with surface charge layers. *Colloids Surfaces A Physicochem. Eng. Asp.*, 212:27–42, 2003.

[140] Vahid Hoshyargar, Arman Sadeghi, and Seyed Nezameddin Ashrafizadeh. Bounded amplification of diffusioosmosis utilizing hydrophobicity. *RSC Adv.*, 6(55):49517–49526, 2016.

[141] Vahid Hoshyargar, Seyed Nezameddin Ashrafizadeh, and Arman Sadeghi. Mass transport characteristics of diffusioosmosis: Potential applications for liquid phase transportation and separation. *Phys. Fluids*, 29(1), 2017.

[142] Huan J. Keh and Jan H. Wu. Electrokinetic flow in fine capillaries caused by gradients of electrolyte concentration. *Langmuir*, 17(14):4216–4222, 2001.

[143] H B Ma, C Wilson, B Borgmeyer, K Park, Q Yu, S U S Choi, and Murli Tirumala. Effect of nanofluid on the heat transport capability in an oscillating heat pipe. *Appl. Phys. Lett.*, 88:143116, 2006.

[144] David M. Huang, Cécile Cottin-Bizonne, Christophe Ybert, and Lydéric Bocquet. Ion-Specific Anomalous Electrokinetic Effects in Hydrophobic Nanochannels. *Phys. Rev. E*, 98:177801, 2007.

[145] David M. Huang, Cécile Cottin-Bizonne, Christophe Ybert, and Lydéric Bocquet. Massive Amplification of Surface-Induced Transport at Superhydrophobic Surfaces. *Phys. Rev. Lett.*, 101:064503, 2008.

[146] Inhee Cho, Wonseok Kim, Junsuk Kim, Ho-young Kim, Hyomin Lee, and Sung Jae Kim. Non-Negligible Diffusio-Osmosis Inside an Ion Concentration Polarization Layer. *Phys. Rev. Lett.*, 254501(June):1–5, 2016.

[147] Hyungkook Jeon, Horim Lee, Kwan Hyoung Kang, and Geunbae Lim. Ion concentration polarization-based continuous separation device using electrical repulsion in the depletion region. *Sci. Rep.*, 3:3483, 2013.

[148] Shizhi Qian, Biswajit Das, and Xiaobing Luo. Diffusioosmotic flows in slit nanochannels. *J. Colloid Interface Sci.*, 315:721–730, 2007.

[149] Kuan Liang Liu, Jyh Ping Hsu, and Shiojenn Tseng. Capillary osmosis in a charged nanopore connecting two large reservoirs. *Langmuir*, 29(30):9598–9603, 2013.

[150] Eunpyo Choi, Kilsung Kwon, Daejoong Kim, and Jungyul Park. Lab on a Chip. *Lab Chip*, 15:168–178, 2015.

[151] Daosheng Deng, Wassim Aouad, William A. Braff, Sven Schlumpberger, Matthew E. Suss, and Martin Z. Bazant. Water purification by shock electrodialysis: Deionization, filtration, separation, and disinfection. *Desalination*, 357:77–83, 2015.

[152] Kwang Seok Kim, Won Ryoo, Myung Suk Chun, and Gui Yung Chung. Simulation of enhanced power generation by reverse electrodialysis stack module in serial configuration. *Desalination*, 318:79–87, 2013.

[153] Robert J. Hunter. *Foundations of Colloid Science*. Oxford University Press, 2 edition, 2001.

[154] David J Griffiths. *Introduction to Electrodynamics*. Pearson, Boston, MA, 4th ed. edition, 2013.

[155] N Lakshminarayanaiah. Transport phenomena in artificial membranes. *Chem. Rev.*, 65(5):491–565, 1965.

[156] Yunus A. Cengel and John M. Cimbala. *Fluid Mechanics Fundamental and Applications*. McGraw-Hill Education, New York, NY, 4th ed edition, 2017.

[157] Yu Yan, Qian Sheng, Ceming Wang, Jianming Xue, and Hsueh-Chia Chang. Energy Conversion Efficiency of Nano fluidic Batteries: Hydrodynamic Slip and Access Resistance. *J. Phys. Chem. C*, 117:8050–8061, 2013.

[158] P B Peters, R Van Roij, M Z Bazant, and P M Biesheuvel. Analysis of electrolyte transport through charged nanopores. *Phys. Rev. E*, 93:053108, 2016.

[159] MM Kohonen, Nobuo Maeda, and HK Christenson. Kinetics of capillary condensation in a nanoscale pore. *Phys. Rev. Lett.*, 82(23):4667, 1999.

[160] Gang Bao. Mechanics of biomolecules. *J Mech. Phys. Solids*, 50(11):2237–2274, 2002.

[161] Shawn C. Owen and Molly S. Shoichet. Design of three-dimensional biomimetic scaffolds. *J. Biomed. Mater. Res. A*, 94A(4):1321–1331, 2010.

[162] Peter Rupprecht, Laurent Golé, Jean-Paul Rieu, Cyrille Vézy, Rosaria Ferrigno, Hichem C Mertani, and Charlotte Riviere. A tapered channel microfluidic device for comprehensive cell adhesion analysis, using measurements of detachment kinetics and shear stress-dependent motion. *Biomicrofluidics*, 6(1):014107, 2012.

[163] Attilio Marino, Carlo Filippeschi, Virgilio Mattoli, Barbara Mazzolai, and Gianni Ciofani. Biomimicry at the nanoscale: current research and perspectives of two-photon polymerization. *Nanoscale*, 7:2841–2850, 2015.

[164] Henry S. White and Andreas Bund. Ion current rectification at nanopores in glass membranes. *Langmuir*, 24(5):2212–2218, 2008.

[165] Haoyuan Jing and Siddhartha Das. Theory of diffusioosmosis in a charged nanochannel. *Phys. Chem. Chem. Phys.*, 20(15):10204–10212, 2018.

[166] Sourayon Chanda and Peichun Amy Tsai. Controlling diffusioosmotic flow. *Submitted*, 2019.

[167] David Feldmann, Salim R Maduar, Mark Santer, Nino Lomadze, Olga I Vinogradova, and Svetlana Santer. Manipulation of small particles at solid liquid interface: light driven diffusioosmosis. *Sci. Rep.*, 6:36443, 2016.

[168] Abhishek Kar, Tso-Yi Chiang, Isamar Ortiz Rivera, Ayusman Sen, and Darrell Velegol. Enhanced transport into and out of dead-end pores. *ACS Nano*, 9(1):746–753, 2015.

[169] Sangwoo Shin, Eujin Um, Benedikt Sabass, Jesse T Ault, Mohammad Rahimi, Patrick B Warren, and Howard A Stone. Size-dependent control of colloid transport via solute gradients in dead-end channels. *Proc. Natl. Acad. Sci.*, 113(2):257–261, 2016.

[170] Sangwoo Shin, Jesse T Ault, Jie Feng, Patrick B Warren, and Howard A Stone. Low-cost zeta potentiometry using solute gradients. *Adv. Mater.*, 29(30):1701516, 2017.

[171] Jesse T Ault, Sangwoo Shin, and Howard A Stone. Characterization of surface–solute interactions by diffusioosmosis. *Soft Matter*, 15(7):1582–1596, 2019.

[172] Juliette Experton, Xiaojian Wu, and Charles R. Martin. From ion current to electroosmotic flow rectification in asymmetric nanopore membranes. *Nanomaterials*, 7(12), 2017.

[173] Tongwen Xu. Development of bipolar membrane-based processes. *Desalination*, 140(3):247 – 258, 2001.

[174] Zuzanna S. Siwy and Stefan Howorka. Engineered voltage-responsive nanopores. *Chem. Soc. Rev.*, 39(3):1115–1132, 2010.

[175] Jingtao Wang, Minghui Zhang, Jin Zhai, and Lei Jiang. Theoretical simulation of the ion current rectification (icr) in nano-pores based on the poisson-nernst-planck (pnp) model. *Phys. Chem. Chem. Phys.*, 16:23–32, 2014.

[176] Chang Wei, Allen J. Bard, and Stephen W. Feldberg. Current rectification at quartz nanopipet electrodes. *Analytical Chemistry*, 69(22):4627–4633, 1997.

[177] Zuzanna Siwy, Elizabeth Heins, C. Chad Harrell, Punit Kohli, and Charles R. Martin. Conical-nanotube ion-current rectifiers: the role of surface charge. *Journal of the American Chemical Society*, 126(35):10850–10851, 2004.

[178] Zuzanna S. Siwy. Ion-current rectification in nanopores and nanotubes with broken symmetry. *Adv. Funct. Mater.*, 16(6):735–746, 2006.

[179] Trevor Gamble, Karl Decker, Timothy S. Plett, Matthew Pevarnik, Jan-Frederik Pietschmann, Ivan Vlassiouk, Aleksei Aksimentiev, and Zuzanna S. Siwy. Rectification of ion current in nanopores depends on the type of monovalent cations: Experiments and modeling. *The Journal of Physical Chemistry C*, 118(18):9809–9819, 2014.

[180] Ye Ai, Mingkan Zhang, Sang W. Joo, Marcos A. Cheney, and Shizhi Qian. Effects of electroosmotic flow on ionic current rectification in conical nanopores. *J. Phys. Chem. C*, 114(9):3883–3890, 2010.

[181] Shizhi Qian, Sang W. Joo, Ye Ai, Marcos A. Cheney, and Wensheng Hou. Effect of linear surface-charge non-uniformities on the electrokinetic ionic-current rectification in conical nanopores. *Journal of Colloid and Interface Science*, 329(2):376 – 383, 2009.

[182] Reiyu Chein and Bogan Chung. Numerical study of ionic current rectification through non-uniformly charged micro/nanochannel systems. *Journal of Applied Electrochemistry*, 43(12):1197–1206, Dec 2013.

[183] J.-F. Pietschmann, M.-T. Wolfram, M. Burger, C. Trautmann, G. Nguyen, M. Pevarnik, V. Bayer, and Z. Siwy. Rectification properties of conically shaped nanopores: consequences of miniaturization. *Phys. Chem. Chem. Phys.*, 15:16917–16926, 2013.

[184] Jyh-Ping Hsu, Yu-You Chu, Chih-Yuan Lin, and Shiojenn Tseng. Ion transport in a ph-regulated conical nanopore filled with a power-law fluid. *Journal of colloid and interface science*, 537:358–365, 2019.

[185] Jyh-Ping Hsu, Shu-Tuan Yang, Chih-Yuan Lin, and Shiojenn Tseng. Voltage-controlled ion transport and selectivity in a conical nanopore functionalized with ph-tunable polyelectrolyte brushes. *Journal of colloid and interface science*, 537:496–504, 2019.

[186] Jyh-Ping Hsu, Sheng-Chang Lin, Chih-Yuan Lin, and Shiojenn Tseng. Power generation by a ph-regulated conical nanopore through reverse electrodialysis. *Journal of Power Sources*, 366:169 – 177, 2017.

[187] Jyh-Ping Hsu, Shu-Tuan Yang, Chih-Yuan Lin, and Shiojenn Tseng. Ionic current rectification in a conical nanopore: Influences of electroosmotic flow and type of salt. *J. Phys. Chem. C*, 121(8):4576–4582, 2017.

[188] Jeffrey Moran and Jonathan Posner. Microswimmers with no moving parts. *Phys. Today*, 72(5):44–50, 2019.

[189] Ibrahim Dincer. Renewable energy and sustainable development: a crucial review. *Renewable and Sustainable Energy Reviews*, 4(2):157 – 175, 2000.

[190] M Z Jacobson. Review of solutions to global warming, air pollution, and energy security. *Energy Environ. Sci*, 2:148–173, 2009.

[191] Gang Li. Energy and exergy performance assessments for latent heat thermal energy storage systems. *Renewable and Sustainable Energy Reviews*, 51:926–954, 2015.

[192] Phebe Asantewaa Owusu and Samuel Asumadu-Sarkodie. A review of renewable energy sources, sustainability issues and climate change mitigation. *Cogent Engineering*, 3(1):1167990, 2016.

[193] M K Nazeeruddin, A Kay, I Rodicio, R Humphry-Baker, E Müller, P Liska, N Vlachopoulos, and M Grätzel. Conversion of Light to Electricity by *cis*-X_2-Bis ruthenium (II) Charge-Transfer Sensitizers on Nanocrystalline TiO_2 Electrodes. *J. Am. Chem. Soc*, 115:6382–6390, 1993.

[194] Aswani Yella, Hsuan-Wei Lee, Hoi Nok Tsao, Chenyi Yi, Aravind Kumar Chandiran, Md.Khaja Nazeeruddin, Eric Wei-Guang Diau, Chen-Yu Yeh, Shaik M Zakeeruddin,

and Michael Grätzel. Porphyrin-Sensitized Solar Cells with Cobalt (II/III)-Based Redox Electrolyte Exceed 12 Percent Efficiency. *Science*, 334:629–634, 2011.

[195] Thomas Ackermann. *Wind Power in Power Systems.* Wiley, 2005.

[196] Alison Bartle. Hydropower potential and development activities. *Energy Policy*, 30:1231–1239, 2002.

[197] Oliver Paish. Small hydro power: Technology and current status. *Renew. Sustain. Energy Rev.*, 6:537–556, 2002.

[198] P. Długołecki, K. Nymeijer, S. Metz, and M. Wessling. Current status of ion exchange membranes for power generation from salinity gradients. *J. Memb. Sci.*, 319:214–222, 2008.

[199] B.E. Logan and M. Elimelech. Membrane-based processes for sustainable power generation using water. *Nature*, 488:313–319, 2012.

[200] Olivier Schaetzle and Cees J.N. Buisman. Salinity gradient energy: Current state and new trends. *Engineering*, 1:164–166, 2015.

[201] Ahmet H. Avci, Ramato A. Tufa, Enrica Fontananova, Gianluca Di Profio, and Efrem Curcio. Reverse electrodialysis for energy production from natural river water and seawater. *Energy*, 165:512 – 521, 2018.

[202] Byeongdong Kang, Jaisuk Yoo, Hyun Jung Kim, and Dong-Kwon Kim. Slip-enhanced reverse electrodialytic power generation in ion-selective nanochannels. *Journal of Thermal Science*, 22(1):36–41, Feb 2013.

[203] Wonseok Kim, Sungmin Park, Kihong Kim, and Sung Jae Kim. Experimental verification of simultaneous desalting and molecular preconcentration by ion concentration polarization. *Lab Chip*, 17:3841–3850, 2017.

[204] Victor V. Nikonenko, Anna V. Kovalenko, Mahamet K. Urtenov, Natalia D. Pismenskaya, Jongyoon Han, Philippe Sistat, and Gérald Pourcelly. Desalination at overlimiting currents: State-of-the-art and perspectives. *Desalination*, 342:85 – 106, 2014.

[205] Jan W. Post, Joost Veerman, Hubertus V M Hamelers, Gerrit J W Euverink, Sybrand J. Metz, Kitty Nymeijer, and Cees J N Buisman. Salinity-gradient power: Evaluation of pressure-retarded osmosis and reverse electrodialysis. *J. Membrane Sci.*, 288(1-2):218–230, 2007.

[206] A. Dai and K.E. Trenberth. Estimates of freshwater discharge from continents: Latitudinal and seasonal variations. *J. Hydrometeorol*, 3:660–687, 2002.

[207] Y. Kobatake and H. Fujita. Flows through charged membranes. i. flip-flop current vs voltage relation. *J. Chem. Phys*, 40:2212–2218, 1964.

[208] M. Mao, J. D. Sherwood, and S. Ghosal. Electro-osmotic flow through a nanopore. *J. Fluid Mech.*, 749:167–183, 2014.

[209] Yuhui He, Zhuo Huang, Bowei Chen, Makusu Tsutsui, Xiang Shui Miao, and Masateru Taniguchi. Electrokinetic Analysis of Energy Harvest from Natural Salt Gradients in Nanochannels. *Sci. Rep.*, 7(1):1–15, 2017.

[210] Luigi Gurreri, Michele Ciofalo, Andrea Cipollina, Alessandro Tamburini, Willem Van Baak, and Giorgio Micale. CFD modelling of profiled-membrane channels for reverse electrodialysis. *Desalination and Water Treatment*, 3994(March 2015):1–20, 2014.

[211] Rui Long, Zhengfei Kuang, Zhichun Liu, and Wei Liu. Reverse electrodialysis in bilayer nanochannels: Salinity gradient-driven power generation. *Phys. Chem. Chem. Phys.*, 20(10):7295–7302, 2018.

[212] Amer Alizadeh and Moran Wang. Reverse electrodialysis through nanochannels with inhomogeneously charged surfaces and overlapped electric double layers. *J. Colloid Interface Sci.*, 529:214–223, 2018.

[213] Jacob Israelachvili. Solvation Forces and Liquid Structure, As Probed by Direct Force Measurements. *Acc. Chem. Res.*, 20:415–421, 1987.

[214] Zhijun Jia, Baoguo Wang, Shiqiang Song, and Yongsheng Fan. Blue energy: Current technologies for sustainable power generation from water salinity gradient. *Renewable and Sustainable Energy Reviews*, 31:91 – 100, 2014.

[215] Ngai Yin Yip and Menachem Elimelech. Performance limiting effects in power generation from salinity gradients by pressure retarded osmosis. *Environmental Science & Technology*, 45(23):10273–10282, 2011.

[216] Doriano Brogioli. Extracting renewable energy from a salinity difference using a capacitor. *Phys. Rev. Lett.*, 103:058501, 2009.

[217] Richard S. Norman. Water salination: A source of energy. *Science*, 186(4161):350–352, 1974.

[218] Rohit Karnik, Chuanhua Duan, Kenneth Castelino, Hirofumi Daiguji, and Arun Majumdar. Rectification of ionic current in a nanofluidic diode. *Nano Lett.*, 7(3):547–551, 2007.

[219] Juan Liu, Maksim Kvetny, Jingyu Feng, Dengchao Wang, Baohua Wu, Warren Brown, and Gangli Wang. Surface charge density determination of single conical nanopores based on normalized ion current rectification. *Langmuir*, 28(2):1588–1595, 2011.

[220] Anne M Benneker, Jeffery A Wood, Peichun A Tsai, and Rob GH Lammertink. Observation and experimental investigation of confinement effects on ion transport and electrokinetic flows at the microscale. *Sci. Rep.*, 6:37236, 2016.

[221] Anne M Benneker, Burcu Gumuscu, Ernest GH Derckx, Rob GH Lammertink, Jan CT Eijkel, and Jeffery A Wood. Enhanced ion transport using geometrically structured charge selective interfaces. *Lab Chip*, 18(11):1652–1660, 2018.

[222] Wei Guo, Liuxuan Cao, Junchao Xia, Fu-Qiang Nie, Wen Ma, Jianming Xue, Yanlin Song, Daoben Zhu, Yugang Wang, and Lei Jiang. Energy harvesting with single-ion-selective nanopores: A concentration-gradient-driven nanofluidic power source. *Adv. Funct. Mater.*, 20(8):1339–1344, 2010.

[223] Liuxuan Cao, Wei Guo, Wen Ma, Lin Wang, Fan Xia, Shutao Wang, Yugang Wang, Lei Jiang, and Daoben Zhu. Towards understanding the nanofluidic reverse electrodialysis system: well matched charge selectivity and ionic composition. *Energy Environ. Sci.*, 4:2259–2266, 2011.

[224] Wei Ouyang, Wei Wang, Haixia Zhang, Wengang Wu, and Zhihong Li. Nanofluidic crystal: a facile, high-efficiency and high-power-density scaling up scheme for energy harvesting based on nanofluidic reverse electrodialysis. *Nanotechnology*, 24(34):345401, jul 2013.

[225] Younggy Kim and Bruce E. Logan. Microbial reverse electrodialysis cells for synergistically enhanced power production. *Environmental Science & Technology*, 45(13):5834–5839, 2011.

[226] Kilsung Kwon, Byung-Ho Park, Deok Han Kim, and Daejoong Kim. Comparison of spacer-less and spacer-filled reverse electrodialysis. *J. Renew. Sustain. Energy*, 9(4):044502, 2017.

[227] Byeongdong Kang, Hyun Jung Kim, and Dong-Kwon Kim. Membrane electrode assembly for energy harvesting from salinity gradient by reverse electrodialysis. *Journal of Membrane Science*, 550:286 – 295, 2018.

[228] B. B. Sales, M. Saakes, J. W. Post, C. J. N. Buisman, P. M. Biesheuvel, and H. V. M. Hamelers. Direct power production from a water salinity difference in a membrane-modified supercapacitor flow cell. *Environ. Sci. Technol.*, 44(14):5661–5665, 2010.

[229] Javier Luque Di Salvo, Alessandro Cosenza, Alessandro Tamburini, Giorgio Micale, and Andrea Cipollina. Long-run operation of a reverse electrodialysis system fed with wastewaters. *J. Environ. Manage.*, 217:871 – 887, 2018.

[230] David A Vermaas, Joost Veerman, Michel Saakes, and Kitty Nijmeijer. Influence of multivalent ions on renewable energy generation in reverse electrodialysis. *Energy Environ. Sci.*, 7(4):1434–1445, 2014.

Appendix A

Formulation of non-dimensional number, C

Diffusioosmotic flow through a nanochannel is affected by two phenomena, namely electroosmosis and chemiosmosis. The physical interpretation of the non-dimensional number, C, is obtained through the simplified expressions of the classical chemiosmotic and electroosmotic velocities, described below.

A.1 Electro-osmotic velocity

On one hand, electro-osmotic velocity, u_{EO}, is caused by electro-migration of ions due to an external electric field or an induced one due to interaction between surface charge and bulk ions. Under a tangential electric field, E_x, without a chemiosmotic effect, it can be shown that u_{EO} for a charged nano-confinement of constant zeta potential, ζ, along its surface, can be represented as [24, 34]:

$$u_{EO} = -\frac{\epsilon \zeta E_x}{\mu}, \tag{A.1}$$

where ϵ $(= \epsilon_0 \epsilon_r)$ is the permittivity of the medium, and μ is the fluid viscosity coefficient. Electric field $(\vec{E})$ is a function of the electric potential, ϕ $(\vec{E} = -\vec{\nabla}\phi)$; $E_x = -\partial\phi/\partial x \ \hat{x}$. Due to the complex nonlinearity of the diffusioosmotic problem for our nano/micro-junction

geometry, a straight-forward analytical formulation of E_x, to the best knowledge of ours, is unavailable. From our numerical results, we observed that $|E_x| \approx |E_y|$ for the parameter ranges analyzed. We thus used this approximation to estimate $|E_x|$.

Along the charged nanochannel wall, $\vec{\nabla}\phi \cdot \vec{n} = \partial\phi/\partial y$, E_y close to the wall can be approximated from the boundary condition of constant surface charge density, σ: $\vec{\nabla}\phi \cdot \vec{n} = -\sigma/\epsilon$ [154], via

$$E_y = -\partial\phi/\partial y \approx \sigma/\epsilon. \tag{A.2}$$

Using the relation (A.2), we can estimate $E_x \approx E_y \approx \sigma/\epsilon$; hence, Eq. (A.1) can be approximated as:

$$u_{EO} \approx -\frac{\zeta\sigma}{\mu}. \tag{A.3}$$

A.2 Chemio-osmotic velocity

On the other hand, when a nanochannel is subjected to a concentration difference of electrolytes, Δc, along its length, a chemical potential difference develops and initiates fluid flow to balance the chemical potential gradient. This flow is represented by the chemio-osmotic velocity, u_{CO}, and can be expressed as [48, 49]:

$$u_{CO} = -\frac{k_B T}{\mu} \frac{\ln(1-\gamma^2)}{2\pi\lambda_B} \frac{\Delta c}{l c_0}, \tag{A.4}$$

where $\gamma = \tanh(ez\phi_s/4k_BT)$, ϕ_s is the surface potential, z is the valence of ions (while $z = 1$ in our case), e is the electronic charge, k_B is the Boltzmann constant, T is the temperature, and c_0 is the reference solution concentration. Here, λ_B is the Bjerrum length, mathematically described by $\lambda_B = z^2e^2/4\pi\epsilon k_BT$ [55], and related to the Gouy-Chapman length, λ_{GC} [55, 48]:

$$\lambda_{GC} \left(= \frac{2\epsilon RT}{\sigma F z} = \frac{2\epsilon k_B T}{\sigma e z} \right) = \frac{ez}{2\pi\sigma\lambda_B}. \tag{A.5}$$

Under the assumption that $\gamma^2 \ll 1$, we can approximate $\ln(1-\gamma^2) \approx -\gamma^2$ [47]. Further considering ϕ_s to be small such that $ez\phi_s/4k_BT \ll 1$, we get $\gamma = \tanh(ez\phi_s/4k_BT) \approx ez\phi_s/4k_BT$. Using Eq. (A.5) and the above approximations, Eq. (A.4) is simplified to:

$$u_{CO} \simeq \frac{k_B T \gamma^2}{\mu} \frac{\lambda_{GC}\sigma}{ez} \frac{\Delta c}{l c_0} \simeq \frac{ez\phi_s^2 \lambda_{GC}\sigma}{16 k_B T \mu} \frac{\Delta c}{l c_0}. \tag{A.6}$$

With the consideration of Boltzmann distribution of ions [153] and subsequent linearization of the ion distribution, the concentration of cation (c_+) and anion (c_-) can be represented as [48]:

$$c_\pm \simeq c_0 \left(1 \mp \frac{ez\phi_s}{k_B T} \exp\left(-\frac{y}{\lambda_D}\right)\right), \tag{A.7}$$

where y is the direction perpendicular to the nanochannel surface.

Using the above linearized distribution of ion concentration, we can approximate the concentration difference, Δc ($\approx c_- - c_+$), as follows:

$$\Delta c \approx 2c_0 \left(\frac{ez\phi_s}{k_B T} \exp\left(-\frac{y}{\lambda_D}\right)\right). \tag{A.8}$$

Eq. (A.6) can be simplified using the above relation:

$$u_{CO} \simeq \frac{1}{8}\left(\frac{ez\phi_s}{k_B T}\right)^2 \frac{\lambda_{GC}\sigma}{l\mu} \exp\left(-\frac{y}{\lambda_D}\right)\phi_s. \tag{A.9}$$

To gauge the dominant effect, we calculate the ratio of the typical chemio-osmotic (Eq. (A.9)) to electro-osmotic velocity (Eq. (A.3)):

$$\frac{u_{CO}}{u_{EO}} \approx \frac{1}{8}\left(\frac{ez\phi_s}{k_B T}\right)^2 \frac{\lambda_{GC}\sigma}{l\mu} \exp\left(-\frac{y}{\lambda_D}\right)\phi_s \times \left(-\frac{\mu}{\zeta\sigma}\right). \tag{A.10}$$

Here, the negative sign in the above ratio denotes that the chemiosmotic (u_{CO}) and diffusioosmotic (u_{EO}) flow are directed in opposite directions, and the final flow direction inside the nanochannel could be decided by the dominant effect.

Assuming surface potential ϕ_s to be approximately equal to the nanochannel zeta potential ζ [114], we obtain a simplified expression of Eq. (A.10):

$$\left|\frac{u_{CO}}{u_{EO}}\right| \approx \frac{1}{8}\left(\frac{ez\phi_s}{k_B T}\right)^2 \frac{\lambda_{GC}}{l} \exp\left(-\frac{y}{\lambda_D}\right). \tag{A.11}$$

Potential gradient along the charged surface can be estimated as $\vec{\nabla}\phi \cdot \vec{n} = d\phi/dy \simeq \phi_s/h$. From this relation and Eq. (A.2), surface potential can be approximated as $\phi_s \simeq -\frac{\sigma h}{\epsilon}$. We substitute this expression for ϕ_s into Eq. (A.11) and obtain:

$$\begin{aligned}\left|\frac{u_{CO}}{u_{EO}}\right| &\approx \frac{1}{2}\frac{h^2}{(2\epsilon k_B T/ez\sigma)^2}\frac{\lambda_{GC}}{l}\exp\left(-\frac{y}{\lambda_D}\right) \\ &\approx \frac{1}{2}\frac{h^2}{\lambda_{GC} l}\exp\left(-\frac{y}{\lambda_D}\right) \\ &\approx \frac{1}{2}C^2 \exp\left(-\frac{y}{\lambda_D}\right),\end{aligned} \tag{A.12}$$

where C ($= h/\sqrt{l\lambda_{GC}}$) is found to be a characteristic non-dimensional number that delineates nanofluidic DOF flow direction inside the nanochannel. For $y < \lambda_D$, $\exp(-y/\lambda_D) \approx 1-(y/\lambda_D)+ O((y/\lambda_D)^2)$. For a simplified estimation, we consider $\exp(-y/\lambda_D) \simeq 1$, ignoring the remaining terms, and consequently $u_{CO}/u_{EO} \sim C^2/2$. This allows us to express the critical C, C^* to be equal to $\sqrt{2}$ when $u_{CO} \approx u_{EO}$. In other words, the non-dimensional parameter, C, can characterize the dominance of either chemio-osmotic (when $C > C^*$) or electro-osmotic (for $C < C^*$) flow. Based on our numerical analysis and data, we found and proposed a critical C between 1.7 and 2.5, which is consistent with the analytical prediction of $C^* = \sqrt{2}$ (≈ 1.41).

Appendix B

Some properties of Nafion membrane

In total, around 35 experiments were conducted to investigate the RED electrical characteristics of an RED cell, designed using Nafion membrane. In this section, we report the procedure for obtaining current-voltage (I-V) relationship, and the observed degradation of a Nafion membrane when used for multiple experiments.

B.1 Current-voltage characteristics

In our experiment investigating RED power generation using Nafion membrane, the voltage and current outputs for different external resistance was recorded using a Keithley sourcemeter and DigiKey multimeter. At each external resistance, we obtained the time-dependent electrical response for approximately one minute at 15 Hz. The I-V characteristics of Nafion membrane was then obtained from steady-state voltage-time and current-time data for each external resistance, as illustrated by Fig. B.1. The internal resistance of the RED cell can be found from the slope of the linear I-V curve, whereas the x-intercept and y-intercept gives the magnitude of short-circuit current and open-circuit voltage, respectively.

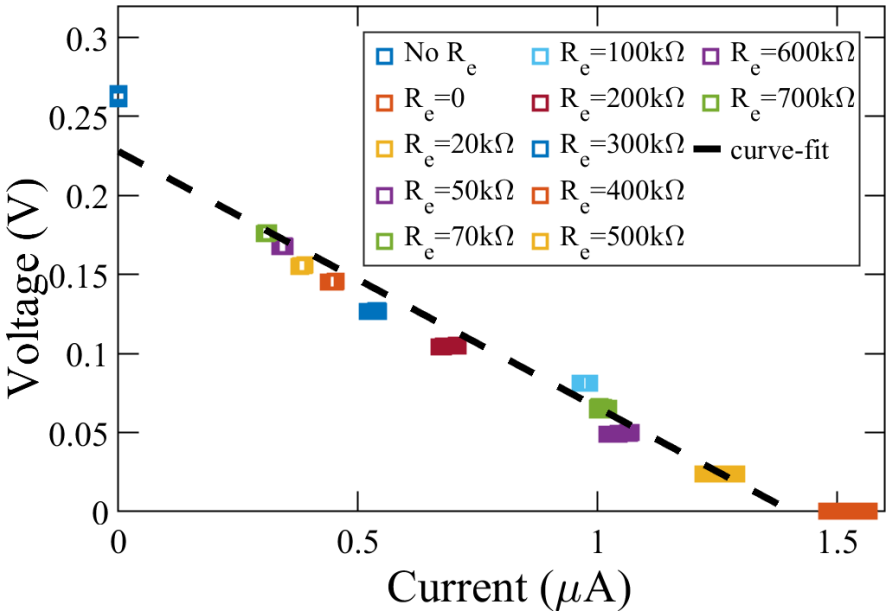

Figure B.1: Sample I-V characteristics when q_f=500 μl/min and c_H=0.86 M demonstrating the individual I-V data for various external resistance, R_e.

B.2 Membrane degradation

We observed that the effectiveness of Nafion membranes degrades throughout its usage, and seems to get degraded after a few set of experiments. The degradation results in reduced electrical response. This reduction in the performance of Nafion membrane over a short period of time raises some questions about its usability for continuous long-term usage to capture energy through reverse electrodialysis.

In Fig. B.2, we demonstrate the variability or results for 3 set of experiments performed independently. In Fig. 3.4a, we see that the the open-circuit voltage fluctuates between 0.26 – 0.32 V and short-circuit current varies between 1.5 — 2 μA. In Fig. 3.4b, we observe that the open-circuit voltage varies between 0.16 – 0.23 V, while the current between 1.2 – 1.5 μA. Inspite of these variation, the I-V curve is always linear, which represents the internal resistance always remains constant.

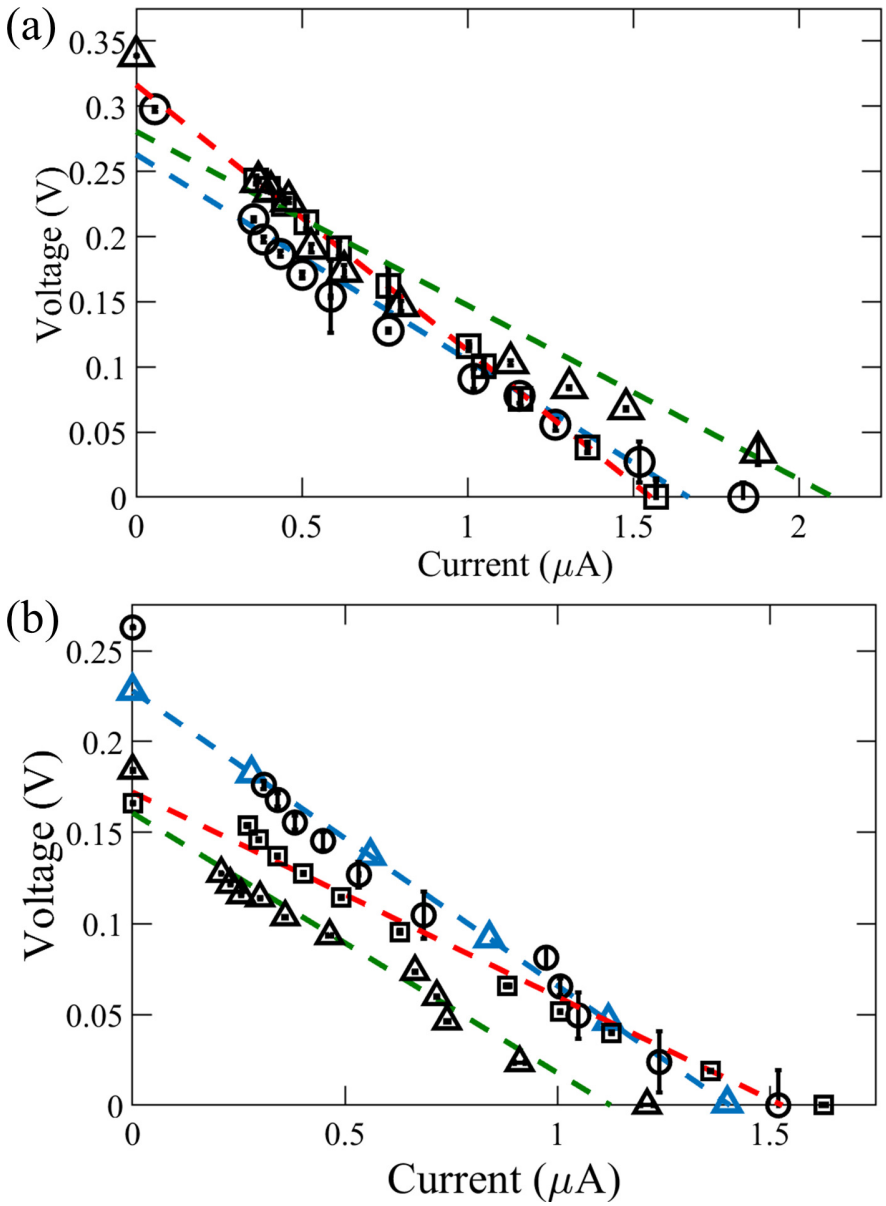

Figure B.2: Sample I-V characteristics when (a) q_f=1000 μl/min and Δc=1.37 M, and (b) q_f=500 μl/min and c_H=0.86 M for 3 independent set of experiments, demonstrating the variability of results.

Appendix C

Details of tapered nanochannel

In this supplementary section, firstly, we provide quantitative details about the possible overlap of electric double layer (EDL) near the narrower orifice. We provide a quantitative comparison of the velocity ratio from our numerical simulations with 1D analytical predictions. Lastly, we also provide an investigation of electroosmotic effect through plots of electric potential distribution and electric field in the model geometry.

C.1 Overlapping of EDL

To quantitatively explain our observations, we perform an approximate analysis based on the average anion concentration at the nanochannel orifices. For the cases shown in Fig. 5 of the main manuscript, d_t=20 nm, α=±10°, l=100 nm, d_b = 37.63 nm, c_H = 0.15 mM and c_L = 0.01 mM. Average anion concentration at the base of the nanochannel, $c_{-,b}$ ~ 1 mM and, thus, for z=1, λ_D (= $\sqrt{\epsilon_0 \epsilon_r RT/2F^2 c_0}$[153]) ≈ 9.2 nm. Given that d_b = 37.63 nm, $d_b \nsim 2\lambda_D$. Similarly, average anion concentration at the nanochannel tip, $c_{-,t}$ ~ 4/3 mM, and, thus, $\lambda_D \approx 8$ nm. For d_t = 20 nm, $d_t \sim 2\lambda_D$, and there is a much greater possibility of EDL overlap in this case.

C.2 Diffusioosmotic velocity at tip and base of the nanochannel

Due to constant surface charge density, σ, we assume the effect of electroosmotic component to be similar in both the tip and base of the nanochannel (which is quantitatively explained in the following section), and the difference in flow is due to the chemioosmotic component, u_{CO}. Thus, ignoring any contribution due to electroosmosis, we assume $u_{DO} \sim u_{CO}$, and compare our results with 1D analytical predictions of u_{DO} through scaling analysis [47]. In the two simulation cases under investigation, we vary the angle of taper, and keep all other control parameters fixed. Thus, the contribution of most variable towards diffusioosmosis can be expected to be constant, and thus, we can assume $u_{DO} \sim u_{CO} \propto \Delta c/L$. Now, since $c_{-,t}$ (or $c_{-,b}$) $\gg c_H$ (or c_L), for a simplified analysis, we assume $\Delta c \sim c_{-,t}$ for the nanochannel tip, and $\Delta c \sim c_{-,b}$ for the nanochannel base. Also the length scale, L, is assumed to be equal to d_t or d_b in the smaller and larger orifice respectively. With these assumptions, we have:

$$\frac{u_{DO,t}}{u_{DO,b}} \approx \frac{c_{-,t}/d_t}{c_{-,b}/d_b} = \frac{4d_b}{3d_t} \approx 2.5 \tag{C.1}$$

To compare the 1D analytical results with out 2D simulations, we only consider the velocity in x-direction (i.e. $u_{DO} \approx u_x$). From our simulation for α=+10°, we, thus, have $u_{DO,t} \approx 0.6$ mm/s, and $u_{DO,b} \approx 0.3$ mm/s. Thus, $u_{DO,t}/u_{DO,b} \approx 2$, which agrees with the analytical predictions with 25% deviation. This does prove that analytical 1D predictions are a great starting point for qualitative comparison. However, the large deviation points out that detailed numerical simulations is necessary for quantative accuracy.

C.3 Electric potential distribution and electric field in the nanochannel

The distribution of electric potential, ϕ and electric field, $\mathbf{E}$=(-$\vec{\nabla}\phi$) for two simulation cases of different cone angle, α = ±15° are shown in Fig. C.1 . In both the diverging and converging nanochannels, the average electric potential at the small and large orifices were similar. This would likely result in comparable electroosmotic effect near the orifices. For both diverging

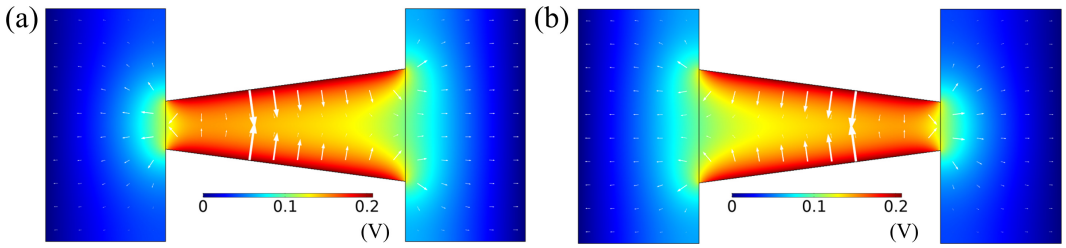

Figure C.1: Electric potential distribution (color map) and electiric field (in arrows), for a nanochannel of l=100nm, d_t=20 nm, and α=(a) 15°, and (b)-15°, with V_f=7 μm/s and Δc= 0.14 mM.

and converging nanochannels, the electric field is always directed away from the nanochannel towards the reservoirs. Interestingly, electric field was found to be maximum near the centre of the nanochannel, and not near the nanochannel tip. This observation can probably be attributed to to the overlapping of EDL near the nanochannel tip. EDL overlap combines the exponentially varying electric potential profiles from the charged nanochannel surfaces on either boundaries, which results in a higher combined electric potential. At the same time, this results in a reduction of the electric potential gradient, and hence the electric field. Smaller electric field near the orifices results in smaller electroosmosis, and hence, the diffusioosmotic flow in tapered nanochannels with fractional EDL overlap is dominated by chemioosmosis, will a smaller contribution from its electroosmotic counterpart.